NASA CR-54284

VON KARMAN CENTER

SNAP-8 DIVISION

SNAP-8 SEALS-TO-SPACE DEVELOPMENT TEST PROGRAM

VOL. I - VISCO PUMP

A REPORT TO

NATIONAL AERONAUTICS AND SPACE ADMINISTRATION

CONTRACT NO. NAS 5-417

REPORT NO. 2808 (TOPICAL) / MAY 1964 / COPY NO. 22

AEROJET GENERAL TIRE GENERAL

NASA CR-54234

SNAP-8 SEALS-TO-SPACE DEVELOPMENT TEST PROGRAM

VOLUME I - VISCO PUMP

By R. L. Lessley

Contract No. NAS 5-417

a topical report to

NASA - LEWIS RESEARCH CENTER
SNAP-8 PROJECT OFFICE
H. O. SLONE, SNAP-8 PROJECT MANAGER

Report No. 2808 (Topical) May 1964

AEROJET-GENERAL CORPORATION
A SUBSIDIARY OF THE GENERAL TIRE & RUBBER COMPANY

CONTRACT FULFILLMENT STATEMENT

This is Volume I of a four-volume topical report covering the SNAP-8 Seals-to-Space Development Test Program, and is submitted in partial fulfillment of NASA Contract No. NAS 5-417.

FOREWORD

The SNAP-8 seals-to-space concept involves the use of visco pump, molecular pump, and dynamic slinger elements. The seals-to-space program encompassed basic test work on each of these components for the purpose of demonstrating satisfactory performance for SNAP-8 operating conditions. In addition to the basic component tests, an overall integrated seal test rig was built and operated. This rig provided a nearly perfect simulation of the SNAP-8 turbine alternator assembly seal-to-space configuration and thermal environment, and demonstrated the satisfactory performance of the seal.

Volumes I through III of this report cover the work done on the visco pump, molecular pump, and dynamic slinger elements. Volume IV describes the design and operation of the integrated seal simulator.

The SNAP-8 Seals-to-Space Development Test Program was carried out under the auspices of the SNAP-8 Division, Von Karman Center, Aerojet-General Corporation, as part of the SNAP-8 Contract work.

Mr. C. G. Boone, Chief Engineer for the SNAP-8 Division, had overall responsibility for the SNAP-8 Seals-to-Space Development Test Program. Mr. R. L. Lessley, Engineering Department, SNAP-8 Division, had direct responsibility for the program. Assisting Mr. Lessley were E. A. Haglund, J. N. Hodgson, and I. L. Marburger, all of the Engineering Department, SNAP-8 Division.

ACKNOWLEDGEMENT

Thi. report covers basic visco pump tests conducted both at Aerojet's Von Karmen Center, Azusa, California, and at General Electric Advanced Technology Laboratories, Schenectady, New York. The work conducted by General Electric is reported separately in GE Report No. 63GL173, An Experimental Evaluation of Three Types of Visco Seals, by John McCrew. Most of the information contained in the GE report has been repeated herein in order to make this volume a complete report of all visco pump testing done in support of the SNAP-8 Seal-to-Space Development Program.

CONTENTS

CONTENTS (cont.)

CONTENTS (cont.)

CONTENTS (cont.)

NOMENCLATURE

A	Area of wetted seal or constant in turbulent flow equation
B	Dimensionless pressure $\frac{h^2}{\mu V}\frac{dp}{d\xi}$
C	Cavitation number or constant in turbulent flow equation
D	Shaft diameter
e	Land width along axis
E	Eccentricity correction factor
f	Friction factor
F	Force or Froude number
h	Groove depth
k'	Constant in turbulent flow equation, Equation 32
K	Function of β, $K = E\beta^3/\left[\gamma\ (1-\gamma)\right]$
K'_1	Constant in turbulent pressure coefficient equation, Equation 33
K'_2	Constant in turbulent pressure coefficient equation, Equation 33
K_1	Sealing coefficient constant
K_2	Sealing coefficient constant
ℓ	Leakage path length or mixing length
L	Length of wetted portion of seal
n	Number of threads or power of Reynolds number
N	Shaft angular velocity, revolutions/unit time
p	Pressure
p_v	Vapor pressure
Δp	Pressure drop across seal
P	Power

NOMENCLATURE (cont.)

Q	Volume flow
r	Radius
Re_h	Reynolds number ($Re_h = \frac{Uh}{\nu}$)
Re_δ	Reynolds number ($Re_\delta = \frac{U\delta}{\nu}$)
t	Thread pitch, $t = \pi D \tan \phi$
T	Measured torque and transverse component of flow velocity
t^*	t/n
u	Velocity along groove axis
U	Shaft surface velocity
V	Component of shaft surface velocity along groove
w	Width of channel
w'	Width of land
x	Coordinate along shaft axis
y	Coordinate in radial direction
β	Ratio of clearance to groove depth, $\beta = \delta/h$
γ	$w/(w + w')$
δ	Radial clearance
μ	Absolute viscosity
ρ	Fluid density
σ	Fluid surface tension
ϕ	Helix angle
ω	Angular velocity
ξ	Coordinate along groove axis

NOMENCLATURE (cont.)

η	Coordinate along perpendicular to groove axis
λ	Moment coefficient
ψ	Sealing coefficient, $\frac{\Delta p \delta^2}{\mu U L}$

Subscripts

c	couette flow value
g	groove
ℓ	lands or laminar
m	mean value
o	optimum
p	pressure
t	turbulent

SUMMARY

In order to permit use of oil-lubricated anti-friction bearings in the SNAP-8 power conversion system rotating assemblies, a seal is required to prevent mixing of mercury and oil. A seal concept was evolved in which mixing of mercury and oil is prevented by venting a section of the shaft to space and permitting a small controlled leakage of each liquid to the space vent cavity. The particular seal-to-space concept advocated for use in SNAP-8 involves use of the visco pump (a device consisting of a shaft with helical grooves rotating within a close-fitting housing). This seal element, when functioning properly, prevents passage of raw liquid through the seal. It establishes a liquid-vapor interface past which only vapors can leak. Visco pumps function improperly under certain conditions. A condition known as "breakdown" can prevail, in which case liquid droplets can be lost from the interface and the effectiveness of the seal as a barrier to liquid leakage is destroyed. Since the visco pump technology is not sufficiently advanced to permit prediction of conditions under which breakdown will occur, a test program was required to demonstrate the adequacy of the visco pump operating with SNAP-8 fluids (mercury and ET-378 oil) and operating conditions. Tests were conducted with quartz visco pump test sections which permitted viewing and photographing of the liquid-vapor interface during operation of the test rig. Results showed the visco pump interface to be stable for SNAP-8 operating conditions. There were no signs whatsoever of "breakdown." In addition, measurements of drag and pumping coefficients were made for a variety of pump configurations. The visco pump has been shown to be very well suited for use in the SNAP-8 seals-to-space.

A few subsidiary tests, which were run with configurations and operating conditions not representative of the SNAP-8 seal, revealed incipient and advanced stages of visco pump "breakdown." Photographs and observations made during these tests have done much to clarify the nature of the "breakdown" phenomenon.

I. INTRODUCTION

The visco pump, sometimes called a screw pump or helical groove pump, consists of a threaded shaft placed within a close-fitting housing. The clearance between the threaded shaft and the housing is very small (similar in magnitude to the thickness of a liquid boundary layer). When the shaft rotates, the interaction between the shaft thread and any liquid present tends to create a pressure gradient along the shaft. The pressure gradient is essentially the same if a smooth shaft is rotated within a helically grooved housing. Tests reported herein reveal that an even greater pressure gradient is obtained by placing helical grooves in both the shaft and the housing.

The basic equations governing visco pump performance for laminar flow were derived by Rowell and Finlayson (Referencer 1, 2, and 3) in 1922. In 1932 Lawaczeck (Reference 4) suggested the use of a herringbone helical groove configuration as a shaft seal. Boon and Tal (Reference 5) and Zotov (Reference 6), among others, attempted to determine optimum channel configurations for effective pumping and low power consumption. Meanwhile investigators such as Piggot (Reference 7) and Carley and Strub (Reference 8) were applying the visco pump to the extrusion processes. All of the work mentioned above applied to laminar flow operation. A good survey of progress prior to 1962 is provided by Stair (Reference 9). More recently, McGrew and McHugh (Reference 10) have defined visco pump performance well into the turbulent flow regime.

Two visco pumps placed in opposition to each other form a herringbone pattern. Such a configuration, when not completely full of liquid, will operate with a high pressure at the center and with liquid-gas interfaces at the two edges of the herringbone. The fluid thus contained can often serve as an excellent buffer seal. This type of seal is called a visco-seal. The possible use of such a seal in the SNAP-8 seal-to-space concept prompted the investigation reported herein.

The role of a visco-seal in the SNAP-8 turbine seal-to-space is illustrated in Figure 1. There it is shown that the visco seal serves as a barrier to prevent loss of raw liquid. It establishes liquid-vapor interfaces in the turbine cavity and seal-to-space. The pressure at the turbine cavity interface is 20 psia. The pressure at the seal-to-space interface is the vapor pressure of the liquid at the interface. The difference between these pressures, which would ordinarily cause leakage along the shaft, only causes a greater liquid engagement with the low-pressure side of the visco seal herringbone pattern. This additional engagement on the low-pressure side of the visco seal exactly balances the turbine cavity pressure

and thus prevents loss of raw liquid. The purpose of the visco seal heat exchanger is to cool the seal-to-space liquid vapor interface and thereby reduce the density of the vapors generated at that interface.

Although this seal arrangement appears to be a plausible one, existing visco pump literature did not provide sufficient evidence to show it would work. Little was known regarding the nature of the visco seal liquid-vapor interface other than the fact that McGrew and McHugh (Reference 10), in investigating visco pump performance in the turbulent regime, had observed a "breakdown phenomenon" which is not yet fully understood. They reported that at large shaft speeds, loss of fluid from the liquid interface sometimes occurs. This indicates a breakdown of effective sealing action. The speed at which breakdown occurs depends on thread configuration, radial clearance between the helical land and the housing, and properties of the pumping fluid. Surface tension of the liquid is believed to play an important role.

Also it was not known whether the performance of the very short pumping sections required in a turbine seal is proportionately as great as that reported in the literature for comparatively long pumping sections.

In order to justify use of the Figure 1 visco seal configuration in the SNAP-8 seal-to-space, it was necessary to obtain performance data for short pumping sections and to demonstrate that interface breakdown conditions do not occur at SNAP-8 operating conditions. SNAP-8 has two seals-to-space: one in the turbine assembly and one in the mercury motor pump assembly. The respective operating conditions are as follows:

	Shaft Speed rpm	Shaft Diameter in.	Peripheral Velocity in./sec
Turbine Assembly	12,000	2.00	1256
Mercury Motor Pump Assembly	7,800	1.25	510

The SNAP-8 Visco Pump Test Program was initiated to answer these questions by running visco pump configurations at and near the above conditions.

Meanwhile a somewhat different seal configuration (Figure 2) was adopted for the initial turbine assembly. In this configuration the seal-to-space interface is created by the action of a liquid slinger, and possible visco seal problems are, for the time being, circumvented. This configuration does require a stepped shaft, however, thus introducing complication to the mechanical design. It also reduces the effectiveness of the seal heat exchanger causing increased liquid-vapor interface temperature and thereby increasing seal-to-space leakage.

II. PROGRAM OBJECTIVES

The SNAP-8 Seal-to-Space Test Program encompassed two series of tests - one conducted at the Aerojet Von Karman Center and the other conducted at the General Electric Advanced Technology Laboratories.

The Aerojet test rig was designed with a transparent quartz housing to permit viewing of the mercury liquid-vapor interface during operation. The interface cavity was equipped with a vacuum connection in order to create a liquid-vapor interface instead of a liquid-air interface. The specific test objectives for the test series were as follows:

A. Obtain pumping coefficients for several visco pump configurations running at SNAP-8 conditions.

B. Obtain drag coefficients for several visco pump configurations running at SNAP-8 conditions.

C. Take microflash photographs and high-speed movies of the mercury liquid-vapor interfaces to determine if they are sufficiently stable for use in a seal-to-space.

D. Observe the effect of radial clearance on interface stability.

E. Observe whether incipient breakdown conditions exist at or near the SNAP-8 operating conditions.

F. Observe whether short visco pump sections are proportionately as effective as long sections.

The decision to build a visco pump test rig with a transparent quartz housing was an ambitious one. Fabrication of a quartz housing was attempted only because of the formidable capabilities of the Von Karman Center Astrionics Division Optics Shop and because there was a definite need to observe the visco seal liquid-vapor interface during actual operation. At the same time the dependence on the successful fabrication of a quartz test section with helical grooves was a calculated risk. There remained the possibility that the quartz test section, once fabricated, would prove to be fragile and easily broken.

For these reasons, the General Electric Advanced Technology Laboratories in Schenectady, New York was authorized to conduct additional tests of visco pump configurations using a modified version of an existing test rig. The objectives of these tests were as follows: (a) to obtain pumping coefficients for several visco pump configurations running at SNAP-8 conditions, (b) to obtain drag coefficients for several visco pump configurations running at SNAP-8 conditions, and (c) to observe whether any loss of liquid from the seal liquid-air interface occurs at SNAP-8 operating conditions.

As it turned out both efforts were very successful and the work done at GE (ATL) did much to complement the work done at Von Karman Center.

III. TEST METHODS AND APPARATUS

A. AEROJET VISCO PUMP TEST RIG

The Aerojet visco pump test console and test rig are shown in Figures 3 and 4. Figure 5 is a close-up view of the visco pump test section showing the quartz test housing with its helical groove pattern. Figures 6 and 7 show the quartz test section during and after fabrication. Figure 8 is a drawing of the test rig which identifies the major functions. The bearing spindle is turned at 6000 to 12,000 rpm. A pressurized mercury cavity at one end of the test section is used to control axial engagement between the fluid and pumping section. A vacuum is applied to the other end of the pumping section to assure that interface stability is not influenced by the presence of a gas. The heat generated within the visco pump is carried away by water which flows through passages in the rotating pump shaft. The water is introduced at the shaft end, as illustrated in Figure 8. It passes through the pumping section cooling passages and then flows between two shaft seals into a housing exit port. Figure 9 is a diagram of the test arrangement.

The evaluation of each visco pump configuration involved running at a constant speed setting, applying successively greater mercury pressures to the test section, and recording the resulting series of axial engagement values. Shaft speed, coolant water flow, and pressures and temperatures at each end of the test section were recorded for each pressure setting. This was repeated at several different shaft speeds - usually 6000, 9000, and 12,000 rpm. Thus a series of pressure vs engagement curves were obtained. Deceleration transients were measured with the pumping section partially full and with the pumping section empty in order to obtain a measurement of visco pump power consumption. This method of power measurement requires an accurate measurement of the polar moment of inertia of the rotating parts of the test rig. Microflash photographs (7×10^{-6} sec exposure) and high-speed movies (8000 frames per sec) were taken of many of the liquid-vapor interface conditions.

Visco pump pressures were measured with Ashcroft bourdon tube gages (0.25% accuracy). The temperatures were measured with Weston Symplytrol pyrometers with IC thermocouples (2% accuracy). Shaft speed was measured with a magnetic pickup mounted on the shaft housing and coupled with a Hewlett Packard electronic counter (0.5% accuracy).

The major test fluid was mercury. One configuration, however, was also evaluated with ET-378 oil. The absolute and kinematic viscosity values of these two fluids are presented in Figures 10 and 11.

B. GENERAL ELECTRIC (ATL) VISCO PUMP TEST RIG

The test device used in Reference 10 was modified to accept a 2-in. shaft in order to meet the geometry requirements for this study. A schematic of the test apparatus is shown in Figure 12. Essentially, this device consists of a variable-speed spindle equipped with an internal taper at one end. Special tapered

quills, on which the test screw threads are cut, fit into the internal taper of the high-speed spindle. This arrangement permits interchange of quills with different screw thread geometry.

The test quills project into a close clearance sleeve. The fluid to be sealed is introduced under pressure into the upper end of the sleeve. To carry away the heat generated by viscous shear, the sleeve is water cooled. A helical groove was cut in the sleeve surface and copper tubing inserted and soldered to it.

The sleeve is attached to a stub shaft mounted in ball bearings. The outer races of the ball bearings were held in a bracket which could be adjusted to align the screw seal shaft and the sleeve surrounding it.

Figure 13 is a schematic diagram of the test loop. The pressurized fluid is introduced at the top of the sleeve. The fluid is pressurized by imposing pressurized nitrogen over the surface of the fluid in a pressure accumulator. The nitrogen pressure is controlled by a standard gas regulator. As a measure of sealing effectiveness, the reservoir can be isolated by a valve from the fluid in the sleeve; for the incompressible fluid used in the tests, any leakage is reflected in a decay in the upstream pressure. Leakage past the screw flights could also be collected in a shield at the lower end of the sleeve.

Inlet and exit cooling-water temperatures were recorded from the emf of copper constantan thermocouples. A rotameter provided for the flow measurement. Thermocouples were also used to measure sealing fluid inlet temperature and the axial temperature distribution in the sleeve. For the latter, the thermocouples were embedded at 0.5-in. intervals along the sleeve and 0.030 in. from the inner wall.

Bourdon tube gages were used for pressure measurements. Since the pressure gages were mounted above the test quill, the pressure due to the height of the column of fluid in the pressure lines was also measured and added to the recorded pressure. The axial pressure distribution was also used to determine the axial location of the fluid-air interface within the seal. At the limiting sealing pressure, the sealed fluid fills the entire seal length. At lower pressures, the fluid-air interface moves further within the seal. Part of the seal length is filled with ambient air and part with fluid. The wetted length of seal, L, was found by fitting a straight line to the pressure distribution by the method of least squares and extrapolating the fitted line to ambient pressure.

Torque transmitted to the sleeve was measured by strain-gage beams supplying restraint to rotation. Some resistance to rotation is supplied by the ball bearings and pressure lines. Torque reading calibrations as low as 10 in.-g could be duplicated to within 5%. Since actual test readings varied from 200 to 2500 in.-g, this effect constituted a relatively small error. To minimize this restraint, flexible lines were used for pressure lines, flow, and thermocouples.

Speed was measured using a magnetic pickup on the high-speed spindle and electronic counter.

Each test geometry was tested on several test fluids in an effort to demonstrate the universality of the correlations developed in Reference 10. The fluids were chosen to give the operating characteristics of each seal geometry from the laminar, through the transition and into turbulent regimes of operations. The fluids used were silicone fluids, water, and mercury. The silicone fluids are desirable since they have a relatively flat viscosity-temperature curve and can be blended to produce intermediate viscosities. Water is readily available and happens to have a viscosity intermediate between SF96-2 and mercury.

Viscosity-temperature curves of silicone oils, water, and mercury are shown in Figure 14. Comparative values of surface tension are given in Figure 15.

IV. VISCO PUMP CONFIGURATIONS EVALUATED

The attempts of various investigators to determine optimum thread configurations for laminar operation of visco pumps is summarized in Table 1. There the work of Zotov (Reference 6), Asanuma (Reference 11), Boon and Tal (Reference 5), Whipple (References 12 and 13), Hughes (Reference 14), and McGrew and McHugh (Reference 10) are presented. Both test results and completeness of theoretical derivation indicate that the optimum configuration of Zotov represents the best insight presently available. According to his findings, channel groove depth should be approximately three times the radial clearance between the lands and the housing. Sixty-three percent of the pitch should be groove and 37% should be land. Groove width should be 12-1/2 times the groove depth; the optimum helix angle is 14-1/2°. These proportions give near-optimum pumping in the laminar flow regime.

A. AEROJET VISCO PUMP CONFIGURATIONS

The Aerojet visco pump tests involved 12 different configurations. These configurations are defined by Table 2. None of these configurations duplicate the optimum channel configuration of Zotov. The channel pitch was restricted to essentially 0.1 in. in hope of maintaining good pumping coefficients for short pumping sections. Configurations with 1, 4, and 12° helix angles were tested. Configurations with groove channels in the housing, on the shaft, and in the housing and shaft were evaluated.

B. GENERAL ELECTRIC (ATL) VISCO PUMP CONFIGURATIONS

The configurations tested by General Electric (ATL) are listed in Table 3. The three configurations follow the proportions cited by Zotov quite closely with the exception of Configuration C which was assigned the non-optimum helix angle of 4°. Configurations A and B are identical with the exception that A has shaft grooves while B uses housing grooves.

V. TEST RESULTS

A. GENERAL ELECTRIC (ATL) TESTS

1. Test Conditions

All three configurations of Table 3 were tested over a speed range extending from 13,200 rpm to the minimum speed (at which the fluid completely filled the seal). In each case a fixed pressure was applied to the seal and readings of pressures and temperatures were taken for various shaft speeds. Series of readings were taken for applied pressure differentials of 15 and 30 psi for water and the silicon fluids. The mercury tests were run with applied pressure differentials of 15, 30, 45, and (where possible) 60 psi.

2. Pumping Coefficients

a. Configuration A (Zotov Configuration - Grooves on Shaft)

This thread geometry is the same as that tested in Reference 10 on a 1-in. shaft. The configuration is tested here on a 2-in. shaft mainly to investigate stability of the seal interface with mercury - a fluid not used in the Reference 10 test. The pumping coefficients obtained are plotted vs Reynolds Number in Figure 16. The solid curve in Figure 16 represents the data obtained for the same thread geometry on the 1-in. shaft of Reference 10.

At very low Reynolds numbers, the sealing coefficient is a constant as predicted by laminar theory. Operation in this range was very steady as evidenced by the small scatter in the data. The measured laminar sealing coefficient was 0.49 which is the same range as the other measured values of Table 1.

At a Reynolds number of about 100 the sealing coefficient drops off slightly and then rises again. At a Reynolds number of 1000, the flow becomes fully turbulent, and the sealing coefficient rises with almost constant slope. A majority of the data lie within a band of $\pm 15\%$ of the mean. At high Reynolds numbers, the data run above the curve given by Reference 10. Since eccentricity effects alone can cause a 50% variation in sealing coefficient, the agreement between the data of Configuration A and the solid curve based on the data for the 1-in. shaft of Reference 10 is acceptable. Thus, at least for shaft diameters larger than 1 in., curvature effects appear to be small or negligible.

At Reynolds numbers above 10,000, the wetted length of the seal for this geometry becomes so short (i.e., less than 0.2 in.) that accurate measurement of the wetted length of seal becomes impossible with the instrumentation used. At a Reynolds number of 9460, and a Δp of 30 psi, the wetted length L was 0.36 in. With further increase in speed there was not a proportionate decrease in pressure along the seal - and consequently in wetted length - and the sealing coefficient dropped off. Data from the Aerojet tests, discussed in the next section, provides a more complete explanation of this apparent drop-off in pumping coefficients.

b. Configuration B (Zotov Configuration - Grooves in Housing)

The geometry of Configuration B was the same as Configuration A except that the grooves were placed in the sleeve rather than on the shaft. The sealing coefficient results are shown in Figure 17. The sealing coefficient did not appear to be affected. The data for this configuration showed considerably more scatter than Configuration A. This was probably a result of the grooving on the sleeve affecting the pressure measurements more than the smooth sleeve of Configuration A. Above a Reynolds number of 12,000, the interface had passed the last pressure tap at x = 0.156 in.; above this value it was no longer possible to determine the wetted length L. This is in contrast to Configuration A, where a pressure was measured at the first pressure tap (x = 0.156 in.) to a maximum speed of 13,200 rpm.

The laminar coefficient for this configuration was 0.45 - a value slightly lower than the 0.49 measured with Configuration A. In the turbulent regime, the data also ran lower. Eccentricity at assembly for both configurations was essentially the same so the difference cannot be attributed to this cause. However, the difference in sealing coefficient between Configurations A and B is no larger than the scatter in each set of data. Therefore it was concluded that the location of the threads (shaft vs sleeve) had no appreciable effect on the sealing.

c. Configuration C (4° Helix Angle - Grooves in Housing)

The laminar flow analysis of the Appendix predicts a decrease in sealing coefficient with helix angle. This variation in sealing coefficient with helix angle is shown in Figure A-3. A reduction in helix angle from 14.5 to 4° should decrease the theoretical sealing coefficient from 0.59 to 0.23. Reference to Figure 18 shows that the measured laminar coefficient for the 4° configuration was about 0.24 which is very close to the theoretical value. Thus, agreement with the theoretical laminar sealing coefficient was much better with the 4° helix geometry than with the 14.5° geometry. The average ratio of the measured laminar sealing coefficient of Configuration C to that for Configurations A and B was 0.51 in contrast to the 0.4 ratio predicted by theory. Thus the data show that the penalty in sealing effectiveness to be paid for reducing the helix angle is not as severe as the theory would predict in laminar flow.

3. Power Loss Measurements

In the Appendix it is pointed out that the laminar flow power loss in the screw seal arises from both viscous effects and pressure effects, but that the losses arising from the pressure effects contribute only a small percentage of the total. Since the groove depth and clearance were the same for all configurations tested, the viscous loss should be the same. Inasmuch as this loss forms the largest proportion of the total loss, there should be little difference between the moment coefficients for the three geometries. Reference to Figures 19, 20, and 21 shows that within the accuracy of the measurements, the above conclusion is correct. The lower dotted curve is the loss curve for a rotating shaft in a cylinder of clearance, h, over part of its area and of clearance, δ, over the

remaining area. The upper dotted curve is the loss curve for a rotating cylinder of clearance, δ, over its entire area. It is apparent that the seal loss is better approximated by the upper dotted curve, with the grooves neglected.

It should be noted that the contribution to the seal loss caused by the quill end was calculated and subtracted from the measured loss value. Even with this correction, at values of $L/D < 1.0$, the moment coefficient curves deviated from the moment coefficient curves of Figures 19, 20, and 21. This effect is demonstrated in Figure 22. The ratio of the actual moment coefficient to the moment coefficient predicted by the solid curve in moment coefficient plots, is shown. This increase in loss may result from not being able to accurately calculate the losses at the end test quill. At low L/D ratios these losses form a large part of the total loss; if the estimates of their value were low, such an effect as shown in Figure 22 would be observed. On the other hand, the increase in moment coefficient at low L/D ratios could result from end effects within the seal length itself. It was not possible to determine the exact cause of this phenomenon.

It can be concluded, however, that for $L/D > 1.0$, screw seal loss can be conservatively predicted by treating the seal as a cylinder rotating in a sleeve of clearance, δ, and neglecting the grooves.

4. Seal Breakdown

One of the most important test objectives was the determination of the speed at which loss of liquid from the interface was detected. With mercury, loss of liquid was not detected through speeds of 13,200 rpm for all three geometries. This was checked in two ways. Visual observation for fluid in the shield at the lower end of the sleeve provided one check. The other method was to close the valve between the seal and pressure accumulator and monitor the inlet pressure. Once seal breakdown occurred with the water or silicone oils, the seal pressure dropped off at a rate of about 1 psi every 5 min. This drop-off in pressure was not observed with mercury at any speed.

This result could indicate two different phenomena: (a) the interface between the mercury and air could have been stable and there was no leakage, or (b) drops could be breaking away from the interface but the unwetted portion of the seal scavenges these drops and pumps them back up to the interface.

Pictures from the Aerojet tests, discussed below, revealed that no breakdown conditions exist for mercury at the 12,000-rpm SNAP-8 operating conditions.

It is interesting to compare the lowest shaft speeds at which breakdown, as evidenced by loss of liquid, has been observed in tests with various fluids. This can be done with reference to Table 5.

The silicone fluids leaked at all speeds for all three geometries. The entries in the table are the lowest surface velocities run; thus breakdown must have occurred at some velocity below these values. Data from Reference 10 are given

for comparison. Water broke down at about 1100 in./sec for all three geometries. No loss of liquid was observed for mercury tests at any speed.

A dimensional analysis of the screw seal is presented in the Appendix. The analysis suggests that surface tension forces may play an important part in the stability of the interface. It is noted from Table 5 and Figure 15 that the speed at which breakdown occurs increases with increasing surface tension. As pointed out in the Appendix the surface tension of a fluid in contact with some gas is a function of the fluid and the gas. The materials of the seal and the wetting characteristics of the fluid on these materials will also probably influence seal breakdown.

B. AEROJET (VON KARMAN CENTER) TESTS

1. Summary

Twelve different visco pump configurations were evaluated in the tests conducted at Aerojet's Von Karman Center. These configurations are identified in Table 2. The configurations with the 12° helix angle yielded the most significant results. They revealed that stable liquid-vapor interfaces are obtained with mercury at radial clearances of 0.003, 0.005, and 0.007 in. No signs of seal breakdown were seen for operation at 12,000 rpm in this range of radial clearance values. Interface stability was satisfactory regardless of whether the visco pump helical channel was located on the shaft, in the housing, or on both the shaft and housing. Some of the configurations generated a small number of droplets at the interface. The scavenging action of the visco pump is so excellent, however, that these droplets seldom wander more than one pitch away before being forced back to the interface. The pumping coefficients for configurations with housing grooves are essentially the same as for configurations with shaft grooves. The pumping coefficient is more than doubled, however, when grooves are placed on both the housing and shaft.

A definite edge effect was observed for all configurations tested. At high speeds, very little pumping is obtained at small axial engagement. Further increase in axial engagement gives a greater than proportionate increase in pumping head. This edge effect was found to be most pronounced for configurations with shaft grooves, to the extent that the other configurations should be preferred in applications where the visco seal must be very short.

2. Pumping Coefficients

The pumping coefficient is defined in the Appendix as

$$\Psi = \frac{\Delta p \, \delta^2}{L \, \mu \, V}$$

It is constant for laminar Reynolds numbers $\left(\frac{r\,\omega\,\delta}{\nu}\right)$ less than 200 and increases almost linearly with Reynolds number for turbulent regime values in excess of 1000.

The tests conducted at the Von Karman Center revealed that a slightly more subtle definition of the pumping coefficient is necessary if the data involve short pumping sections. Curves of pumping vs axial engagement of the liquid followed the pattern illustrated in Figure 23. There it is seen that the pumping vs engagement curves, though linear in nature, do not pass through the origin. At low speeds a considerable positive pressure must be applied to create any axial engagement at all. At high speeds, the liquid appears to enter the pump easily and a definite engagement is necessary before any signs of pressure generation can be observed. This edge effect is indeed interesting and is controlled by factors that may not be understood for a long time. For the moment, however, attention will center on the edge effect as it is related to the obtaining of accurate pumping coefficients. Note from Figure 23 that the pumping coefficient defined above is equal to the quotient obtained by dividing the ordinate by the abscissa. Thus the pumping coefficient value of any data point is equal to the slope of the line joining that point to the origin. Herein the weakness of this definition of pumping coefficient becomes evident. It is quite clear that the total characteristic of a visco pump configuration consists of an edge effect and a pumping coefficient. The edge effect may not be a function of Reynolds number at all; indeed the evidence available indicates it is not such a function. And the pumping coefficient is clearly the slope of the line connecting the data points corresponding to a given speed. In this case the true pumping coefficient is obtained by changing the definition of the pump coefficient to

$$\psi = \frac{\Delta p\ \delta^2}{\Delta L\ \mu V}$$

Replacing $\frac{\Delta p}{L}$ by $\frac{\Delta p}{\Delta L}$ gives the actual slope of pumping curve instead of the slope of a line passing through the origin which has been made meaningless by the edge effect. Notice that for very large axial engagement, these two slopes tend to converge on the same value. So the revised definition of pumping coefficient might be considered that for a very long pump, where edge effects are negligible.

The pumping coefficients obtained from the visco pump tests are presented in Figure 24. These coefficients are based on the actual slope of the pumping curves. Had the original definition of pumping coefficient been used, curves like those of Figures 25 and 26 would have been obtained. These curves show a tendency for the coefficient to drop-off at larger Reynolds numbers. The same behavior is seen in tests reported by General Electric in Figure 16. The explanation for this behavior is obtained from Figure 23 where it is seen that the slope of the dotted lines between the origin and successively lower points on a high-speed curve must assume successively lower values, thus creating an apparent drop-off in sealing coefficient. From Figure 23 it is clear that this is due entirely to the edge effect.

Returning to Figure 24 it can be seen that the pumping coefficients obtained with housing grooves and shaft grooves are essentially the same. Compare these pumping coefficients with those obtained in the General Electric tests of the optimum Zotov configuration (solid curve in Figure 24). The pumping coefficients obtained for the Zotov configuration are approximately 50% greater than those obtained for the configurations tested at Aerojet. It would appear that even though the Zotov channel proportions are derived on the basis of laminar flow, they are superior proportions for turbulent flow as well.

The data points for the configuration with both housing and shaft grooves show the pumping coefficient to be nearly triple that obtained for housing or shaft grooves alone. This is very significant in seal applications where close radial clearances are difficult to maintain. If necessary, the radial clearance can be doubled with a net improvement in pumping if both housing and shaft grooves are employed.

3. Edge Effect

Figures 27 through 35 show pumping curves for configurations with shaft grooves, housing grooves, and both shaft and housing grooves. Each of these curves shows the same edge effect illustrated in Figure 23 and discussed above. The edge effect for the shaft groove configuration is considerably greater than that shown for the other configurations. It is not known why this should be the case.

It is worthwhile to consider what parameters influence edge effect. Are correlations possible with available data? Although the curves are labeled according to Reynolds number they actually correspond to three discrete speed values: 12,000 rpm (triangle points up), 9000 rpm (circles), and 6000 rpm (triangle points down). The initial impression of a correlation between edge effect and Reynolds number is a false impression. Examination of all curves except that of Figure 30 leads to the impression that lower Reynolds numbers reduce pumping loss due to edge effect. Figure 30 alone among the set of curves represents test of a viscous fluid (i.e., ET-378 oil). If Reynolds number were the controlling parameter, the curve in Figure 30 should intercept the abscissa axis far to the left of the origin. Instead it shows an edge effect almost identical to that shown in Figure 31 for the same speed. The two 12,000-rpm curves (triangle points up) of Figures 30 and 31 have nearly identical edge effects although their Reynolds numbers are greatly different. It appears that the edge effect correlates better with shaft speed than with Reynolds number. Possibly the edge effect, like the breakdown phenomenon, is influenced by the surface tension or Weber's number effect. The data of the current test series are not adequate to test this supposition. The present data indicate only that an edge effect does exist, and that it is more pronounced in the shaft groove configuration than in the housing groove or shaft and housing groove configurations.

4. Power Loss Measurements

It was originally intended that power loss measurements would be taken for all configurations tested. The measurements were taken by means of an

inertia method wherein measurement of the deceleration speed transient and of the inertia of the rotating mass permit calculation of the power consumption. One measurement was made with the pumping section containing liquid and another with the pumping section empty, the difference between the two power consumptions being attributed to the visco pump.

The tests were run and the deceleration transients were measured on an oscillograph. Unfortunately a faulty oscillograph was used. Since almost all of the testing was conducted during an accelerated 2-week period, the inadequacy of the deceleration measurements was not discovered until it was too late. As a result no power measurements were obtained from the tests conducted at Aerojet.

It is fortunate that good power measurements were obtained from the tests conducted at General Electric (see Figures 19, 20, and 21). It is regrettable, however, that no comparison of power consumption was obtained for the configuration with both housing and shaft grooves. Since performance for such a configuration has never been reported before, and since its pumping characteristics are quite impressive, it would have been very interesting to compare its power consumption to that measured for housing or shaft groove configurations. As it is, little is known about the relative power consumption of these configurations.

The heat generated by the visco pump drag was transferred to water flowing in cooling passages within the shaft. The inlet temperature and flow rate of the water were held essentially constant for all tests of the series. With identical cooling, radial clearance, and axial engagement, the mercury temperature ran hotter in the housing and shaft groove configurations than in the other configurations; this in itself is evidence that the increased power consumption must be associated with the large pumping coefficient previously discussed. But it is not yet known just how large a power consumption must be attributed to the housing and shaft groove visco pump configuration.

5. Interface Stability

The major reason for conducting the visco pump tests was to discover whether seal breakdown occurs with mercury at the SNAP-8 operating speed of 12,000 rpm. The interface for each configuration was observed visually during the test with ordinary light and with strobescope light. Microflash pictures were taken of these interfaces, and high-speed movies were taken during testing of five of the twelve configurations (see Table 2). The microflash pictures for configurations considered for application to the turbine-alternator assembly seal-to-space are shown in Figures 36 through 43. These pictures were taken at 12,000-rpm shaft speed for the three basic configurations and for radial clearances of 0.003, 0.005, and 0.007 in.

Figure 36 shows the housing groove configuration at 0.003 in. radial clearance. The axial engagement for an applied pressure of 100 psi is only 1/4 in., a more than adequate pressure gradient for most seal applications. Traces of cavitation were observed across the lands. This is due partly to the fact that a vacuum exists at the liquid-vapor interface. In general, the tendency toward cavitation is more pronounced at low land clearances while seal breakdown is to be

expected at large clearances. The present test series extended from 0.003 to 0.007 in. radial clearance with no evidence of seal breakdown. The net effect of increased clearance, therefore, was an improvement of the interface due to a diminishing tendency to cavitate in the vicinity of the interface.

Figure 37 is the same configuration shown in Figure 36, but the test fluid is ET-378 oil and the applied pressure is only 61.5 psi. The liquid-vapor interface is difficult to see in this photograph. It assumed the appearance of a viscous lip located immediately below a cavitation zone. Cavitation in the remainder of the pumping section is suppressed by higher pressures. Since the pumping section was run at larger engagements prior to the taking of this picture, it is obvious that an oil film must have existed below the liquid-vapor interface. Nothing of a mobile nature was observed, however. To all appearances the liquid-vapor interface was stable and an effective barrier to loss of liquid. The nature of the interface, however, is quite different than that observed for mercury. Our observations lead us to believe that had the interface been a generator of liquid droplets, the pump would not have performed the scavenging action nearly as well as it does with a non-wetting fluid such as mercury. The visco pump is an excellent scavenger with mercury. Presumably the visco pump would be a good scavenger of oil also if the boundaries were coated with a nonwettable material such as Teflon.

Figure 38 shows a configuration with shaft grooves and a 0.003 in. radial clearance. The liquid-vapor interface is observed to be generating liquid droplets. These droplets are immediately scavenged back to the interface. The clear region below the interface is a scavenging zone. All scavenging is accomplished in a region within one pitch of the interface. In the few tests where droplets were generated, they seldom migrated more than one pitch away from the interface before being scavenged. The mist in the low part of the test section consists of particles on the smooth outer wall which are too small to be scavenged. It is a completely immobile film which was created on start-up of the test.

The formation of droplets at the interface should not be confused with the breakdown phenomena which will be discussed later. Breakdown is accentuated by increasing speed and radial clearance. The tendency of this interface to generate droplets was observed to diminish with increased speed (see Figure 44) and to disappear entirely at larger radial clearances (see Figure 39).

Figure 39 shows a very crisp interface generating almost no droplets. The tiny specks seen below the interface on the smooth inner wall are static particles too small to be scavenged. High-speed movies revealed that the specks within 0.10 in. of the interface were mobile and tending to migrate back to the interface.

Figure 40 shows the configuration with both housing and shaft grooves operating with a 0.0048 in. radial clearance. Placing grooves on both the rotating and static surfaces more than doubles the pumping coefficient. The effect is somewhat as though the radial clearance were cut in half by an imaginary plane. With a reduced effective clearance, increased pumping is obtained but the level of turbulence and the tendency towards cavitation is also increased. When this same

configuration was run at a 0.003 in. clearance, the turbulence was so severe that the test was terminated without taking any microflash pictures. Upon disassembly, erosion damage was observed at the entrance to each helical channel (see Figure 41). This damage is believed to have been the result of pressure pulsations caused by the close passage of adjacent sets of lands and grooves. This damage remains visible in photographs of subsequent tests (e.g., Figures 40, 42, 43, 47, and 48). In Figure 40 the cavitation pattern, most pronounced near the interface, seems to follow the regions where the two sets of lands intersect. Figure 43 shows the same configuration with a larger 0.0067-in. radial clearance. Here the tendency toward cavitation is somewhat diminished.

Figure 42, a housing groove configuration with a 0.0051 in. radial clearance, shows the configuration and clearance adopted for the current turbine alternator assembly seal-to-space. It provides a stable interface with good scavenging and essentially no generation of liquid droplets. Figure 44 shows a shaft groove configuration operating with a 0.0067-in. radial clearance and still showing no evidence of breakdown.

It was necessary to discontinue testing at this time. Had testing continued, successively larger radial clearances would have been tested until breakdown was achieved. Based on the tests completed, however, it is clear that no signs of a breakdown condition occurred for any of the 12° helix angle configurations for radial clearance values up to 0.0067 in. The configuration selected for use in the turbine seal-to-space has been shown to be a satisfactory barrier against the loss of raw liquid.

Figures 45 through 48 show visco pumps operating at the peripheral speed representative of the SNAP-8 Mercury Motor Pump Seal-to-Space. In this application a visco pump axial length of 1-2/3 in. is available for opposing an applied pressure of 70 psia. Half of the length is held in reserve for scavenging and degradation during 10,000 hours of operation. The configuration and clearance of Figure 45 is that of the first generation of mercury PMA hardware. This configuration will be satisfactory if the small radial clearance can be maintained. The configuration of Figure 48 is to be preferred, however, since it gives the same pumping capability and a better interface with over twice the radial clearance.

6. Seal Breakdown

Incipient and complete breakdown of the visco seal was experienced for two non-optimum configurations. One configuration had a 1° helix angle and the other had a 4° helix angle.

The 1° helix angle was tested with a 0.003-in. radial clearance with good results. The expected pumping coefficient was obtained and the interface appeared to be steady and stable. The clearance was increased to 0.004 in. and the test repeated. To the eye it appeared that continuum pumping existed but the interface and flow pattern seemed to fluctuate somewhat. Operation was not as steady as observed previously. Microflash pictures revealed, however, that a condition of incipient breakdown existed. The fluctuations were apparently being caused

by voids which were forming and collapsing within the pumping continuum. As is illustrated by the polaroid microflash pictures of Figure 49, these voids tend to form on the helical lands. Figure 49a shows a few voids which have formed in the lower half of the pumping continuum. Figure 49b shows voids penetrating the entire continuum.

The 4° helix angle configuration was tested with a 0.006-in. radial clearance. Originally it had a groove depth of only 0.004 in. (optimum = 0.018 in.). This configuration exhibited complete breakdown at 12,000 rpm and incipient breakdown in the 6000 to 9000 rpm range. Figure 50 is a microflash picture of the pump operating in the complete breakdown situation. The pumping continuum and the ability of the pump to generate pressure or impede a through flow is completely destroyed. When shaft speed was reduced from 12,000 rpm to the 8500 rpm, the pumping continuum was restored and the pump generated a pressure of 4 psi while operating under a condition of incipient breakdown.

This information is reported in the hope it will contribute to the eventual understanding of the breakdown phenomenon. Breakdown is not understood at the present time and it is clear that it remains a most significant object of future research.

VI. CONCLUSIONS

A. Mercury visco pumps running at SNAP-8 turbine assembly conditions (12,000 rpm; 2-in. shaft dia; 1256 in./sec peripheral velocity) have stable liquid-vapor interfaces and exhibit no signs of breakdown for radial clearance values of 0.003 to 0.007 in.

B. Mercury visco pumps running at SNAP-8 Mercury Motor-Pump conditions (7800 rpm; 1.25-in. shaft dia; 510 in./sec peripheral velocity) have stable interfaces and exhibit no signs of breakdown for radial clearance values of 0.003 to 0.007 in.

C. Visco pumps do exhibit an edge effect wherein the performance of a pumping section with short axial engagement is not proportionate to that obtained with longer axial engagement. The nature of the edge effect varies with shaft speed. The magnitude of the edge effect is greater for the shaft groove configurations than for configurations with housing grooves or housing and shaft grooves.

D. Laminar regime pumping coefficients for the Zotov optimum configuration visco pump are 0.45 to 0.49. Turbulent pumping coefficients for the Zotov optimum configuration are defined by the relation

$$\psi = 0.313 + 4.3 \times 10^{-4} \, Re_g^{1.044}$$

Pumping coefficients for shaft groove configurations are essentially the same as those obtained for housing groove configurations. Use of both housing and shaft grooves increases pumping coefficient by a factor of 2 to 3.

E. Power loss for visco pumps of L/D>1 can be conservatively estimated by treating the pump as a smooth shaft rotating in a close clearance sleeve and by neglecting the grooves. This conclusion is true only for the shaft groove and the housing groove configurations. Use of both housing and shaft grooves results in a greater power loss.

F. The seal breakdown phenomenon has been observed to originate with voids which form on the lands. These voids form near the interface at the outset; at a more advanced state of breakdown, they extend throughout the entire pumping continuum until the pumping continuum is completely destroyed and a state of complete breakdown is achieved.

VII. RECOMMENDATIONS FOR FUTURE WORK

A. BREAKDOWN PHENOMENON

Tests should be run for viewing of the breakdown process. This should involve the following steps:

1. High-speed movie of incipient breakdown
2. High-speed movie of complete breakdown
3. Identification of breakdown speeds, pumping coefficients, and edge effects for optimum (Zotov) visco pump configuration. Data should be taken with several fluids for correlation with theoretical models of breakdown.

B. ZERO-LEAKAGE SEAL EXPERIMENT

The zero-leakage seal illustrated in Figure 51 uses ultra-low vapor pressure liquid (e.g., eutectic indium-gallium) for buffer fluid in the central herringbone visco seal. The basic experiment should involve evaluation of a triple herringbone seal in a quartz test section of the existing visco pump test rig. The center seal containing indium-gallium should be run hotter than the mercury seal and the oil seal to prevent contamination of buffer fluid by condensation. Samples of the three seal liquid inventories can be analyzed for inter-contamination after 10-hour tests.

C. HERRINGBONE VISCO BEARING

The visco bearing configuration illustrated in Figure 52 promises to be second only to the tilting pad bearing in anti-whirl stability. The center section consists of a bearing operating at a close clearance. The visco pump sections on the two ends are large clearance (0.007 in. radial) seals which apply pressure to the two grooves. These pressurized grooves assure that the bearing remains full of liquid throughout its periphery.

REFERENCES

1. H. S. Rowell and D. Finlayson, "Screw Viscosity Pumps," Engineering, 114, pp. 606-607, 17 November 1922.

2. H. S. Rowell and D. Finlayson, "Screw Viscosity Pumps," Engineering, 126, pp. 249-250, 31 August 1927.

3. H S. Rowell and D. Finlayson, "Screw Viscosity Pumps," Engineering, 216, pp. 385-387, 28 September 1928.

4. F. Lawaczeck, Turbinen und Pumpen, Berlin, 1932, p. 171.

5. E. F. Boon and S. E. Tal, "Hydrodynamic Seals for Rotating Shafts," Chemce-Ing.-Technik, 31, No. 3, pp. 202-212 (1959); Translation by R. Presser, United Kingdom Atomic Energy Authority, Risley, Warrington, Lancashire, 1961.

6. V. A. Zotov, "Research on Helical Groove Seals," Machine Design and Calculation (Russia), Issue No. 10.

7. W. T. Piggot, "Pressures Developed by Viscous Materials in the Screw Extrusion Machine," Transactions of the ASME, 73, No. 7, October 1951.

8. J. F. Carley and R. A. Strub, Industrial and Engineering Chemistry, 45, No. 5, May 1953.

9. W. K. Stair, The Visco Seal--A Survey, University of Tennessee Engineering Experiment Report No. ME-5-62-2, March 1962.

10. J. M. McGrew and J. D. McHugh "Analysis and Test of the Screw Seal in Laminar and Turbulent Operation," ASME Paper 64-LubS-7, presented at 28-30 April ASME Spring Lubrication Symposium, Cleveland, Ohio.

11. T. Asanuma, "Studies on the Sealing Action of Viscous Fluids," International Conference on Fluid Sealing, Paper A3, 17-19 April 1961, BHRA, Harlow Essex, England.

12. R. T. P. Whipple, Herringbone Pattern Thrust Bearing, UK HEA, Atomic Research Establishment, TIM-29, 24 August 1949.

13. R. T. P. Whipple, Theory of the Spiral Grooved Thrust Bearing with Liquid or Gas Lubricant, UK HEA, Atomic Research Establishment, T/R 622, 6 March 1951.

14. D. P. Hughes, Shaft Seal for High Gas Pressures, Paper C1, 17-19 April 1961, International Conference on Fluid Sealing, BHRA, Harlow, Essex, England.

15. W. Frössel, Hochtourige Schmierölpumpe," Konstrucktion, 12, No. 5, pp. 195-203 (1960).

TABLE 1

SUMMARY OF OPTIMUM GEOMETRY FOR
LAMINAR SCREW SEAL OPERATION

	ψ_ℓ (theor)	ψ_ℓ (meas)	ϕ	δ/h	$\gamma = \frac{w}{w' + w}$	h/w	Test Regimes
1. Zotov-Reference 6	0.69	0.37-0.69	14.5°	0.32	0.63	0.08	Lam & Turb ($Re_{h_{cr}} = 1300$)
2. Asanuma-Reference 11	0.45	0.33-0.36	10°~11°	0.2	0.5	0.05~0.2	Lam
3. Boon and Tal-Reference 5	0.55	------	15.8°	0.38	0.5	------	Lam
4. Frössel-Reference 15	----	0.122*	12°	0.007*	----	------	Lam
	----	0.18*	15°~20°	0.16*	----	------	Lam
5. Whipple et. al.-Reference 13	0.55	------	13.8°	0.38	0.5	------	Lam
6. Hughes, Reference 14	0.55	0.47	13.8°	0.38	0.5	0.055	Lam
7. McGrew and McHugh-Reference 10	0.61	0.313	21.6°	0.36	0.5	------	Lam & Turb
8. Present GE(ATL) Tests	0.61	0.45-0.49	21.6°	0.36	0.5	------	Lam & Turb

*Not optimum value

TABLE 2

VISCO PUMP CONFIGURATIONS TESTED AT VON KARMAN CENTER

Configuration	1	2	3	4	5	5	6	7	8	9	10	11	12
Test Fluid	Hg	Hg	Hg	Hg	ET-378	Hg	Hg	Hg	Hg	Hg	Hg	Hg	Hg
Location of Thread	Housing	Housing	Housing	Housing	Housing	Housing	Shaft	Both	Shaft	Both	Housing	Both	Shaft
Housing Diameter, in.	2.0125	2.0064	2.0125	2.0085	2.0064	2.0064	2.0070	2.0064	2.0104	2.0105	2.0105	2.0105	2.0104
Shaft Diameter, in.	2.0003	2.0003	2.0003	2.0003	2.0003	2.0003	2.0008	2.0008	2.0008	2.0008	2.0003	1.9971	1.9971
Number of Thread Starts	4	1	4	1	13	13	13	13	13	13	13	13	13
Helix Angle, degrees	4	1	4	1	12	12	12	12	12	12	12	12	12
Radial Clearance, δ in	0.006	0.003	0.006	0.004	0.003	0.003	0.003	0.0028	0.0048	0.0048	0.0051	0.0057	0.0067
Groove Depth, n, in.	0.004	0.0138	0.0123	0.0138	0.0153	0.0153	0.0143	0.0153 0.0143	0.0143	0.0133 0.0143	0.0133	0.0133 0.0124	0.0124
Groove Width, w, in.	0.0475	0.0494	0.0475	0.0494	0.0464	0.0464	0.0507	0.0464 0.0507	0.0507	0.0464 0.0507	0.0464	0.0464 0.0507	0.0507
Land Width, w', in.	0.0630	0.0494	0.0630	0.0494	0.0534	0.0534	0.0505	0.0534 0.0505	0.0505	0.0534 0.0505	0.0534	0.0534 0.0505	0.0505
Pitch, in.	0.1105	0.0988	0.1105	0.0988	0.0998	0.0998	0.1012	0.0998 0.1012	0.1012	0.0998 0.1012	0.0998	0.0998 0.1012	0.1012
Lead, in.	0.442	0.0988	0.442	0.0988	1.297	1.297	1.316	1.297 1.316	1.316	1.297 1.316	1.297	1.297 1.316	1.316
δ/h	1.5	0.217	0.488	0.290	0.196	0.196	0.210	0.189 0.196	0.336	0.361 0.336	0.383	0.504 0.540	0.540
h/w	0.084	0.279	0.259	0.279	0.329	0.329	0.281	0.329 0.281	0.281	0.287 0.281	0.287	0.287 0.244	0.244
w/w+w'	0.430	0.500	0.430	0.500	0.465	0.465	0.501	0.465 0.501	0.501	0.465 0.501	0.463	0.465 0.501	0.501
Build-Up No.	1 - 3	1 - 4	1 - 5	1 - 7	1 - 6	1 - 8	1 - 9	1 - 10	1 - 11	1 - 12	1 - 13	1 - 14	1 - 15
Micro-Flash Photo	Yes	No	No	Yes	Yes	Yes	Yes	No	Yes	Yes	Yes	Yes	Yes
High-Speed Movie No.	-	-	-	-	-	29765	-	29771	29782	-	29805	-	29816

TABLE 3

VISCO PUMP CONFIGURATIONS TESTED AT GENERAL ELECTRIC ADVANCED TECHNOLOGY LABORATORY

	Configuration		
	A	B	C
Location of Threads	Shaft	Housing	Housing
Housing Diameter, in.	-	-	-
Shaft Diameter, in.	2	2	2
Number of Thread Starts	8	8	2
Helix Angle, Degrees	14.5	14.5	4
Radial Clearance, δ, in.	0.0032	0.0032	0.0032
Groove Depth, h, in.	0.010	0.010	0.010
Groove Width, w, in.	0.122	0.122	0.136
Land Width, w', in.	0.075	0.075	0.083
Pitch, in.	0.197	0.197	0.219
Lead, in.	1.576	1.576	0.438
δ/h	0.32	0.32	0.32
h/w	0.082	0.082	0.074
$w/w + w'$	0.62	0.62	0.62

TABLE 4

DATA SUMMARY SHEET

Configuration Number	B-U No.	N rpm	Δp psi	L in.	T °F	μ lb-sec/in.² x 10⁻⁷	ω sec⁻¹	δ in.	rL/δ² x 10⁴	Δp/μω x 10⁴	Δpδ²/μrωL	ν in.²/sec x 10⁻⁴	rωδ/ν x 10³	Δpδ/μωr	L/δ	Comments
1	1-3	11200	0	0.5	-	1.85	1173	0.006	1.39	0	0	1.47	47.9	0	83.3	Mercury - 4° helix angle
1	1-3	7500	4	0.35	170-200	1.89-1.81	785	-	0.973	2.755	2.83	1.5-1.45	32.1	165.3	58.3	Mercury - 4° helix angle
2	1-4	11200	13	0.5	170	1.89	1173	0.003	5.55	5.86	1.055	1.5	23.45	-	167	Mercury - 1° helix angle
3	1-5	11120	7	0.3	190	1.84	1165	0.006	0.834	3.26	3.91	1.47	47.6	195.8	50	Mercury - 4° helix angle
		11480	9.5	0.25	150	1.95	1202		0.695	4.05	5.83	1.55	46.5	245	41.7	
		11300	12.5	0.3	190	1.84	1183		0.834	5.73	6.87	1.47	48.25	344	50	
3	1-5	11300	20.5	0.5	190-215	1.84-1.77	1183	0.006	1.39	9.62	6.92	1.47-1.42	49.1	577	83.3	Mercury - 4° helix angle
4	1-7	12150	3	0.5	140	1.98	1272	0.004	3.12	1.19	0.381	1.57	32.4	47.6	125	Mercury - 1° helix angle
		12150	4	0.62	173	1.88	1272		3.87	1.67	0.431	1.50	33.9	66.8	155	
		12150	8.5	0.65	200	1.81	1272		4.06	3.69	0.908	1.45	35.1	147.6	162.5	
		12090	19.6	0.94	245	1.70	1266		5.87	9.10	1.55	1.37	36.95	364	235	
		12000	37	1.8-2.0	264	1.66	1256		11.25-12.5	17.75	1.58-1.42	1.34	37.5	711	450-500	
		12200	0	0	185	1.85	1278		0	0	0	1.48	34.5	0	0	
		12200	0	0	170	1.89	1278		0	0	0	1.51	33.85	0	0	
		8850	27.7	1.8	163	1.91	926		11.25	15.65	1.39	1.52	24.4	626	450	
		8850	12.0	1.4	158	1.93	926		8.75	6.70	0.765	1.53	24.2	268	350	
		8850	9.8	1.15	150	1.95	926		7.19	5.42	0.755	1.55	23.9	217	287.5	
		8850	2.4	0.25	128	2.02	926		1.56	1.285	0.821	1.60	23.15	51.3	62.5	
		6225	2.2	0.29	110	2.075	652		1.81	1.628	0.899	1.65	15.8	65.1	72.5	
		6225	4.4	0.5	113	2.07	652		3.12	3.26	1.045	1.64	15.9	130.5	125	
		6300	4.6	0.8	115	2.06	660		5.00	3.38	0.675	1.64	16.1	135.2	200	
		5925	5.2	1.0	117	2.05	620		6.25	4.09	0.655	1.63	15.22	163.6	250	
		6150	8.2	1.25	123	2.03	644		7.81	6.08	0.804	1.61	16.0	251	312.5	
4	1-7	6300	11.0	1.8	123	2.03	660	0.004	11.25	8.20	0.779	1.51	16.4	328	450	Mercury - 1° helix angle
5	1-6	12400	20	0.25	176	16.5	1299	0.003	2.78	0.934	0.336	150	0.26	28	83.3	ET-378 - 12° helix angle
			30	0.36	179	15.7			4.00	1.47	0.367	142	0.274	44.1	120	
			40	0.50	182	15.0			5.55	2.05	0.370	138	0.282	61.5	167	
			50	0.60	184	14.6			6.66	2.64	0.396	132	0.295	79.1	200	
			60	0.70	185	14.5			7.77	3.19	0.410	130	0.30	95.7	233	
			60.5	0.70	185	14.5			7.77	3.21	0.413	130	0.30	96.3	233	
5	1-6	12400	66	0.77	187	13.8	1299	0.003	8.55	3.69	0.431	127	0.30	110.8	256.5	ET-378 - 12° helix angle
5	1-8	11700	9	0.06	185	1.85	1225	0.003	0.666	3.97	5.96	1.48	24.85	119	20	Mercury - 12° helix angle (housing grooves)
			19	0.10	225	1.75			1.11	8.86	7.98	1.40	26.25	266	33.3	
			30	0.13	253	1.68			1.44	14.58	10.12	1.36	27.0	437	43.3	
			44	0.175	282	1.62			1.94	22.15	11.42	1.32	27.85	664	58.3	
			60	0.23	296	1.60			2.56	30.60	11.95	1.30	28.3	918	76.7	
			22	0.11	255	1.68			1.22	10.70	8.77	1.35	27.2	321	36.7	
			80	0.30	290	1.61			3.33	40.60	12.18	1.31	28.05	1218	100	
			99	0.39	300	1.59			4.33	50.80	11.72	1.29	28.5	1523	130	
			70	0.27	265	1.66			3.00	34.40	11.47	1.34	27.4	1032	90	
			90	0.34	263	1.66			3.78	44.20	11.70	1.34	27.4	1326	113.3	
		11700	117	0.50	267	1.66	1225		5.55	57.50	10.36	1.34	27.4	1725	167	
		9000	27	0.1	155	1.94	942		1.11	14.8	13.33	1.54	18.55	444	33.3	
			37.5	0.2	162	1.92			2.22	20.7	9.32	1.52	18.6	621	66.7	
			47	0.3	173	1.88			3.33	26.5	7.95	1.52	18.6	795	100	
			69	0.4	175	1.88			4.44	39.0	8.78	1.50	18.85	1170	133	
			76	0.5	180	1.86			5.55	43.3	7.80	1.50	18.85	1300	167	
		9000	85.5	0.6	1.86	1.85	942		6.66	49.0	7.35	1.48	19.1	1470	200	
		6000	11	0.1	133	2.0	628		1.11	8.75	7.88	1.59	11.85	262	33	
			16	0.2	135	2.0			2.22	12.73	5.73	1.59	11.85	382	67	
			20.5	0.3	137	1.99			3.33	16.4	4.92	1.58	11.93	498	100	
			24	0.4	137	1.99			4.44	19.2	4.32	1.58	11.93	576	133	
			25	0.5	137	1.99			5.55	23.2	4.18	1.58	11.93	696	167	
5	1-8	6000	39.2	0.6	138	1.99	628	0.003	6.66	31.4	4.71	1.58	11.93	942	200	Mercury - 12° helix angle (housing grooves)
6	1-9	12020	11	0.15	155	1.94	1260	0.003	1.67	4.50	2.69	1.54	24.55	135	50	Mercury - 12° helix angle (shaft grooves)
		12030	20	0.19	217	1.77	1260		2.11	8.96	4.25	1.42	26.6	269	63.3	
		11920	29.7	0.25	270	1.65	1250		2.78	14.40	5.18	1.33	28.2	432	83.3	
		11990	40	0.27	281	1.63	1255		3.00	19.55	6.51	1.32	28.5	586	90	
		11980	50	0.3	282	1.63	1253		3.33	24.45	7.34	1.32	28.5	733	100	
			60	0.33	278	1.63			3.67	29.4	8.01	1.32	28.5	882	110	
			70	0.355	283	1.62			3.945	34.5	8.74	1.31	28.7	1035	118.3	
			90	0.38	287	1.61			4.22	44.6	10.56	1.31	28.7	1338	126.7	
6	1-9	11980	110	0.50	287	1.61	1253	0.003	5.55	54.5	9.81	1.31	28.7	1635	167	Mercury - 12° helix angle (shaft grooves)

Table 4
Sheet 1

Report No. 2808, Vol. I

TABLE 4 (cont.)

Configuration Number	B-U No.	N rpm	Δp psi	L in.	T °F	μ lb-sec/in.² x 10⁻⁷	ω sec⁻¹	δ in.	rL/δ² x 10⁴	Δp/μω x 10⁻⁴	Δpδ²/μωL	ν in.²/sec x 10⁻⁴	rωδ/ν x 10³	Δpδ/μωr	L/δ	Comments
6	1-9	12000	2	0	130	2.01	1256	0.003	0	0.792	∞	1.60	23.55	23.7	0	Mercury - 12° helix angle (shaft grooves)
		9000	10.5	0.2	177	1.87	942		2.22	5.95	2.68	1.49	18.95	178	66.6	
			20	0.22	165	1.91			2.44	11.1	4.55	1.52	18.6	333	73.3	
			30	0.28	167	1.90			3.11	16.8	5.40	1.51	18.7	504	93.3	
			40	0.35	170	1.90			3.89	22.35	5.75	1.50	18.8	670	116.7	
		9000	69	0.52	170	1.90	942		5.78	38.5	6.56	1.50	18.8	1155	173.2	
		6300	13.5	0.2	132	2.00	660		2.22	10.22	4.60	1.59	12.46	307	66.7	
		6300	22.5	0.25	130	2.01	660		2.78	16.95	6.09	1.60	12.38	509	83.3	
		6220	31	0.35	128	2.02	651		3.89	23.6	6.06	1.60	12.2	708	116.7	
		6220	38	0.42	126	2.03	651		4.67	28.8	6.16	1.61	12.14	864	140	
		6150	47	0.52	126	2.03	644		5.78	36.0	6.22	1.61	12.00	1080	173.2	
		7860	55	0.50	145	1.97	823		5.55	34.0	6.12	1.58	15.82	1020	167	
	1-9	12120	106	0.50	280	1.83	1270	0.003	5.55	51.1	9.21	1.32	28.85	1533	167	Mercury - 12° helix angle (shaft grooves)
7	1-10	12000	145	0.12 | 0.21	285	1.82	1256	0.0028	1.53 | 2.68	91.4	40.1 | 22.9	1.31	26.85	1720	42.9 | 75	Mercury - 12° helix angle (housing and shaft grooves)
		12100	80	0.1 | 0.16	278	1.83	1267		1.276 | 2.04	38.8	30.4 | 19.0	1.32	26.85	1087	35.7 | 57.1	
		12080	90	0.1 | 0.18	283	1.82	1265		1.276 | 2.295	43.9	34.4 | 19.1	1.31	27.05	1230	35.7 | 64.3	
		12080	50	0.07 | 0.12	255	1.88	1265		0.769 | 1.53	23.5	30.7 | 15.35	1.35	26.25	658	21.4 | 42.9	
		12080	110	0.11 | 0.2	285	1.82	1265		1.403 | 2.55	53.6	38.2 | 21.0	1.31	27.05	1500	39.3 | 71.5	
7	1-10	12130	20	0.04 | 0.1	162	1.92	1270	0.0028	0.510 | 1.275	8.2	10.1 | 5.43	1.52	23.40	230	14.3 | 35.7	Mercury - 12° helix angle (housing and shaft grooves)
8	1-11	11990	21	0.35	232	1.73	1255	0.0048	1.52	9.66	6.35	1.39	43.3	464	72.9	Mercury - 12° helix angle (shaft grooves)
		12020	10	0.31	200	1.81	1260		1.345	4.38	3.26	1.45	41.7	210	64.6	
		11980	30	0.40	165	1.91	1253		1.735	12.52	7.21	1.52	39.6	601	83.3	
		11980	40	0.48	250	1.69	1253		2.08	18.9	9.08	1.36	44.2	908	100	
		11980	50	0.51	273	1.64	1253		2.21	24.3	11.0	1.33	45.2	1167	106.2	
		11970	61	0.52	275	1.64	1252		2.26	29.7	13.13	1.33	45.2	1427	108.3	
		11990	2	0	250	1.69	1255		0	.943	∞	1.36	44.3	45	0	
		8980	10	0.30	192	1.83	940		1.30	5.81	4.47	1.40	30.9	279	62.5	
		8970	22	0.4	185	1.85	939		1.735	12.67	7.30	1.48	30.4	608	83.3	
		8965	35	0.5	190	1.84	939		2.17	20.25	9.32	1.47	30.3	972	104.2	
		9080	60	0.68	190	1.84	950		2.95	34.4	11.66	1.47	31.0	1652	141.7	
		9070	70	0.75	194	1.83	950		3.25	40.25	12.40	1.47	31.2	1933	156.2	
		6100	11.5	0.30	160	1.92	639		1.30	9.37	7.21	1.53	20.05	450	62.5	
		6100	19	0.40	145	1.97	639		1.735	15.1	8.70	1.56	19.65	725	83.3	
		5980	70	1.42	130	2.01	626		6.16	55.6	9.02	1.60	18.80	2640	296	
		6000	28	0.6	130	2.01	628		2.60	22.2	8.54	1.60	18.85	1067	125	
9	1-11	6000	23.8	0.5	128	2.02	628	0.0048	2.17	18.8	8.65	1.60	18.85	903	104.2	Mercury - 12° helix angle (shaft grooves)
9	1-12	12000	11	0.10	160	1.92	1256	0.0048	0.434	4.56	10.50	1.53	39.4	219	20.8	Mercury - 12° helix angle (housing and shaft grooves)
		12000	20	0.12	225	1.75	1256		0.520	9.10	17.50	1.40	43.1	437	25	
		11980	50	0.15	295	1.60	1253		0.651	24.9	38.25	1.30	46.3	1195	31.2	
		11970	80	0.21	290	1.61	1252		0.911	39.7	43.6	1.31	45.9	1707	43.75	
		6100	51	0.34	145	1.97	639		1.475	40.5	27.45	1.56	19.67	1945	70.8	
		6000	80	0.51	135	2.00	628		2.645	63.7	24.05	1.59	18.95	3060	127	
9	1-12	6000	20	0.15	145	1.97	628	0.0048	0.751	16.2	24.9	1.56	19.32	778	31.2	Mercury - 12° helix angle (shaft grooves)
10	1-13	6000	10	0.18	100	2.11	628	0.0051	0.693	7.54	10.88	1.68	19.1	384	35.3	Mercury - 12° helix angle (housing grooves)
			20	0.40	100	2.11			1.54	15.1	9.80	1.68	19.1	770	73.5	
			30	0.7	110	2.07			2.69	23.1	8.58	1.65	19.43	1178	137.2	
			50	1.2	120	2.04			4.61	39.0	8.45	1.62	19.8	1990	235	
		6000	10	1.5	125	2.03	628		5.77	47.0	8.14	1.61	19.9	2400	290	
		9000	12	0.17	135	2.00	942		0.654	5.83	8.91	1.59	30.2	297	33.3	
			20	0.20	150	1.92			0.770	11.05	14.34	1.53	31.4	593	33.2	
			40	0.41	175	1.88			1.58	22.6	14.30	1.50	32.0	1152	80.4	
			60	0.65	180	1.86			2.50	36.3	13.72	1.49	32.25	1750	127.5	
			80	0.87	190	1.84			3.35	46.1	13.77	1.47	32.7	2350	170.6	
		9000	100	1.10	195	1.82	942		4.23	58.25	13.77	1.46	32.9	2970	214	
		12000	10	0.14	190	1.84	1256		0.539	4.33	8.03	1.47	43.5	221	27.45	
			20	0.18	210	1.78			0.693	8.95	12.90	1.43	44.75	456	35.3	
			30	0.21	240	1.71			0.808	14.0	17.32	1.38	46.4	714	41.2	
			50	0.30	265	1.66			1.15	24.0	20.85	1.34	47.75	1225	53.9	
			70	0.41	280	1.63			1.58	34.2	21.6	1.32	48.5	1745	80.3	
			90	0.51	295	1.60			1.96	44.8	22.9	1.30	49.2	2285	100	
			110	0.68	305	1.58			2.62	55.5	21.2	1.29	49.6	2830	133.2	
10	1-13	12000	2	0	100	2.11	1256	0.0051	0	0.754	∞	1.68	38.1	38.4	0	Mercury - 12° helix angle (housing grooves)

Table 4
Sheet 2

TABLE 4 (cont.)

Configuration Number	B-U No.	N rpm	Δp psi	L in.	T °F	μ lb-sec/in.² x 10⁻⁷	ω sec⁻¹	δ in.	rL/δ² x 10⁴	Δp/μω x 10⁴	Δpδ²/μrωL	ν in.²/sec x 10⁻⁴	rωδ/ν x 10³	Δpδ/μωr	L/δ	Comments
11	1-14	9000	10	0.1	182	1.86	942	0.0067	0.223	5.7	25.6	1.48	42.6	382	14.9	Mercury - 12° helix angle (housing and shaft grooves)
			36.2	0.2	203	1.80			0.446	21.35	47.8	1.44	43.8	1430	29.9	
			62.1	0.3	200	1.81			0.669	36.4	54.4	1.45	43.55	2440	44.8	
			77.5	0.4	195	1.82			0.892	45.2	50.7	1.46	43.2	3030	59.7	
			94.2	0.5	195	1.82			1.115	54.9	49.2	1.46	43.2	3680	74.6	
		9000	111	0.6	195	1.82	942		1.34	64.7	48.3	1.46	43.2	4330	89.5	
		6100	8.8	0.1	145	1.97	639		0.223	7.0	31.4	1.56	27.45	469	14.9	
		6100	21.5	0.2	143	1.97	639		0.446	17.1	38.3	1.57	27.25	1146	29.9	
		6000	29	0.3	140	1.98	628		0.669	23.3	34.9	1.57	26.8	1562	44.8	
			36	0.4	135	2.00			0.892	28.65	32.1	1.58	26.65	1920	59.7	
			42.8	0.5	130	2.01			1.115	33.9	30.4	1.60	26.3	2270	74.6	
			48.5	0.6	130	2.01			1.34	38.5	28.7	1.60	26.3	2580	89.5	
			70	0.88	125	2.03			1.96	54.9	28.0	1.61	26.15	3680	131.2	
			90	1.15	125	2.03			2.56	70.6	27.6	1.61	26.15	4730	171.6	
		6000	100	1.3	125	2.03	628		2.90	78.5	27.1	1.61	26.15	5260	194	
		12000	10.5	0.12	185	1.85	1256		0.268	4.51	16.82	1.48	56.9	302	17.9	
			20	0.14	210	1.78			0.312	8.94	28.65	1.43	58.9	599	20.9	
			40	0.18	250	1.69			0.401	18.85	47.0	1.36	61.9	1263	26.9	
			81.5	0.23	285	1.62			0.535	40.1	75.0	1.31	64.2	2690	34.3	
			100	0.28	295	1.60			0.634	49.8	78.6	1.30	64.75	3335	41.8	
			120	0.31	310	1.57			0.691	60.8	87.9	1.28	65.75	4070	46.2	
11	1-14	12000	2	0	210	1.78	1256	0.0067	0	0.894	∞	1.43	58.9	60	0	Mercury - 12° helix angle (housing and shaft grooves)
12	1-15	12000	120	1.08	330	1.54	1256	0.0067	2.41	62.0	25.7	1.26	66.8	4155	161.2	Mercury - 12° helix angle (shaft grooves)
			102	0.90	320	1.55			2.01	52.4	26.1	1.77	66.3	3510	134.3	
			82.5	0.8	300	1.59			1.78	41.3	23.2	1.29	65.25	2770	119.4	
			60	0.7	255	1.68			1.56	28.45	18.25	1.35	62.3	1908	104.5	
			44	0.6	225	1.75			1.34	20.0	14.92	1.40	60.1	1340	89.6	
		12000	15	0.35	160	1.92	1256		0.780	6.21	7.96	1.53	55.0	416	52.2	
		9000	70	1.2	170	1.89	942		2.68	39.3	14.67	1.51	41.8	2635	179	
			58.5	1.0	170	1.89			2.23	32.8	14.72	1.51	41.8	2200	149.2	
			42	0.8	168	1.90			1.78	23.45	13.18	1.51	41.8	1572	119.4	
		9000	30	0.6	165	1.91	942		1.34	16.7	12.47	1.52	41.5	1120	89.6	
		6000	27	1.0	130	2.01	628		2.23	21.4	9.59	1.60	26.3	1434	149.2	
			22.5	0.8	128	2.02			1.78	17.75	9.97	1.60	26.3	1190	119.4	
			20	0.7	125	2.03			1.56	15.7	10.06	1.61	26.1	1052	104.5	
			17	0.6	125	2.03			1.34	13.33	9.94	1.61	26.1	894	89.6	
			15	0.5	125	2.03			1.115	11.76	10.53	1.61	26.1	788	74.6	
		6000	10	0.3	125	2.03	628		0.669	7.85	11.74	1.61	26.1	526	44.8	
12	1-15	12000	2	0	125	2.03	1256	0.0067	0	0.784	∞	1.61	52.2	52.5	0	Mercury - 12° helix angle (shaft grooves)

TABLE 5

SHAFT SURFACE SPEED (IN./SEC) AT BREAKDOWN*

	Configuration			
Fluid	A (D = 1 in., Ref. 10)	A (D = 2 in.)	B (D = 2 in.)	C (D = 2 in.)
SF96-2	290	< 330	< 460	< 710
SF96-5	198-592	< 136	< 262	< 290
Water	1160	1060	1100	1090
Mercury	-	>1380	>1380	>1380

*As evidenced by loss of liquid.

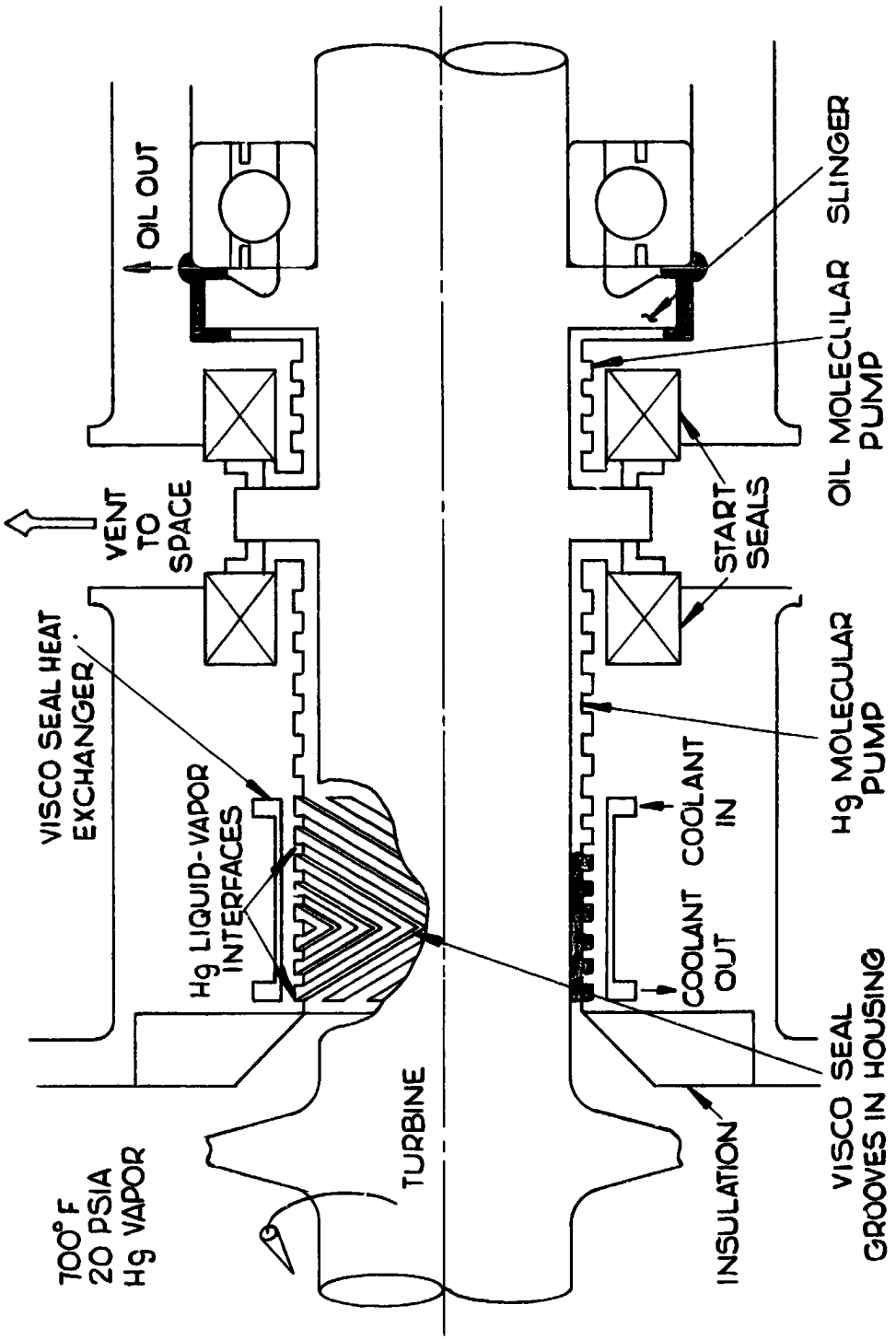

Advanced Configuration - SNAP-8 Seal-To-Space

Figure 1

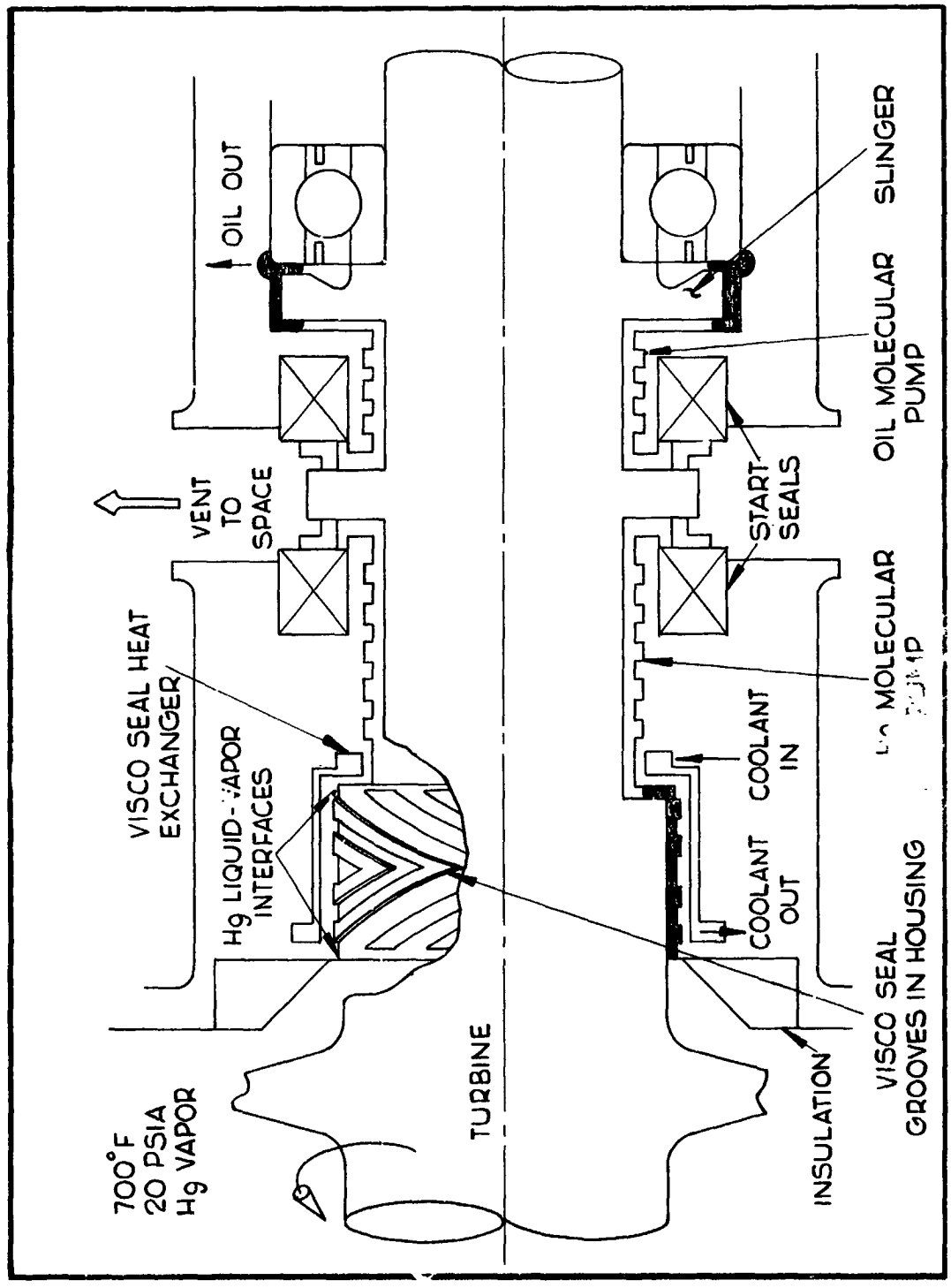

Figure 2

Current Configuration - SNAP-8 Seal-To-Space

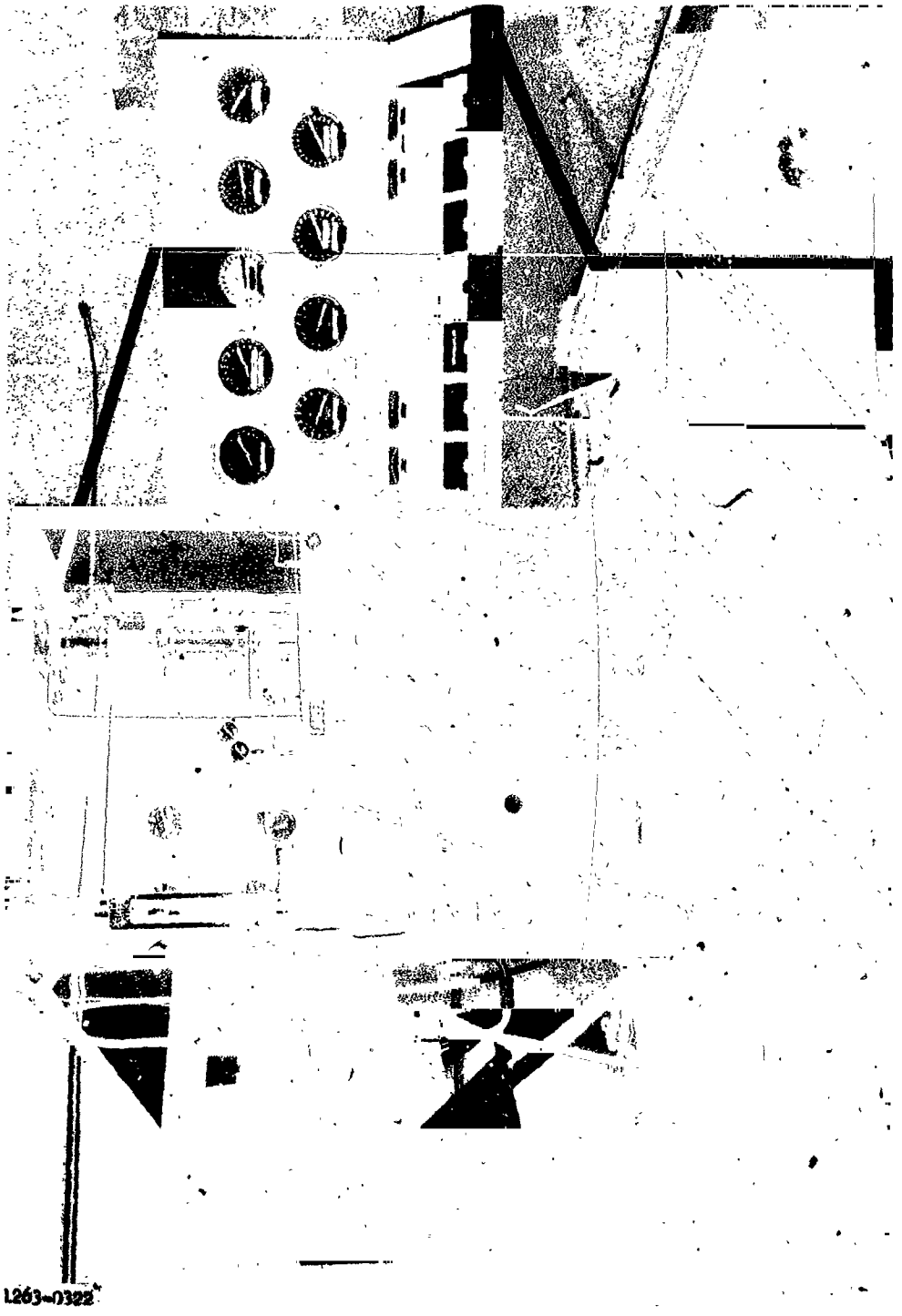

AGC Visco Pump Test Console

Figure 3

AGC Visco Pump Test Rig

Figure 4

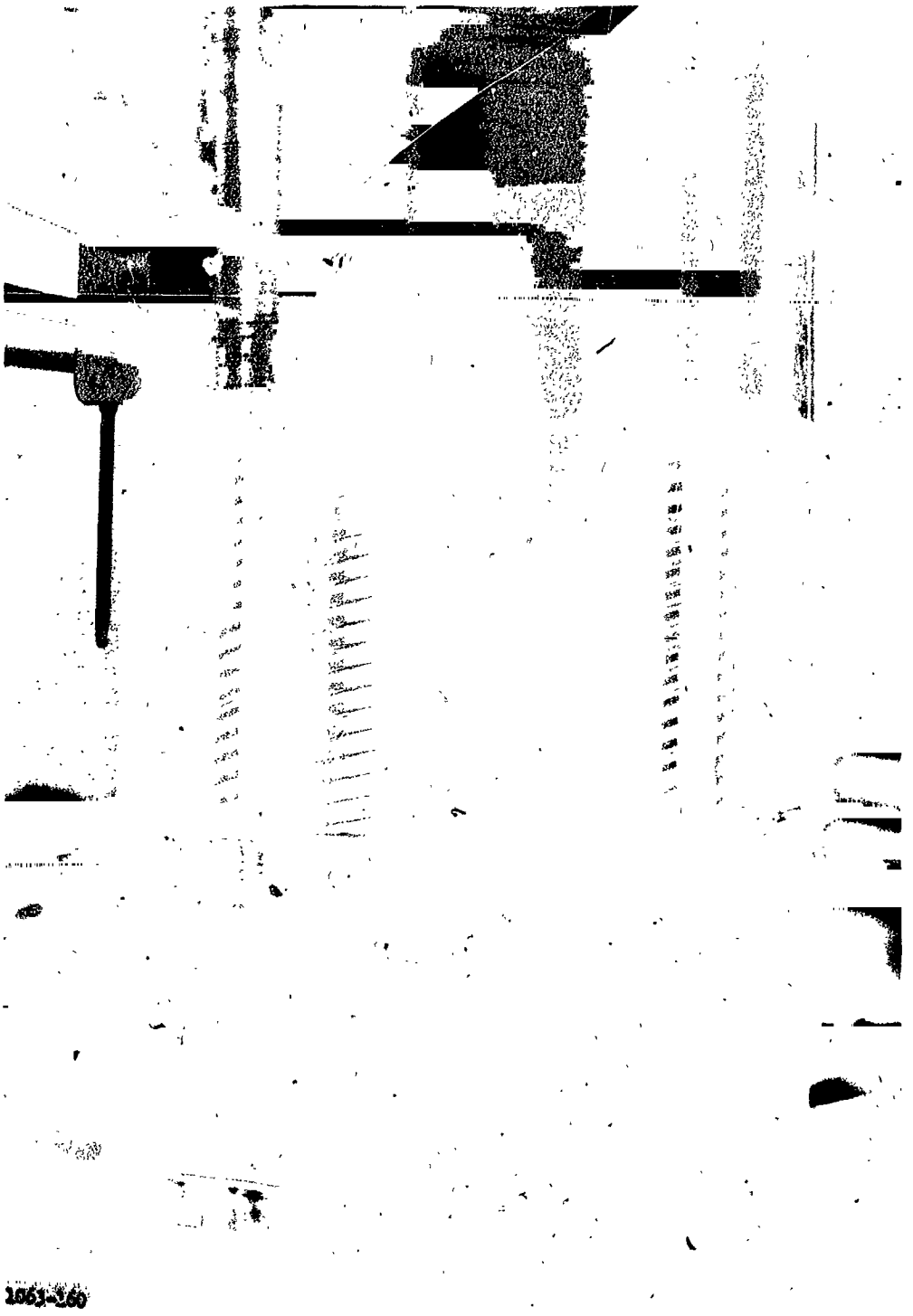

Visco Pump Test Section

Figure 5

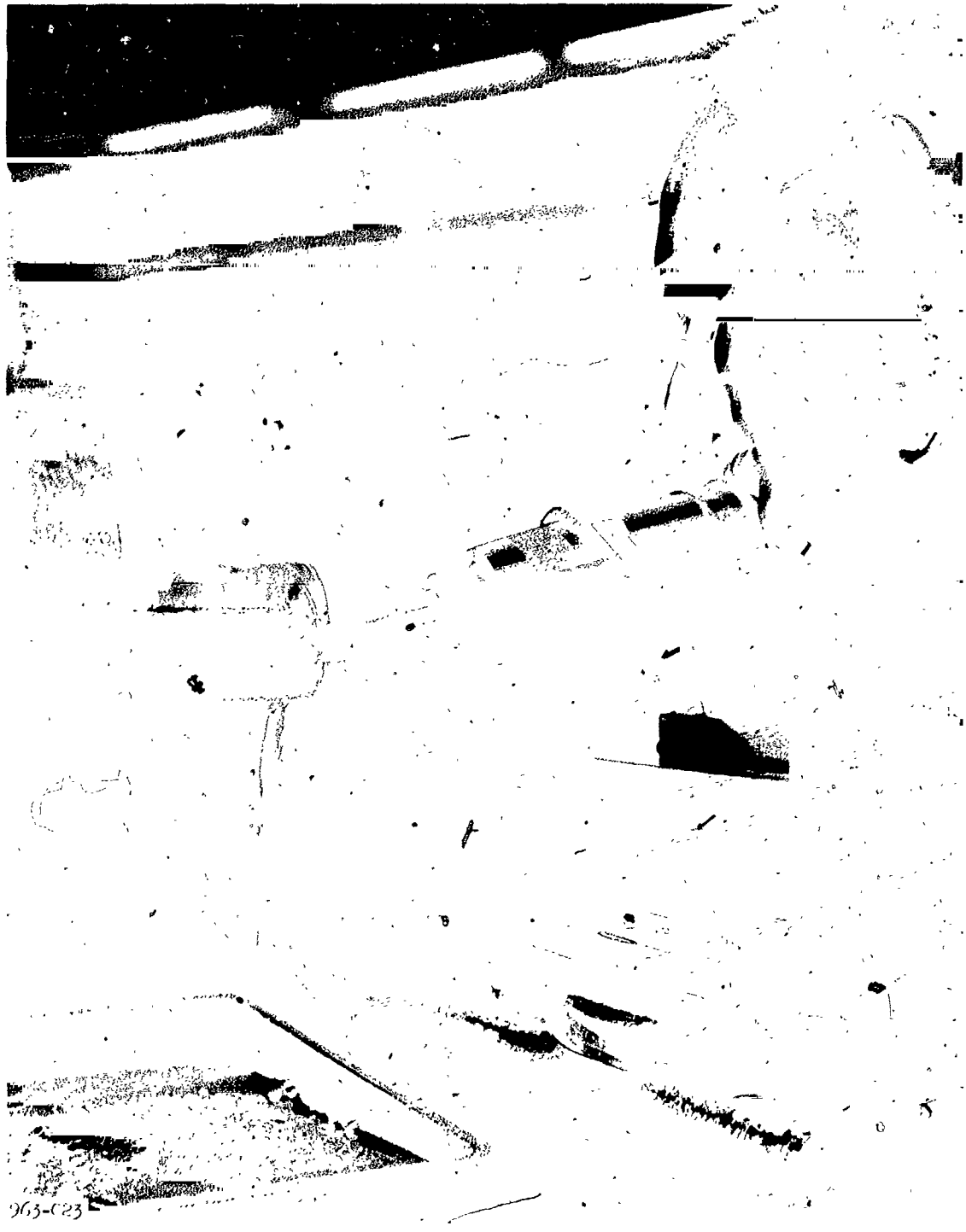

Machining of Transparent Quartz Housing

Figure 6

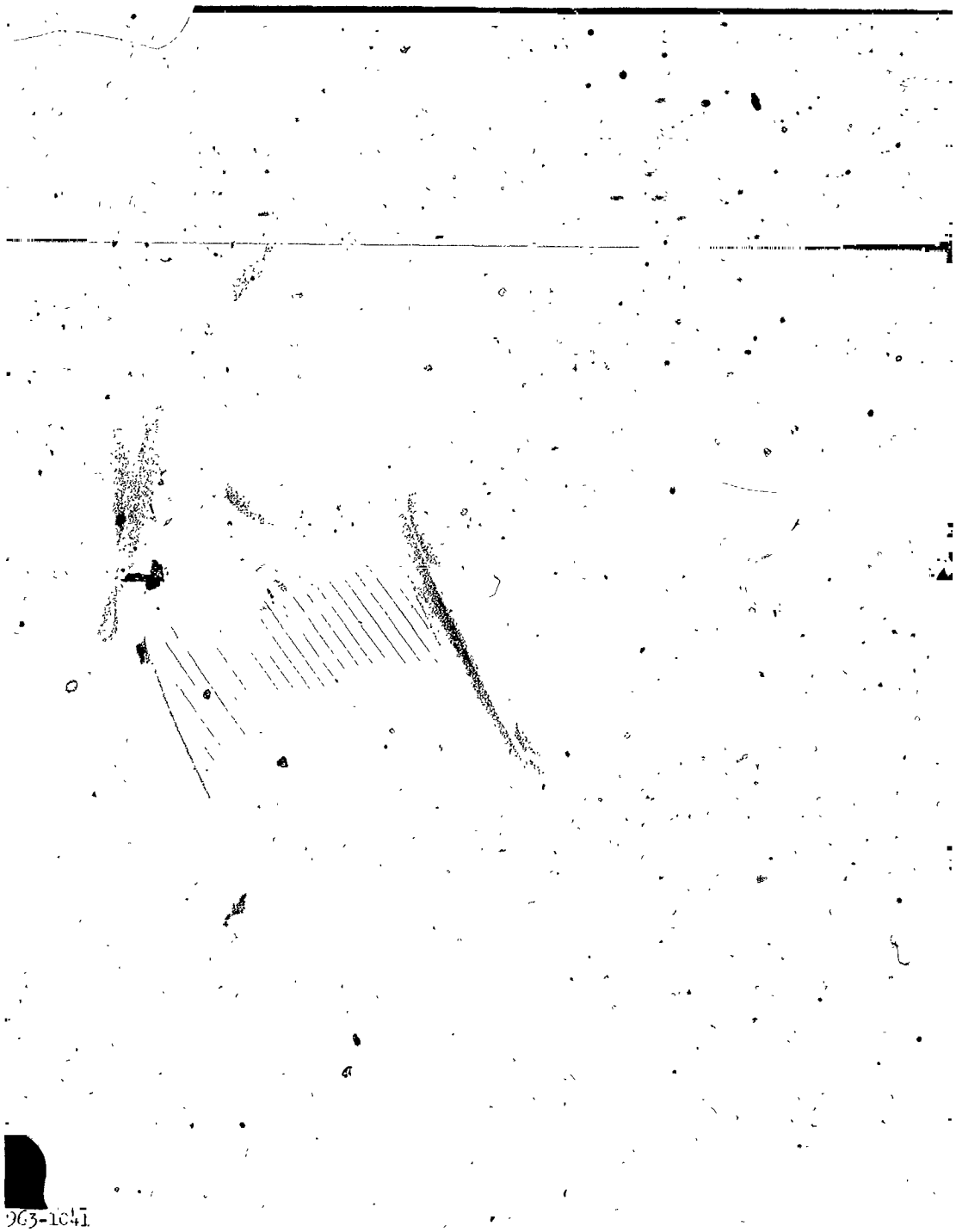

Figure 7

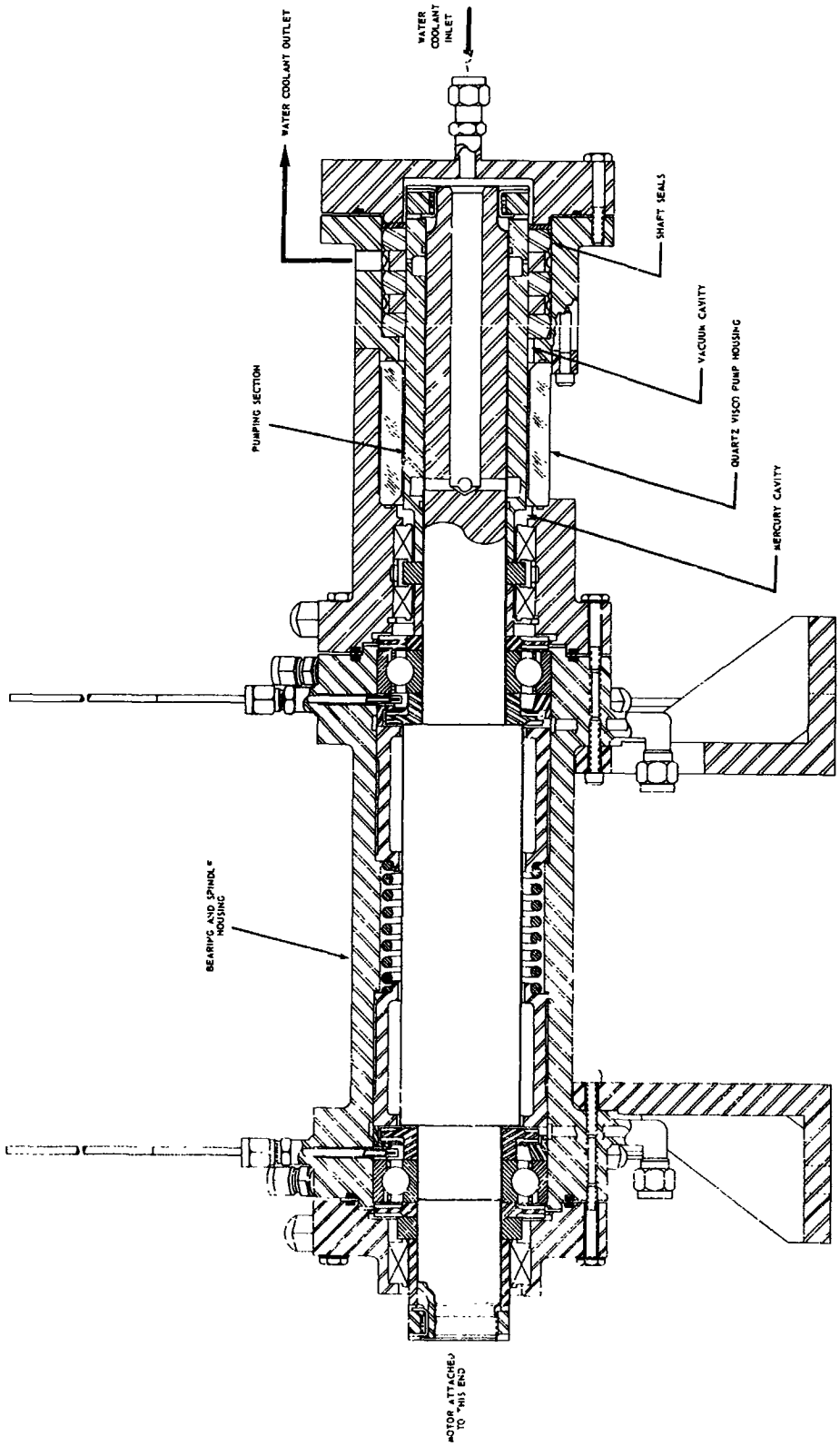

Visco Pump Test Rig - Assembly Drawing

Figure 8

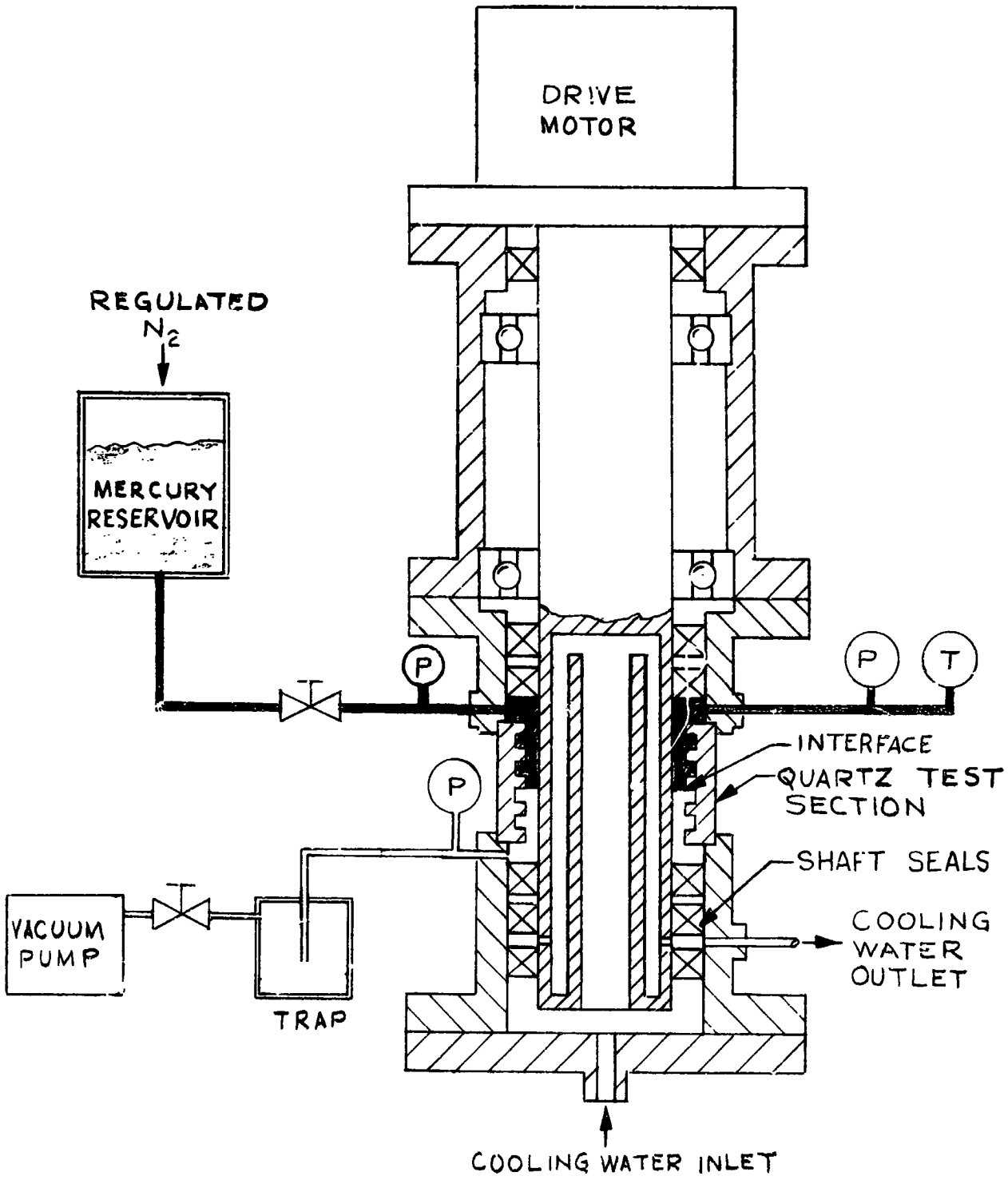

Schematic of Test Arrangement

Figure 9

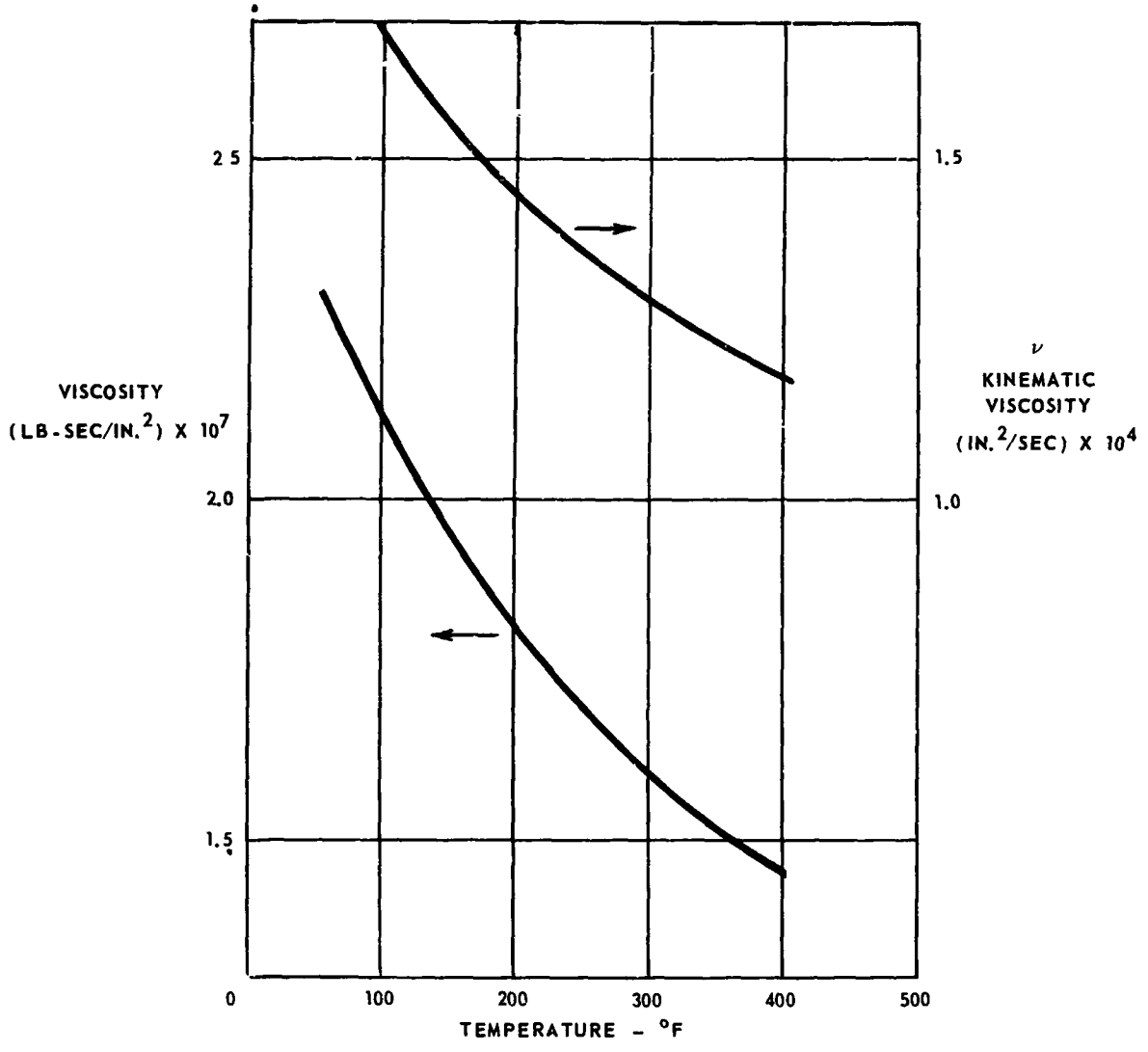

REF: LIQUID METALS HANDBOOK

Viscosity of Liquid Mercury

Figure 10

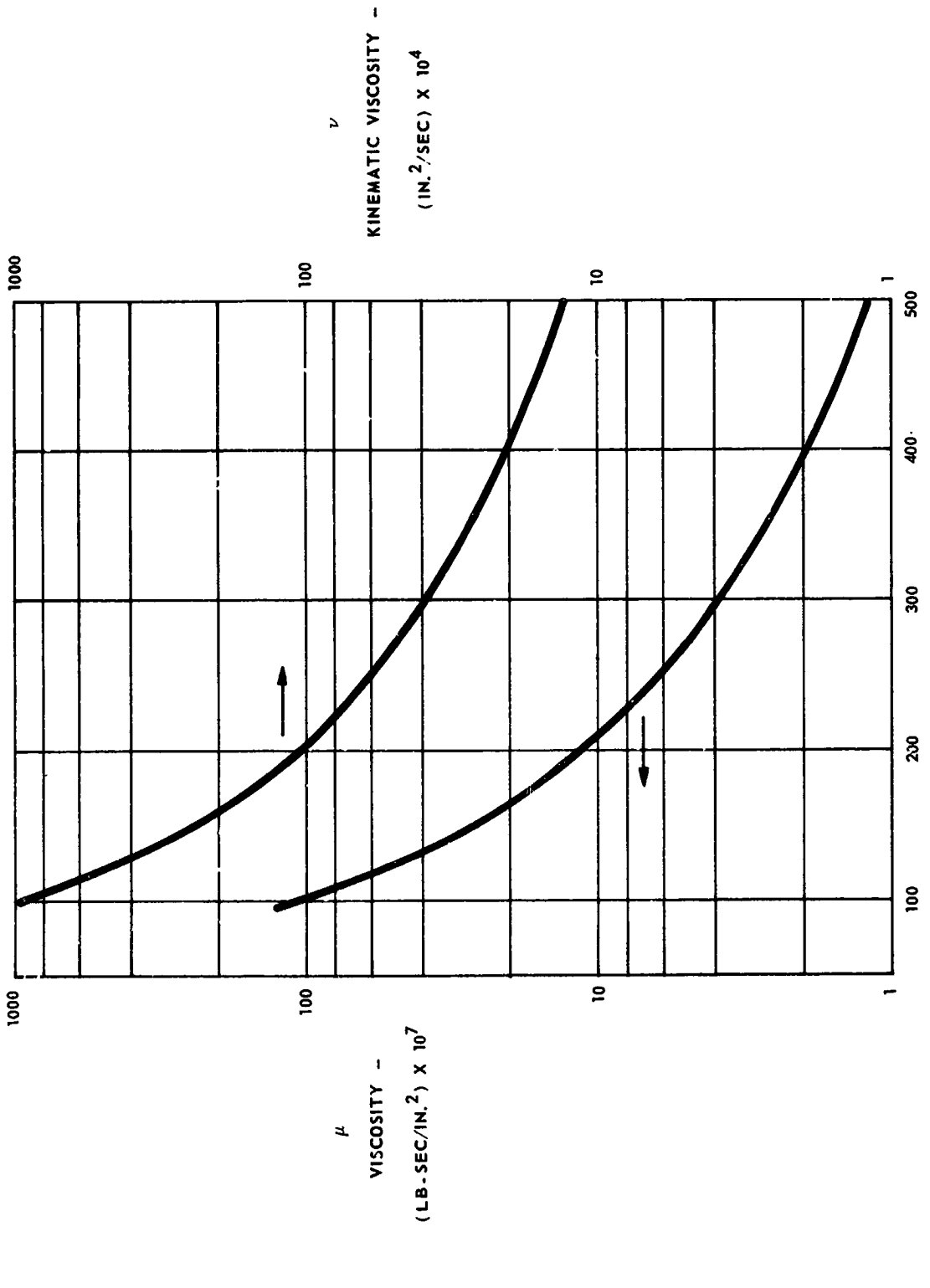

Viscosity of Liquid ET-378 Polyphenyl Ether

Figure 11

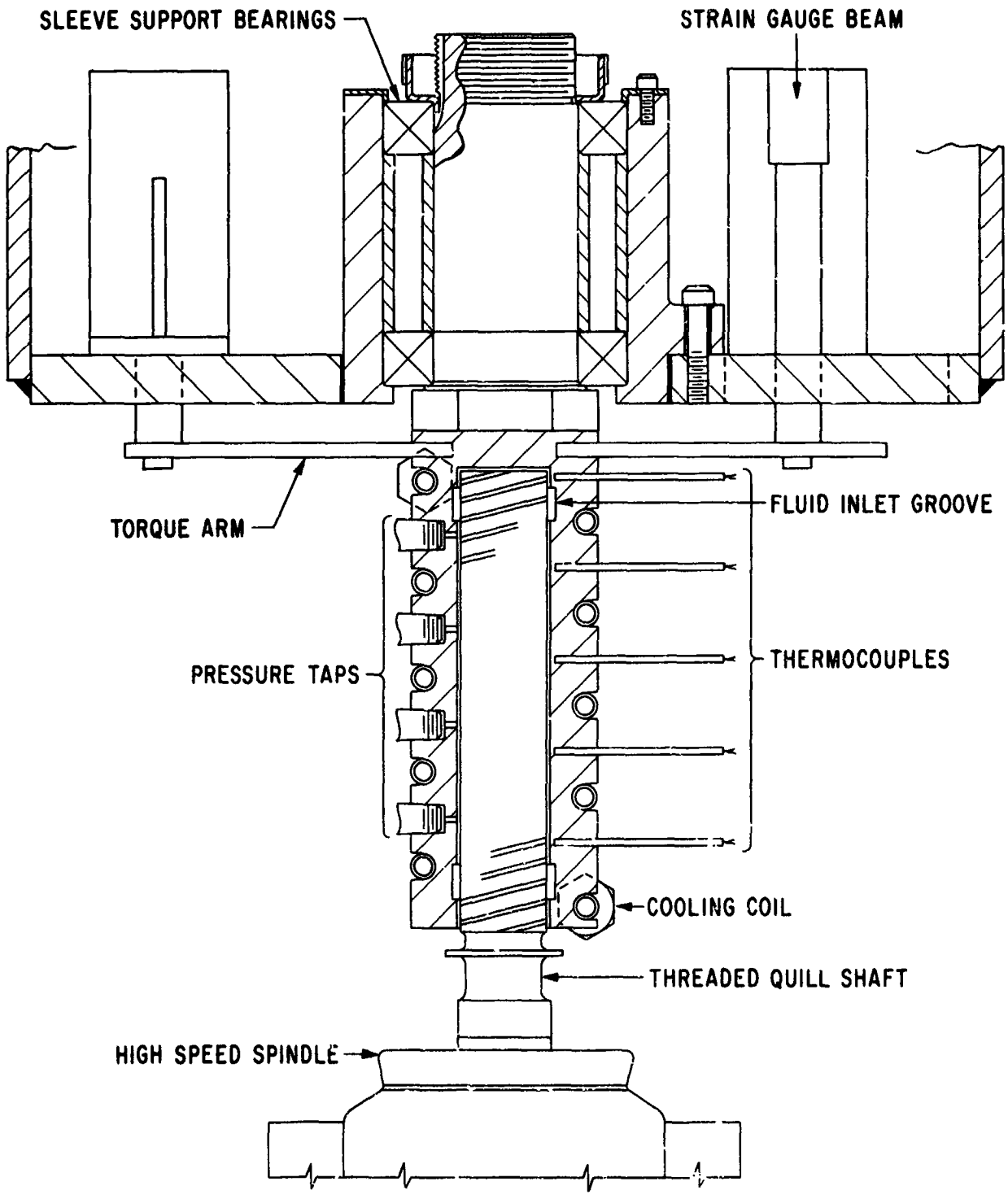

Test Rig Layout

Figure 12

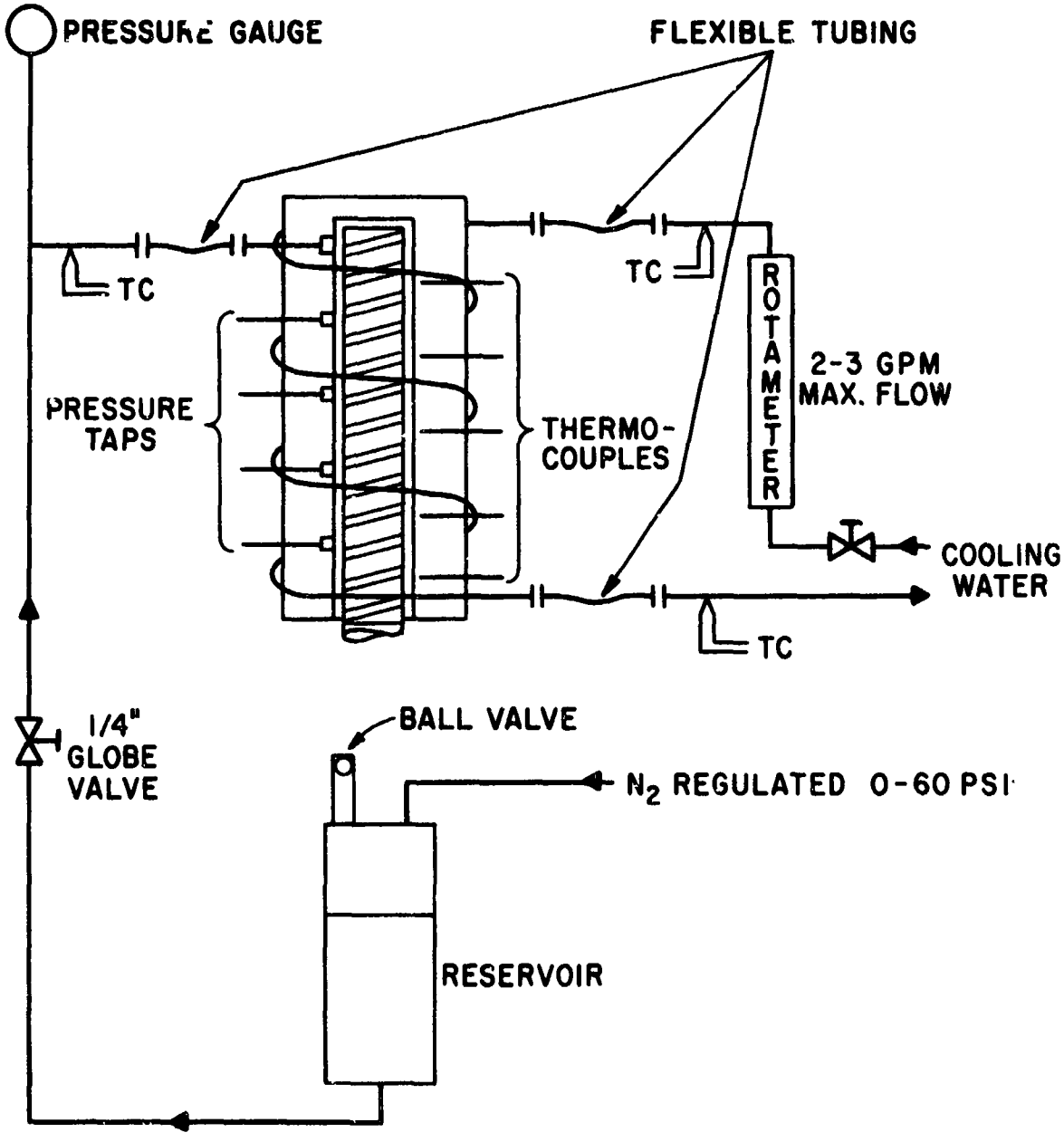

Test Loop and Instrumentation

Figure 13

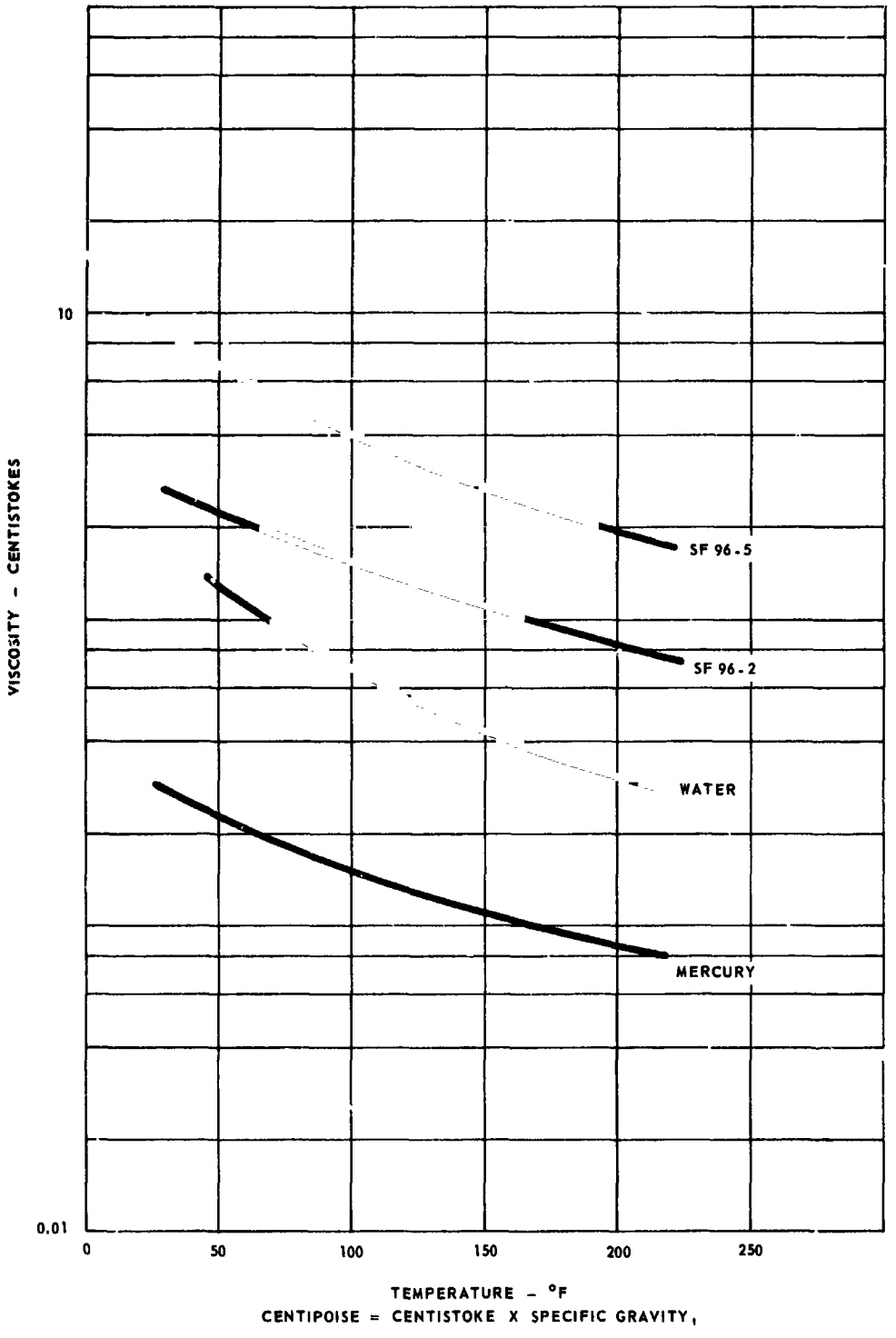

Viscosity of Test Liquids

Figure 14

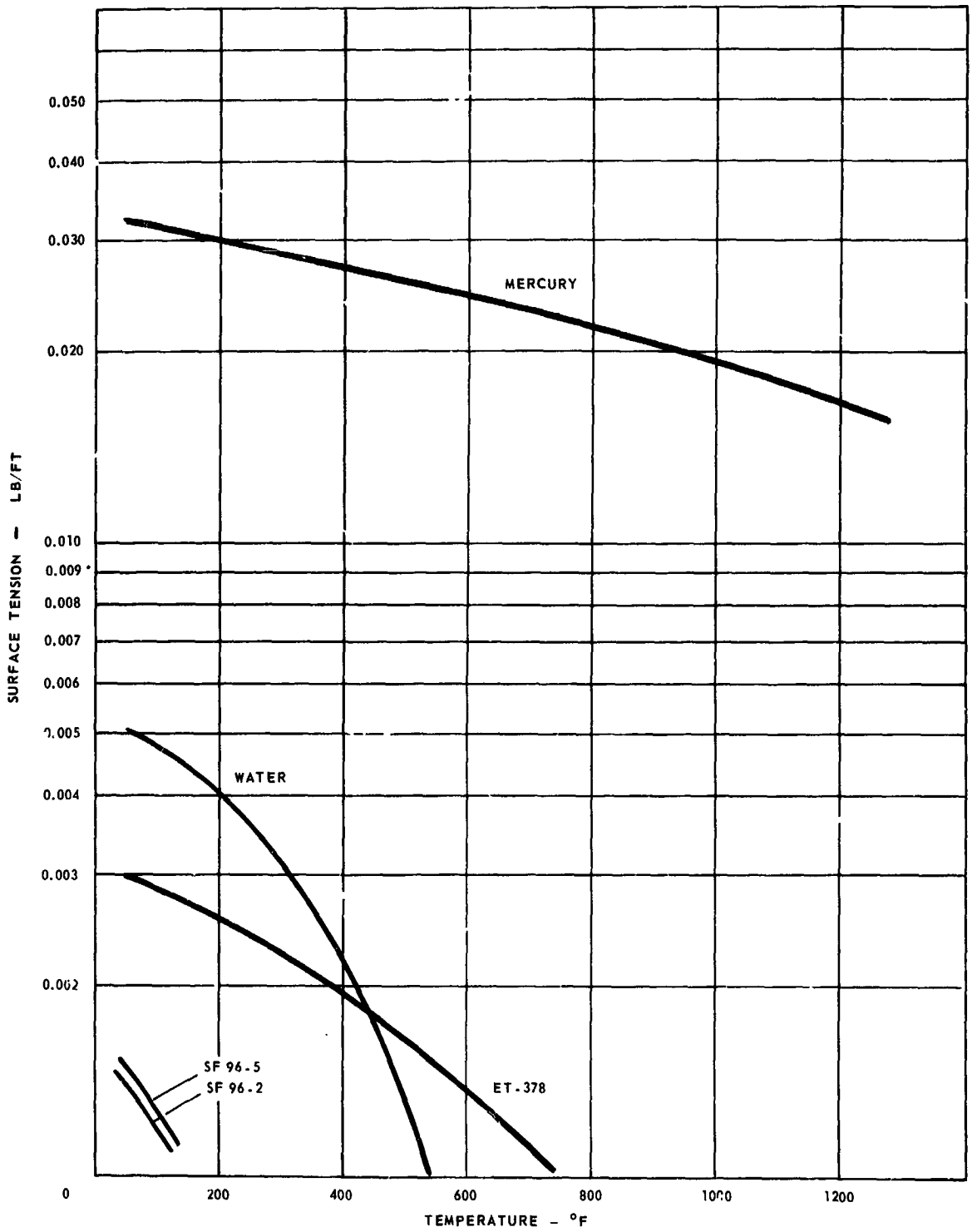

Surface Tension of Test Fluids in Contact With Air

Figure 15

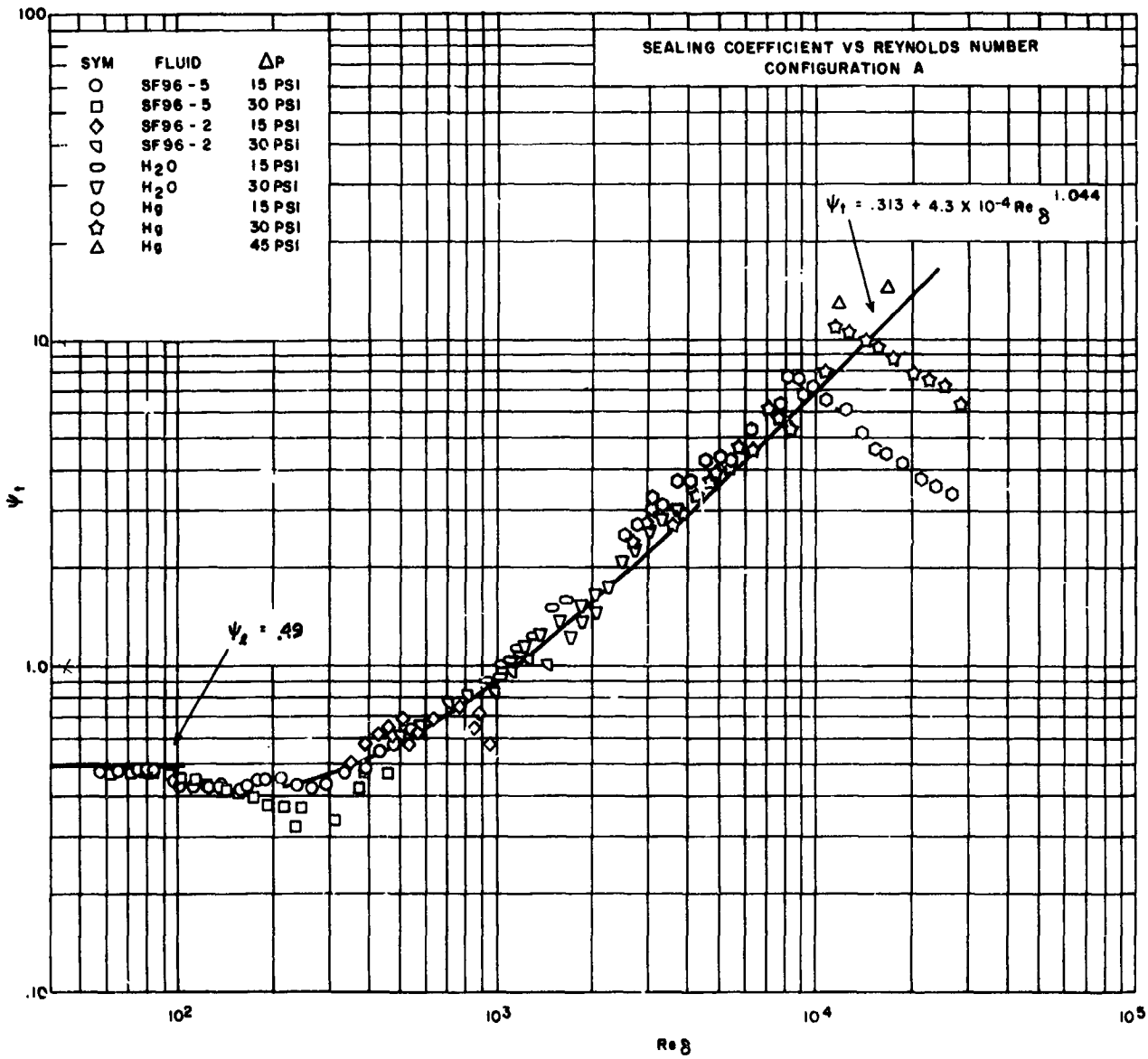

Sealing Coefficient vs Reynolds Number, Configuration A

Figure 16

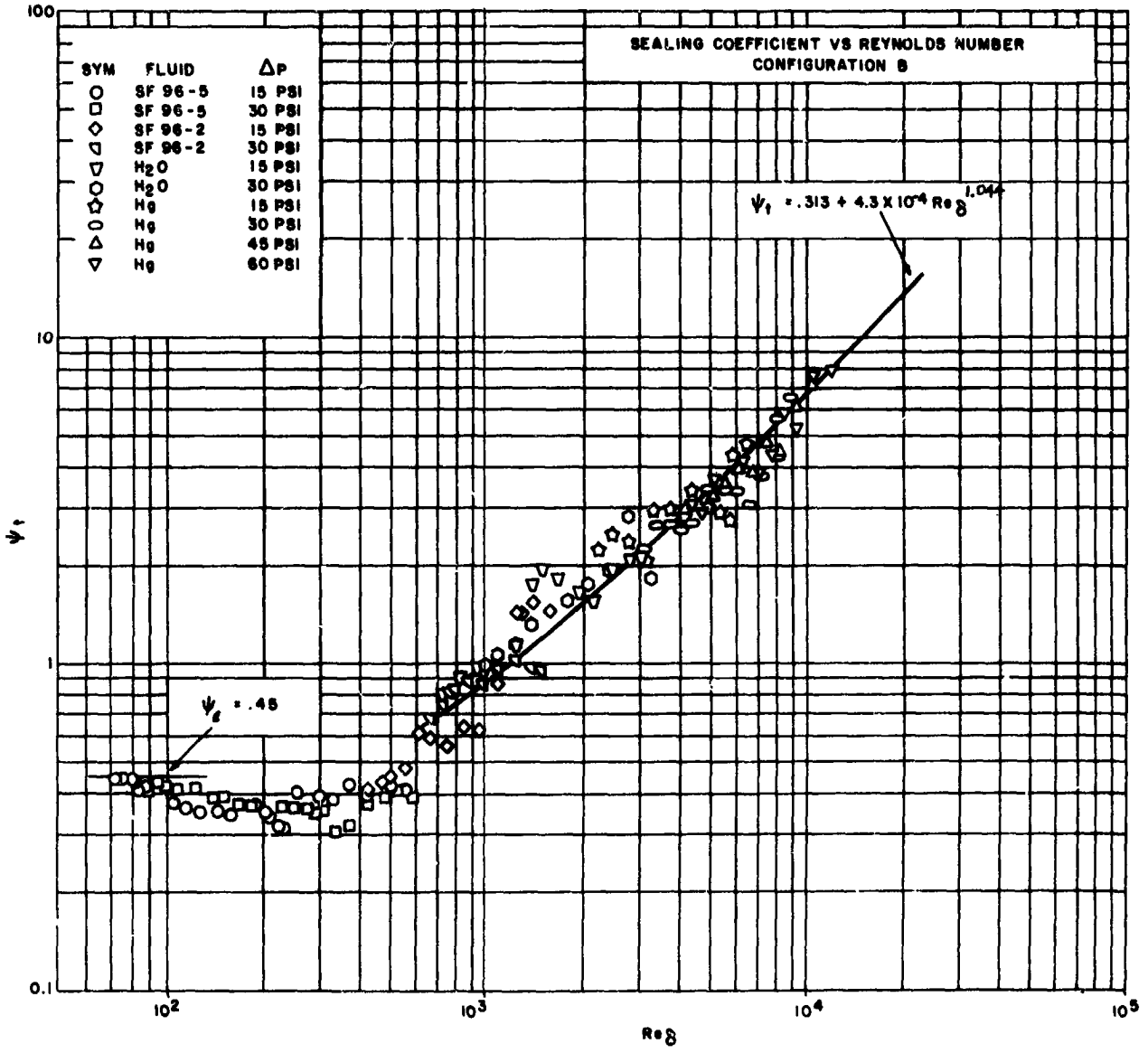

Sealing Coefficient vs Reynolds Number, Configuration B

Figure 17

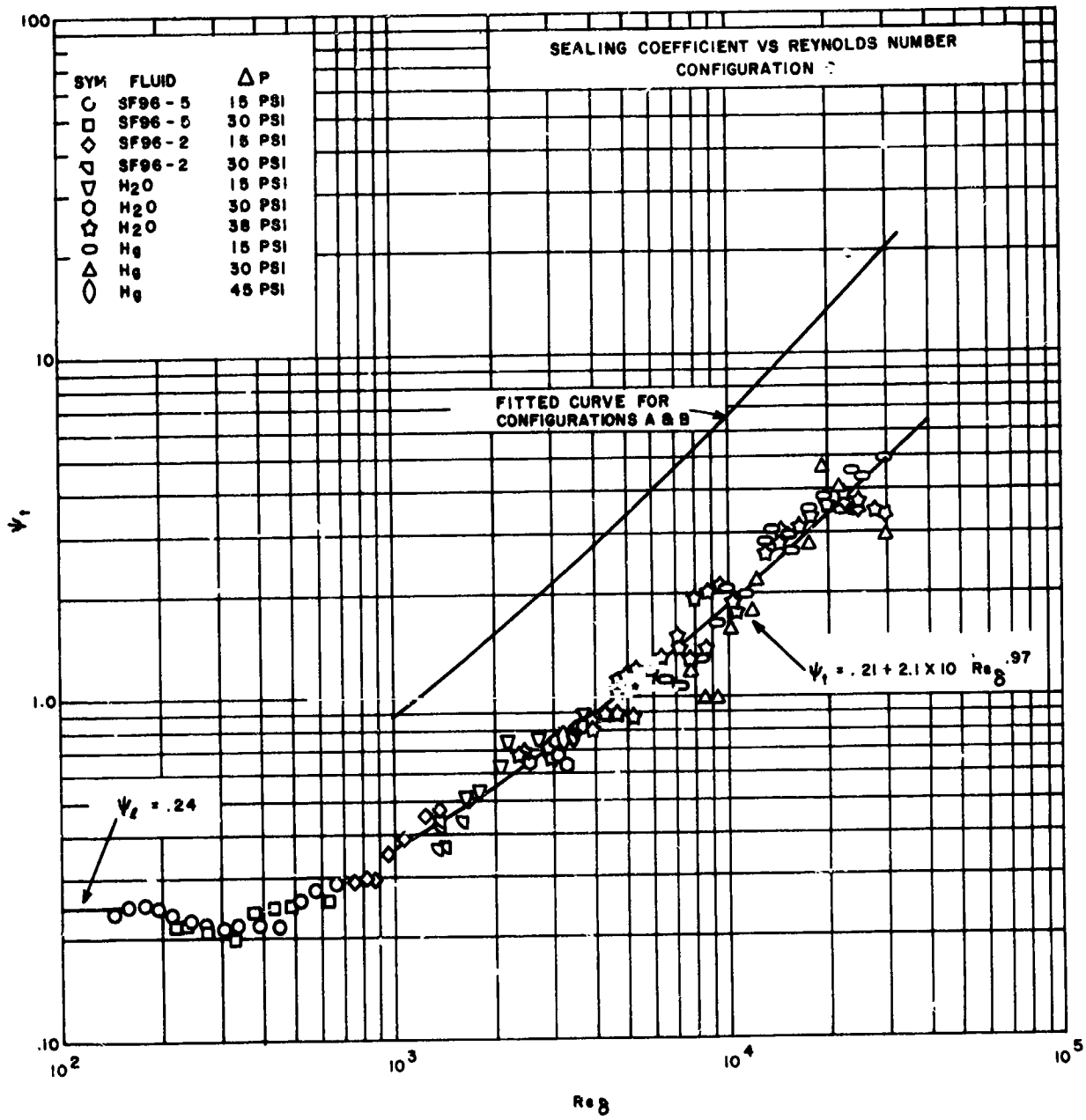

Sealing Coefficient vs Reynolds Number, Configuration C

Figure 18

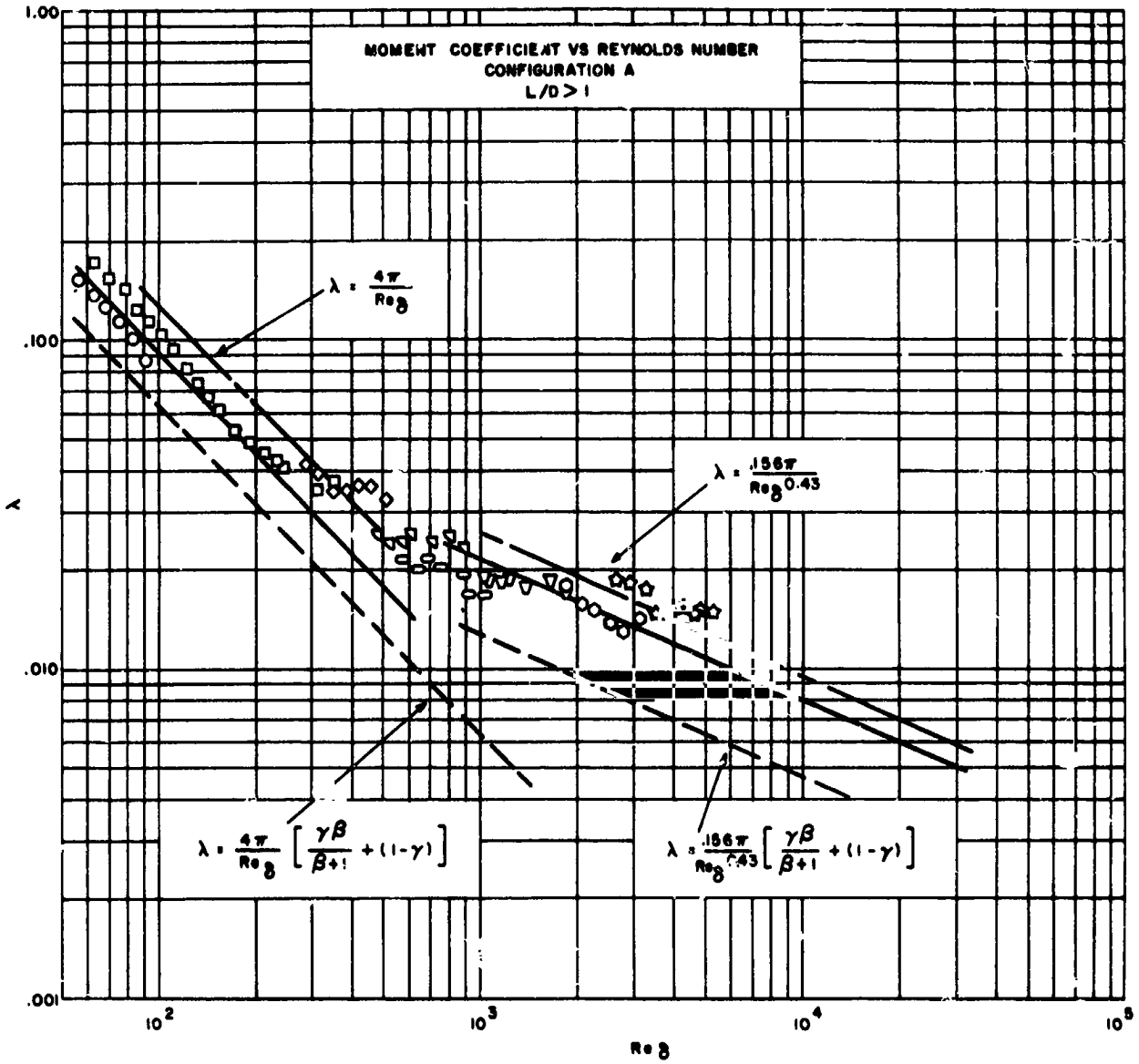

Moment Coefficient vs Reynolds Number, Configuration A

Figure 19

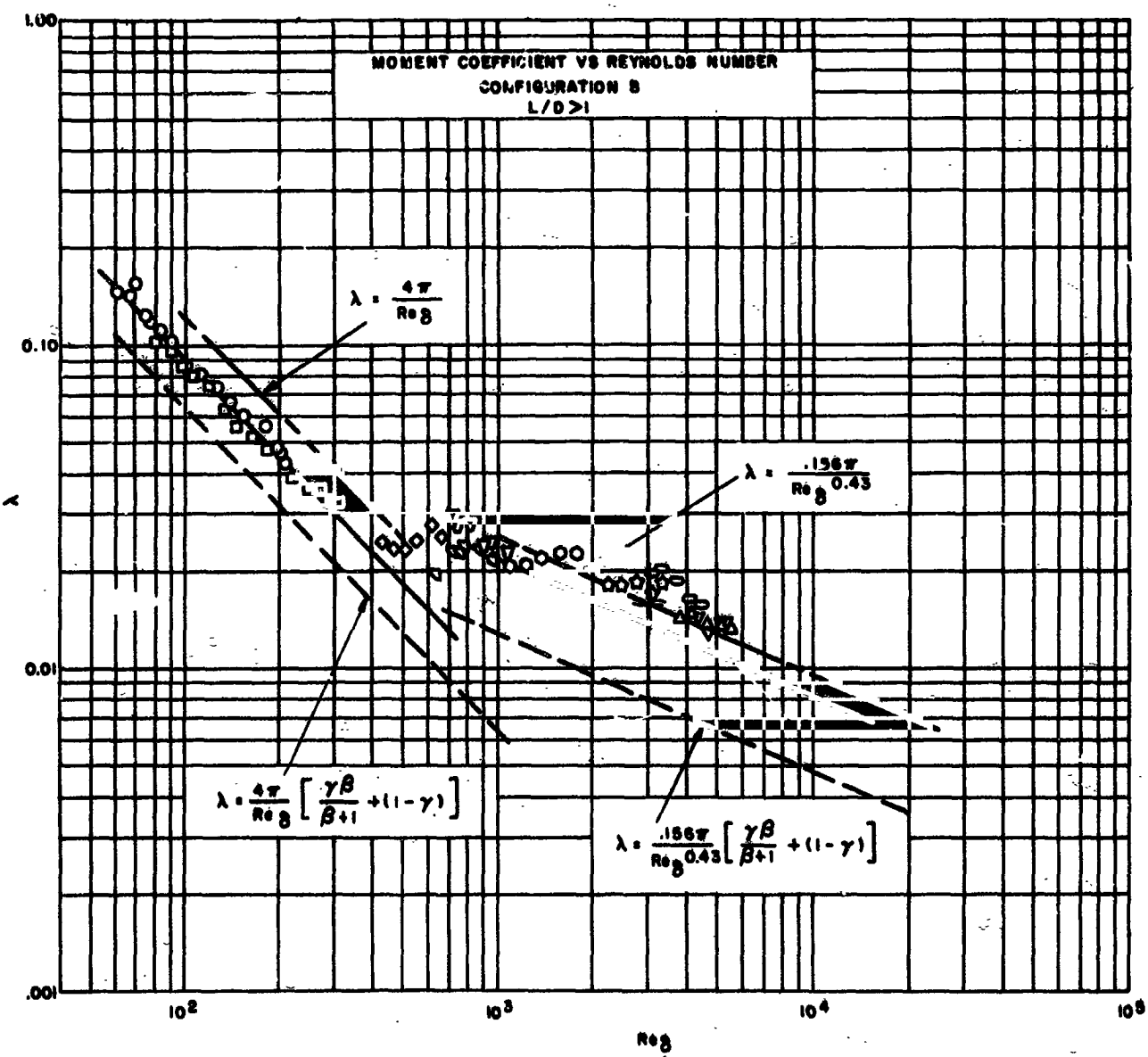

Moment Coefficient vs Reynolds Number, Configuration B

Figure 20

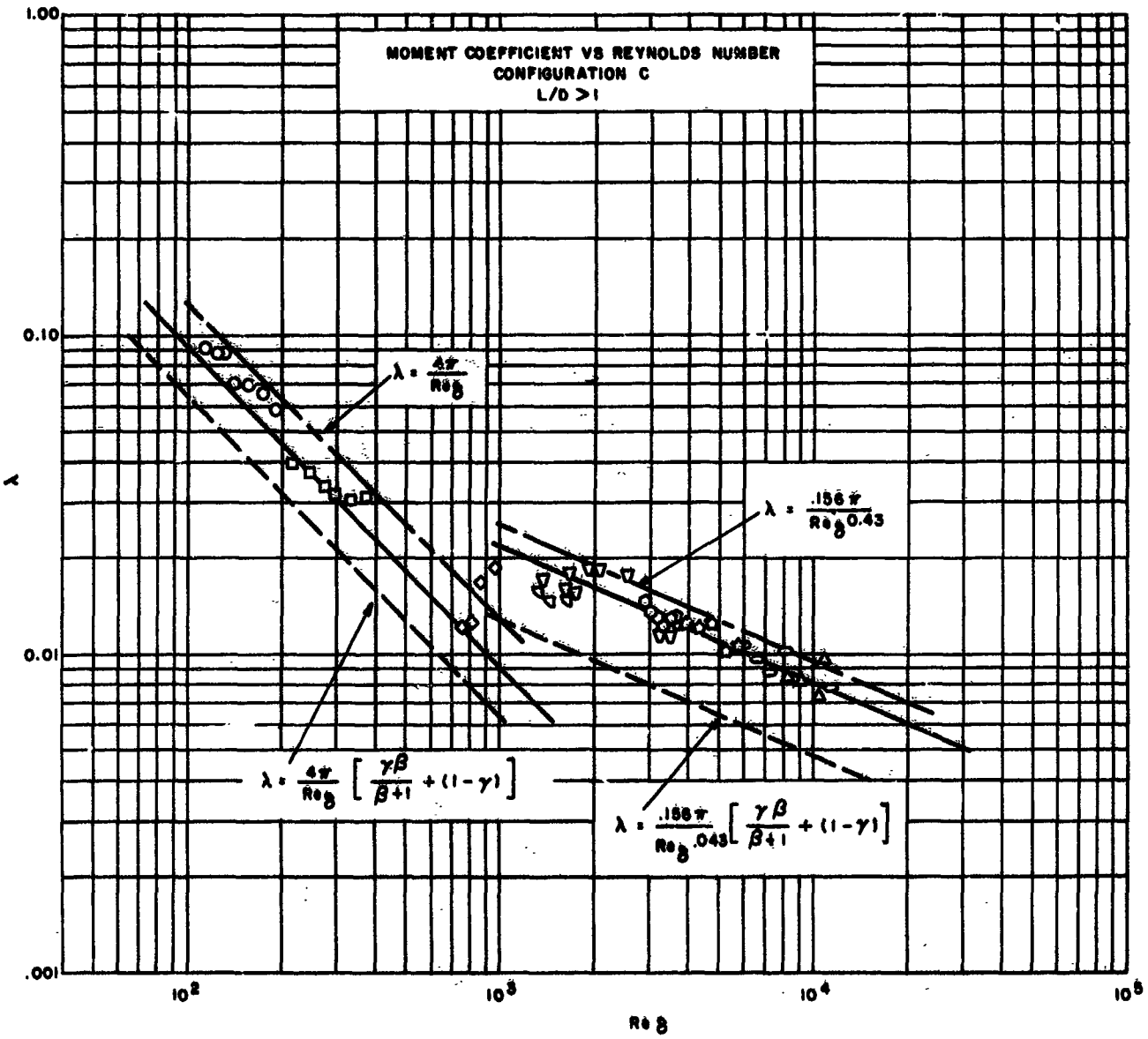

Moment Coefficient vs Reynolds Number, Configuration C

Figure 21

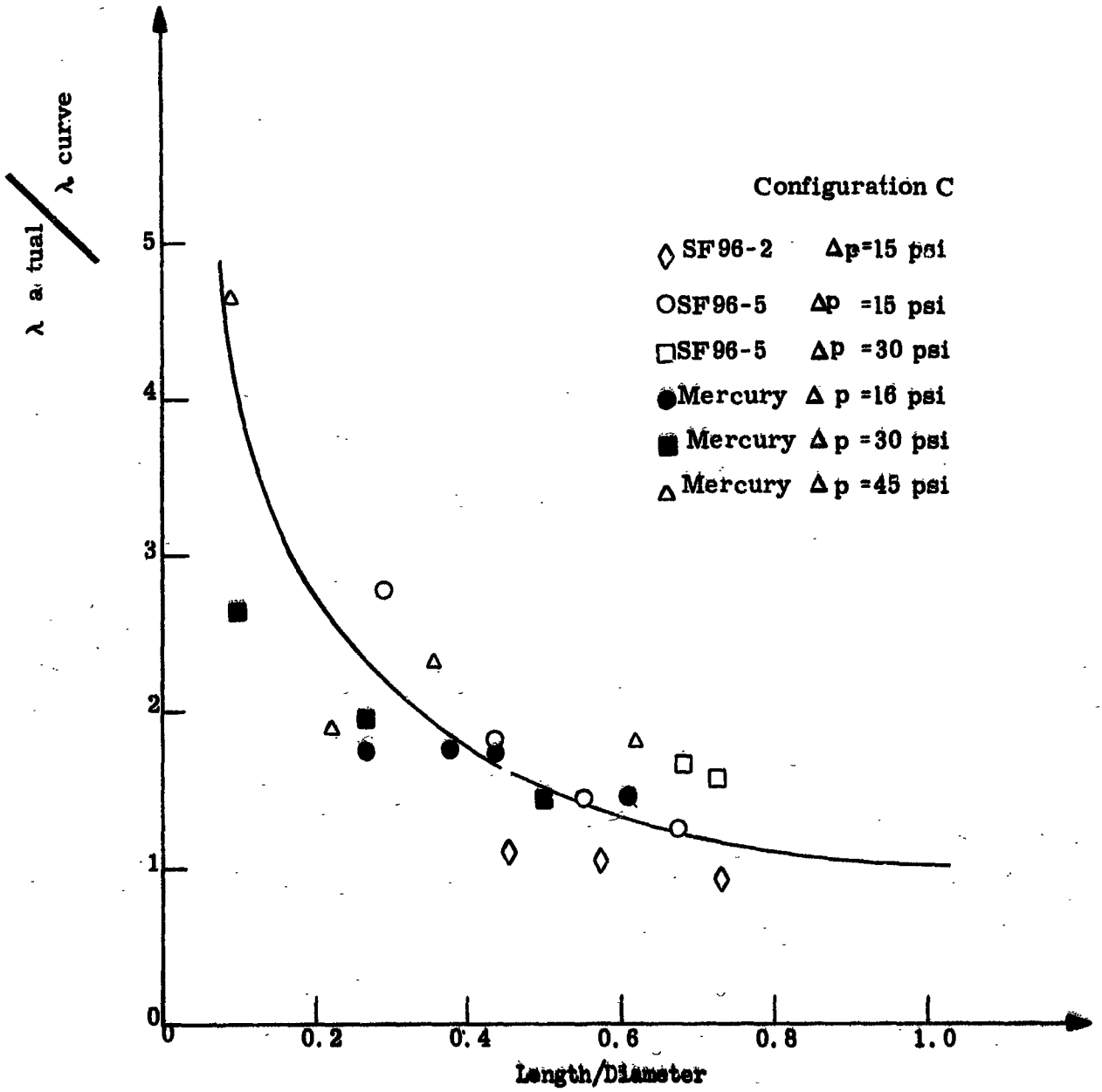

Ratio of Actual Moment Coefficient
to Extrapolated Coefficient for L/D > 1

Figure 22

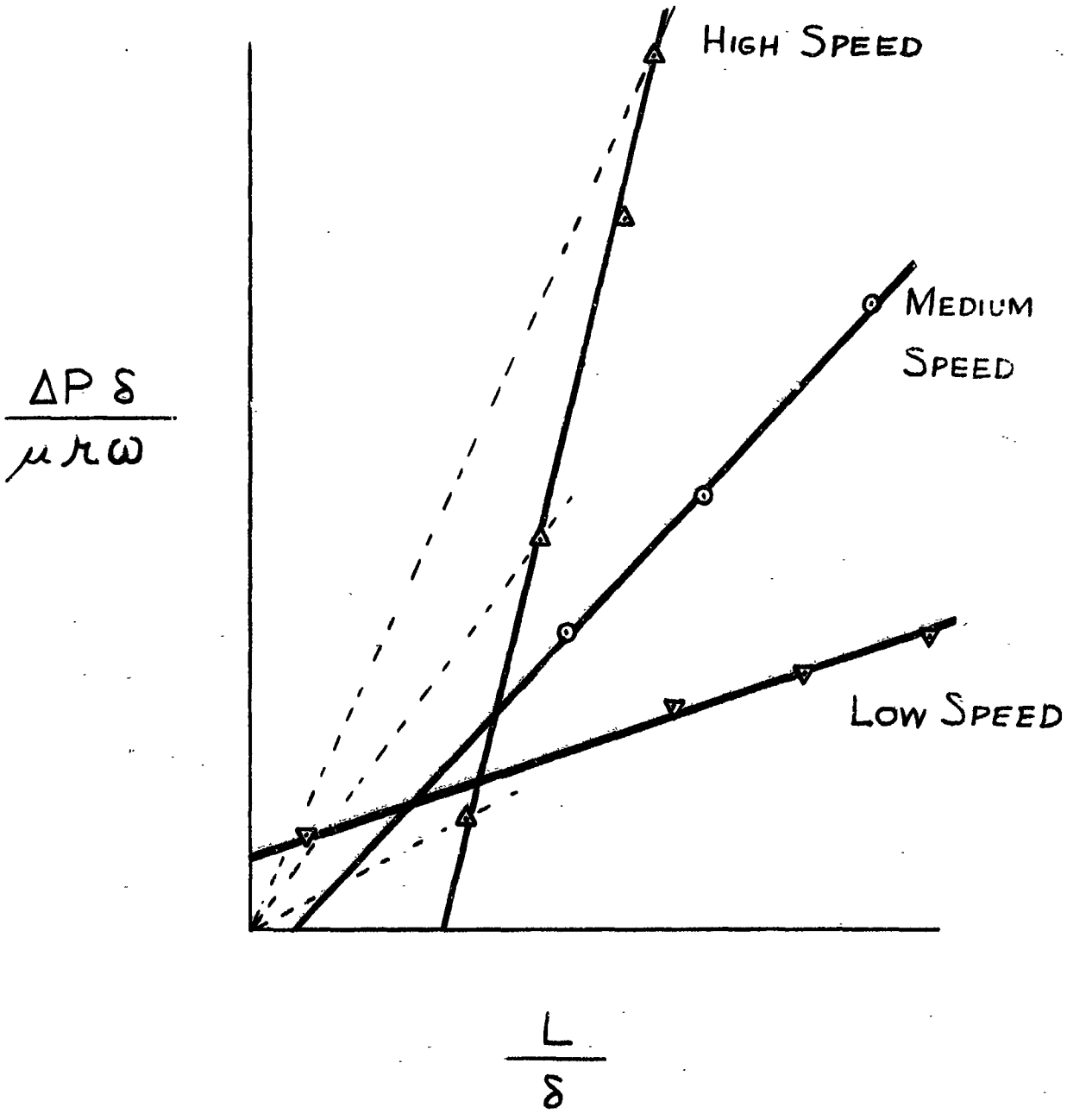

General Nature of the Edge Effect

Figure 23

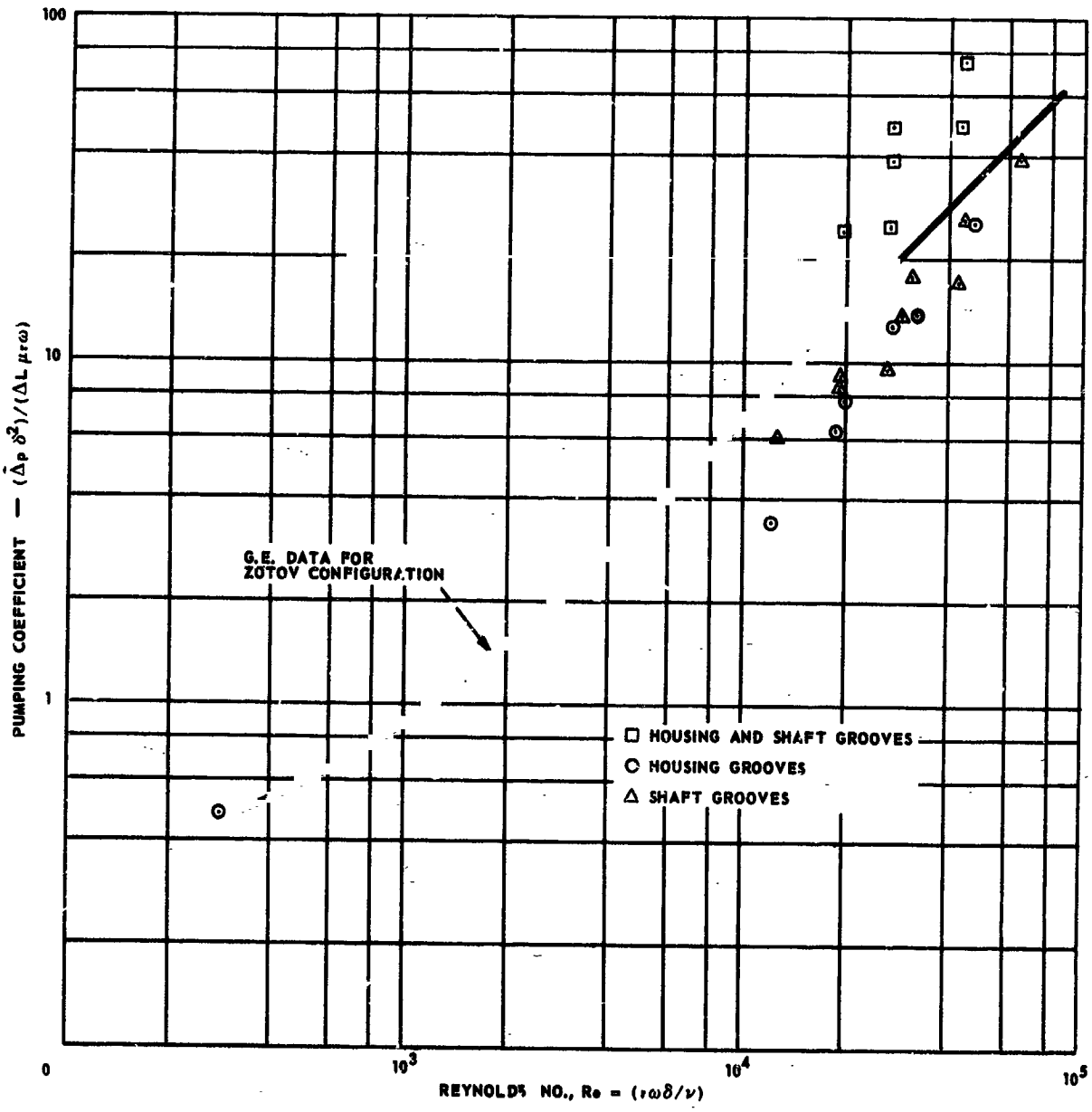

Pumping Coefficients from AGC Visco Pump Tests

Figure 24

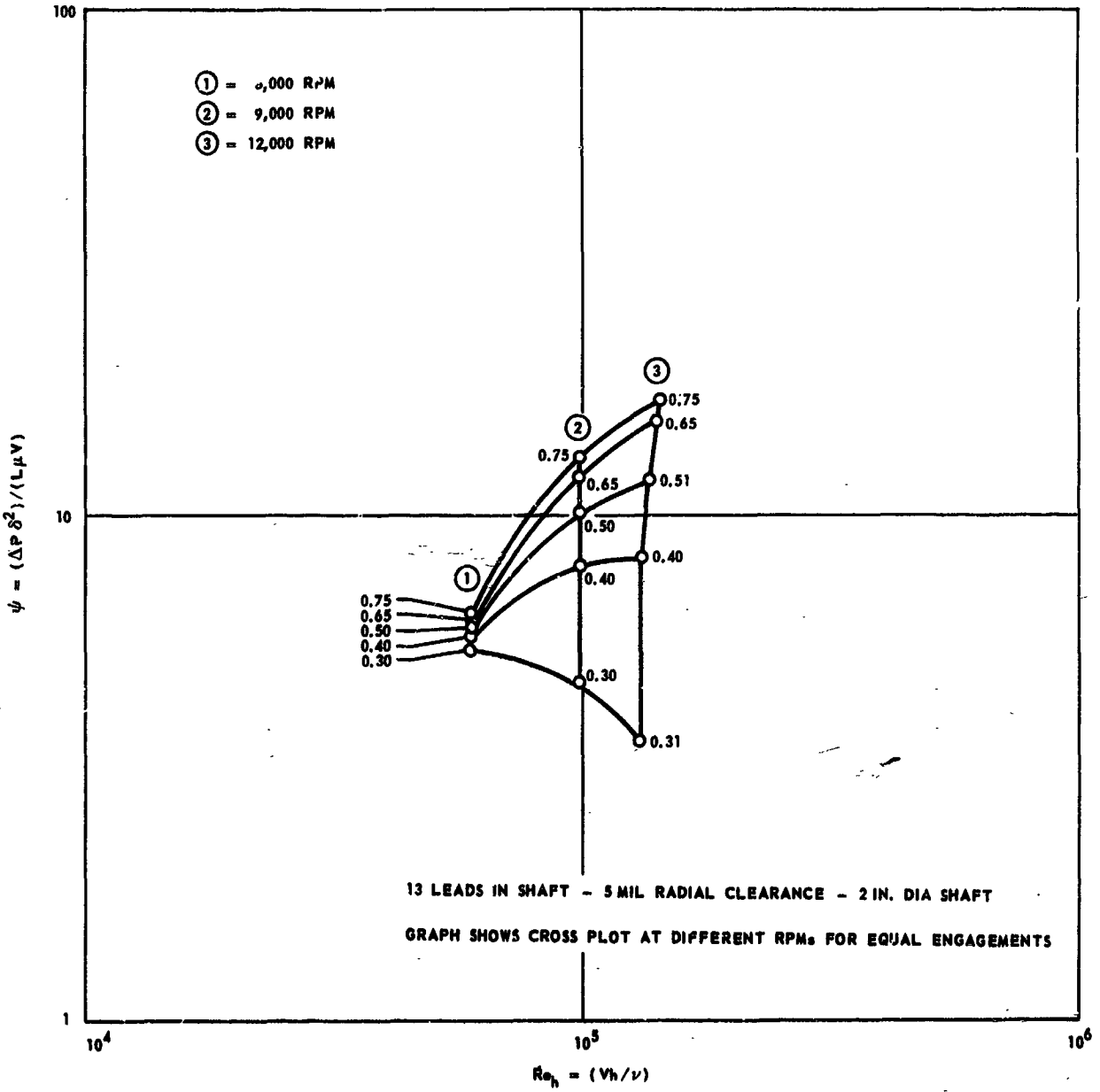

Pumping Coefficient - Shaft Grooves

Figure 25

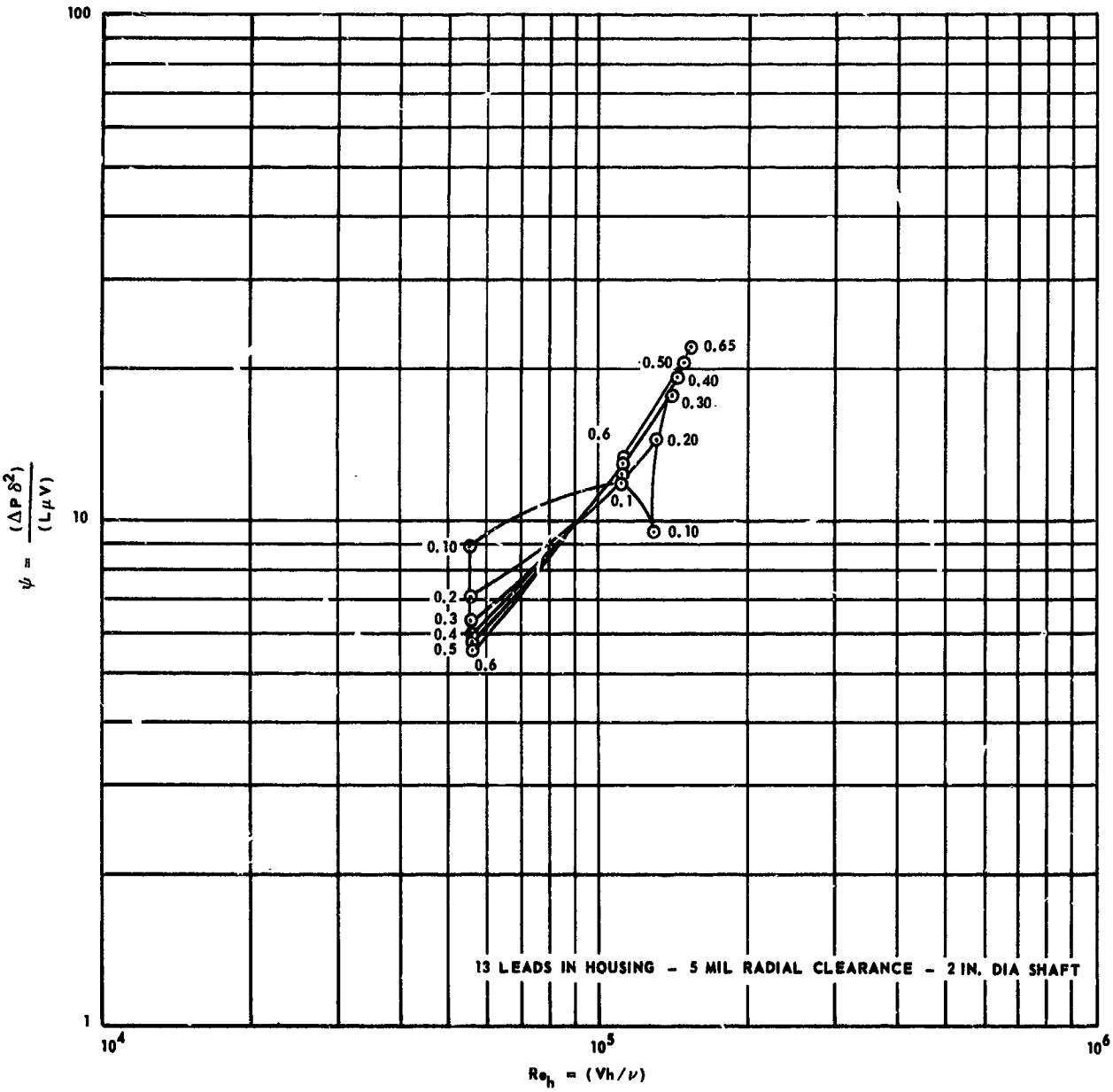

Pumping Coefficient - Housing Grooves

Figure 26

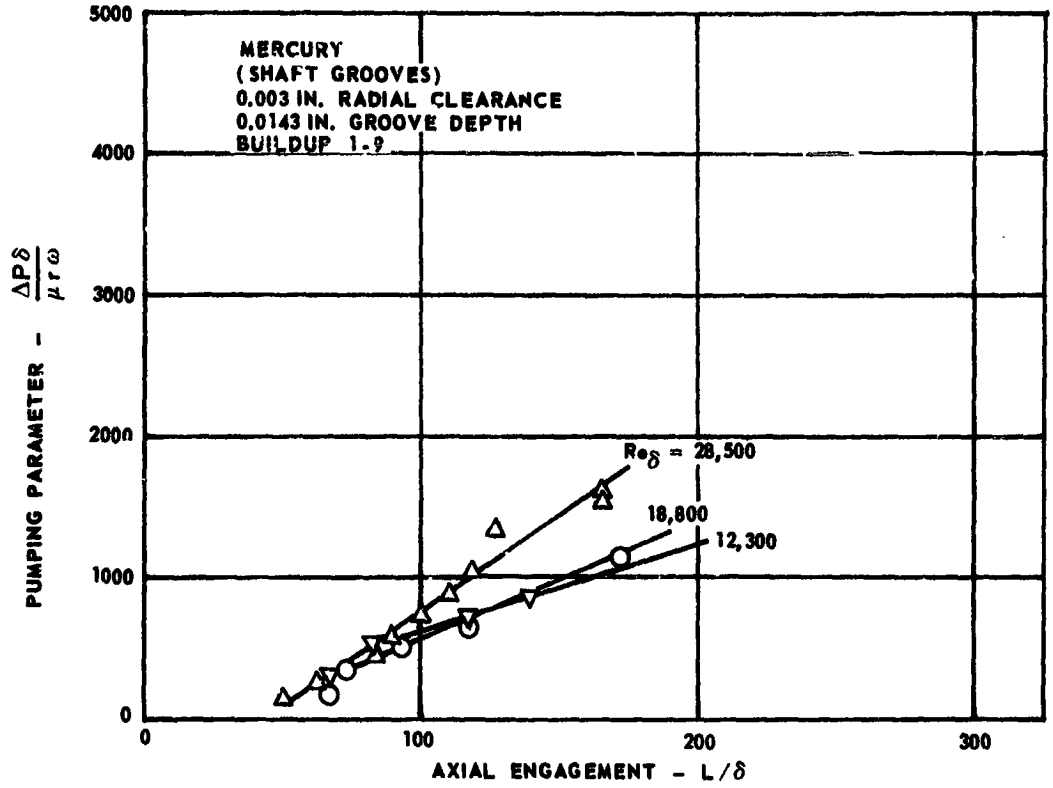

Visco Pump Pressure Characteristic (Buildup 1-9)
Mercury - Configuration 6

Figure 27

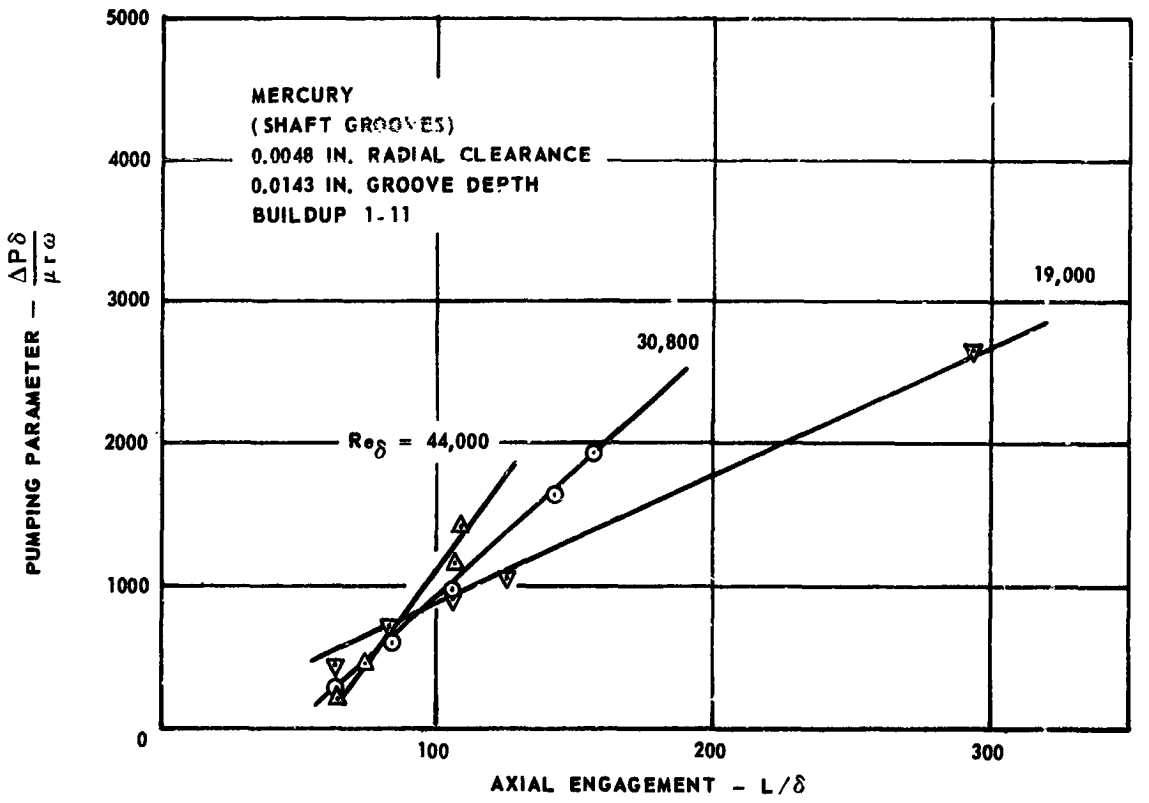

Visco Pump Pressure Characteristic (Buildup 1-11)
Mercury - Configuration 8

Figure 28

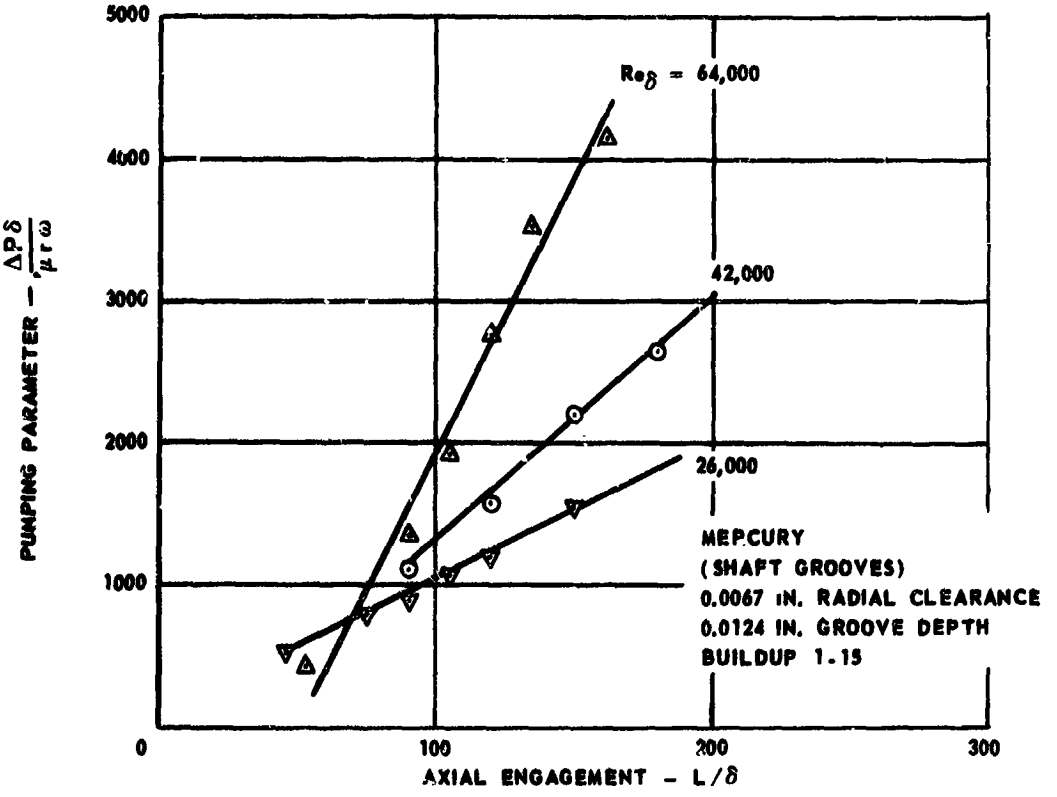

Visco Pump Pressure Characteristic (Buildup 1-15)
Mercury - Configuration 12

Figure 29

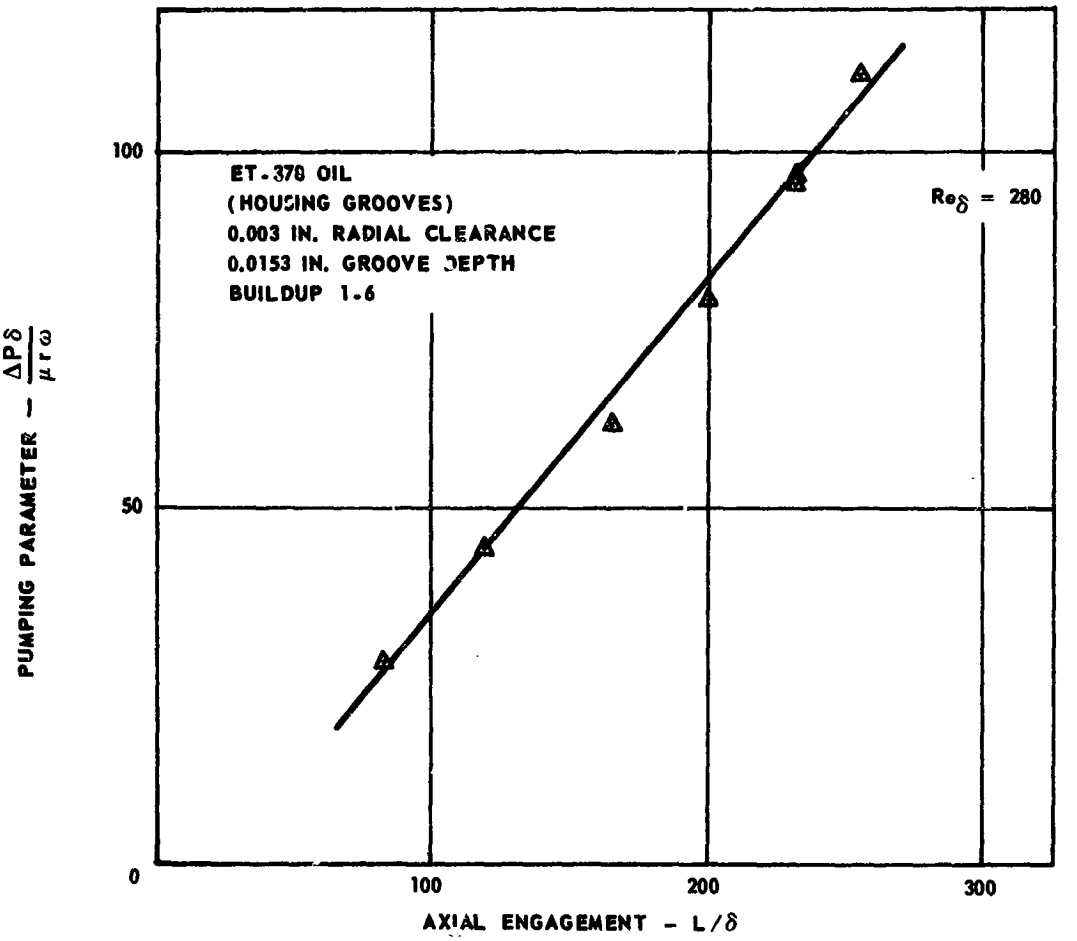

Visco Pump Pressure Characteristic (Buildup 1-6)
ET-378 Oil - Configuration 5

Figure 30

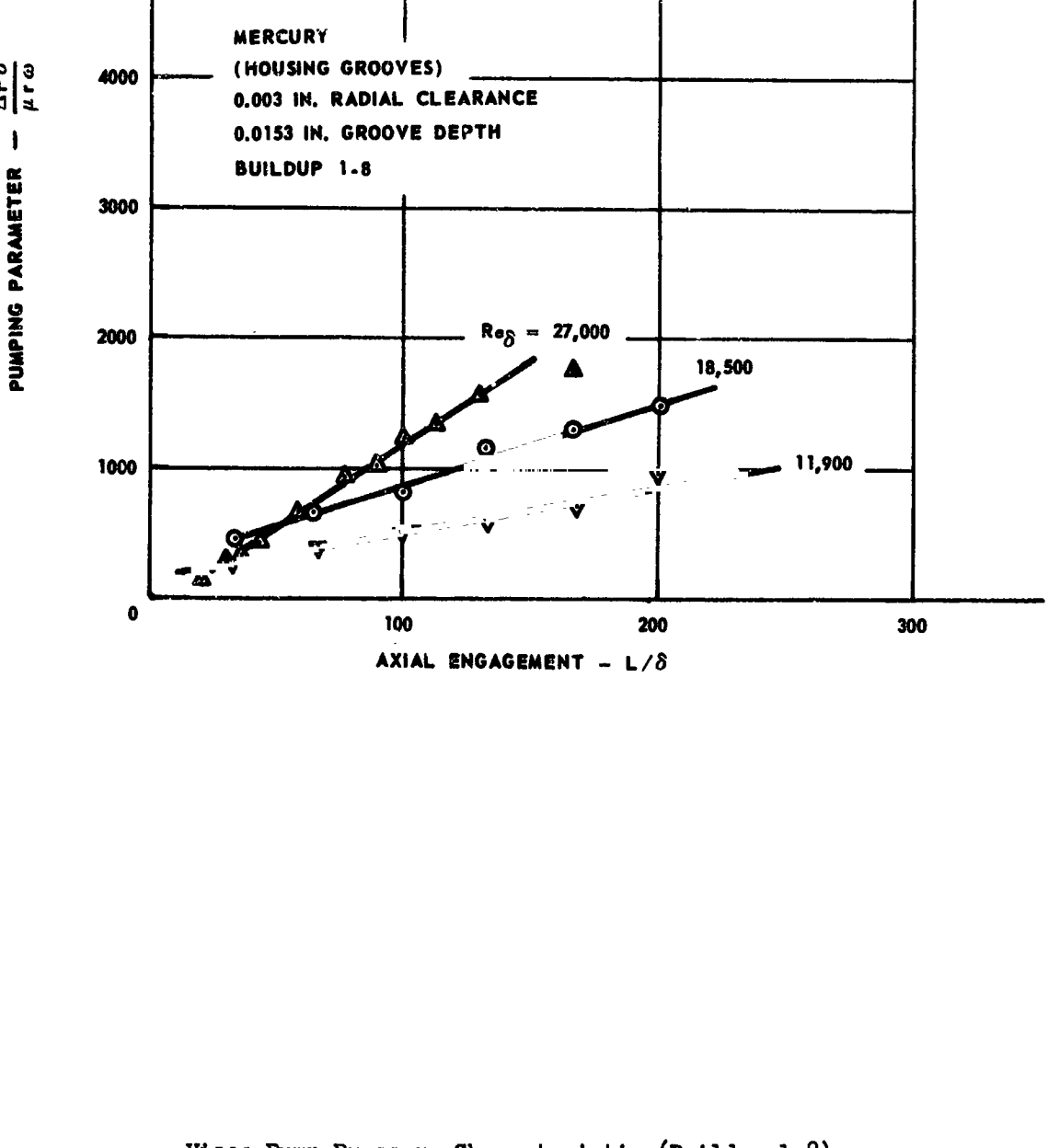

Visco Pump Pressure Characteristic (Buildup 1-8)
Mercury - Configuration 5

Figure 31

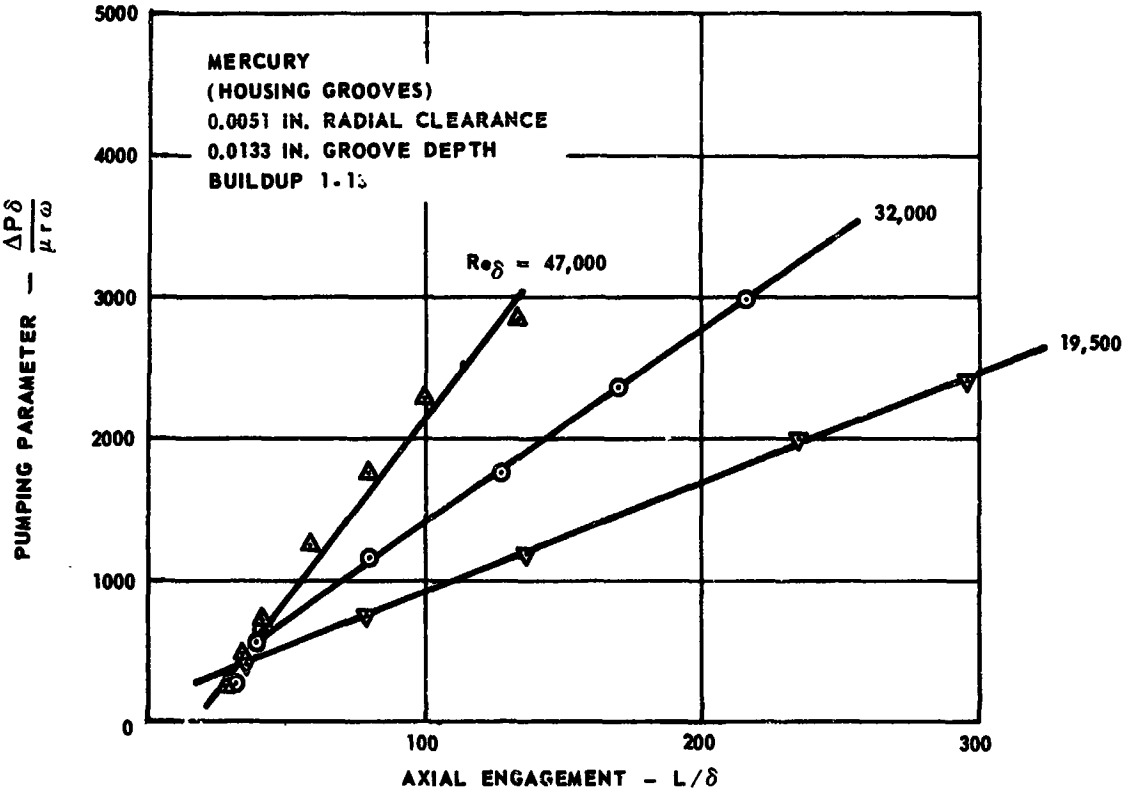

Visco Pump Pressure Characteristic (Buildup 1-13)
Mercury - Configuration 10

Figure 32

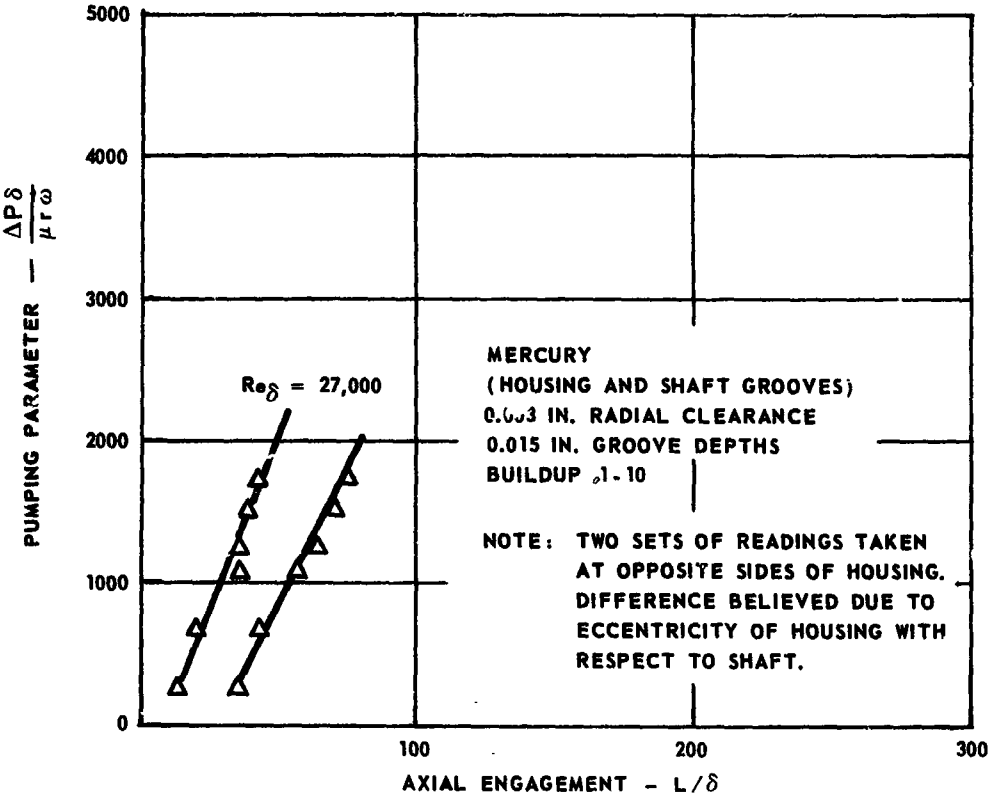

Visco Pump Pressure Characteristic (Buildup 1-10)
Mercury - Configuration 7

Figure 33

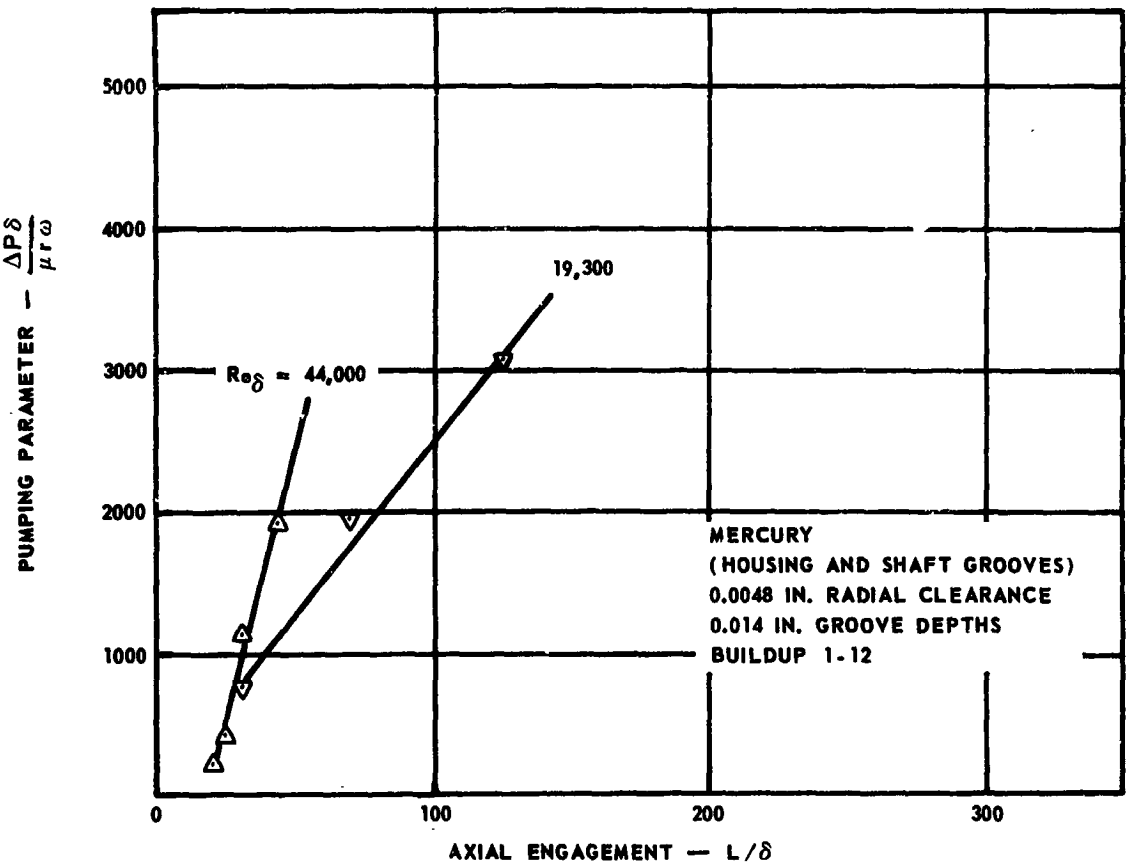

Visco Pump Pressure Characteristic (Buildup 1-12)
Mercury - Configuration 9

Figure 34

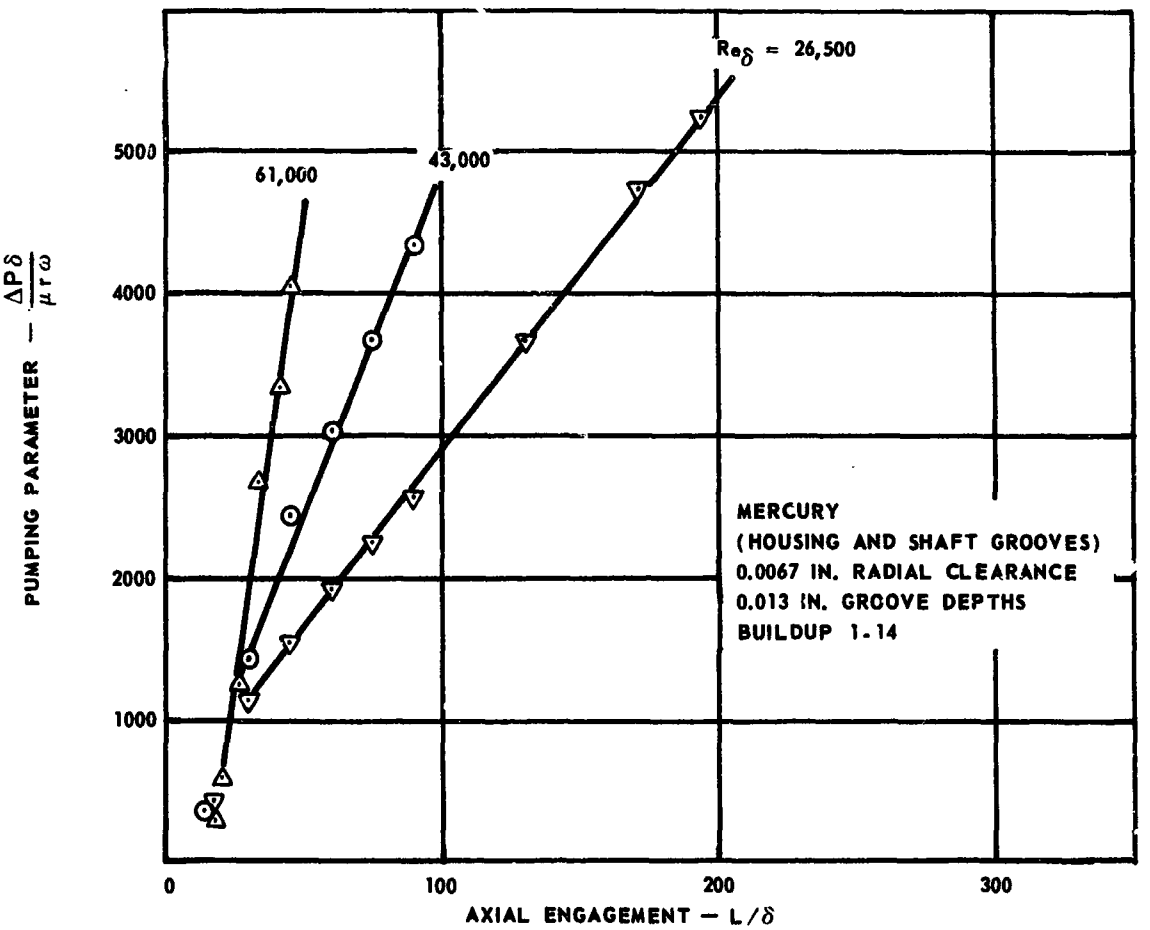

Visco Pump Pressure Characteristic (Buildup 1-14)
Mercury - Configuration 11

Figure 35

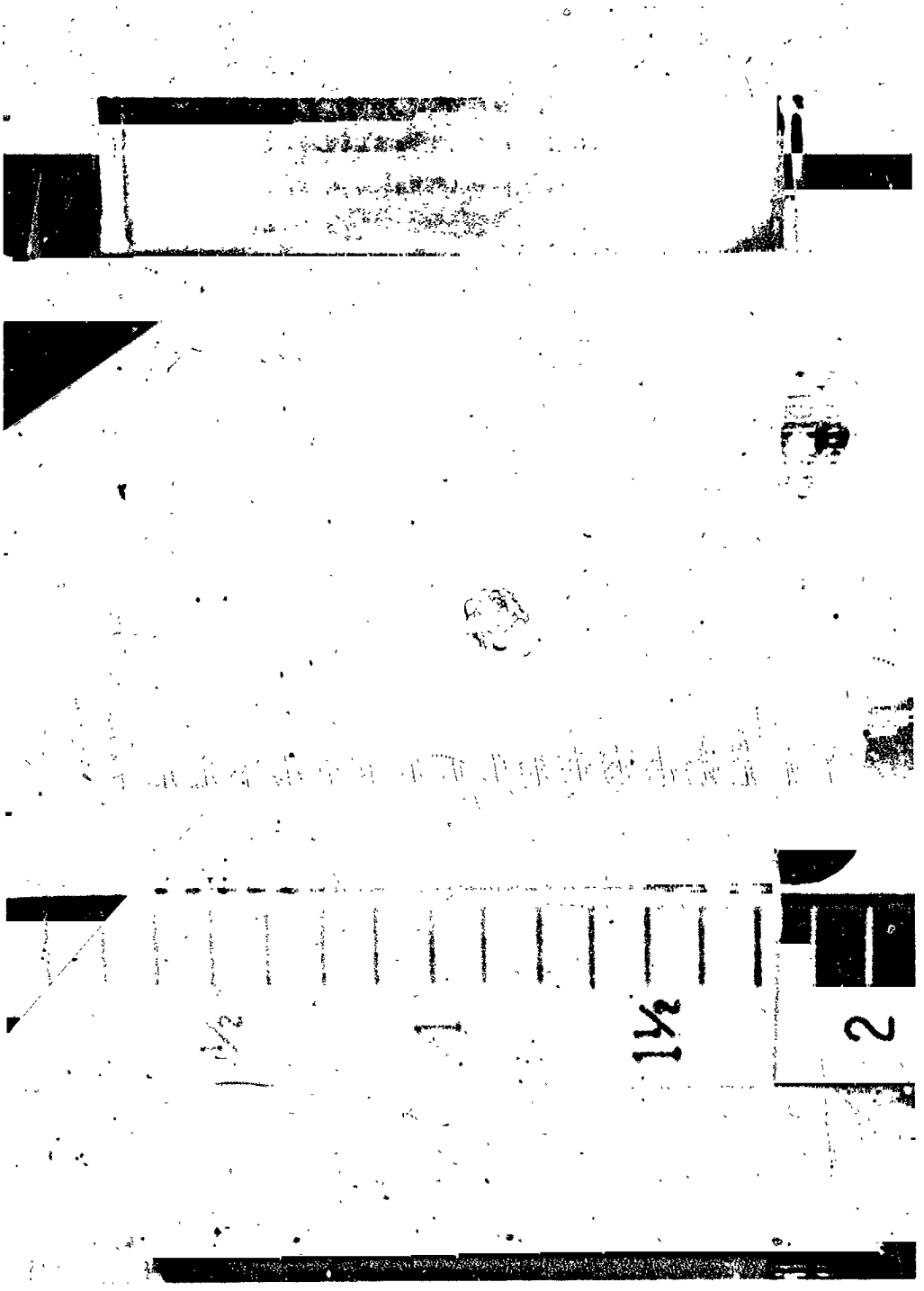

Mercury Interface - Configuration 5
(Housing Grooves, 0.003 in. Radial Clearance;
N = 12,000 rpm; T = 300°F; ΔP = 100 psi)

Figure 36

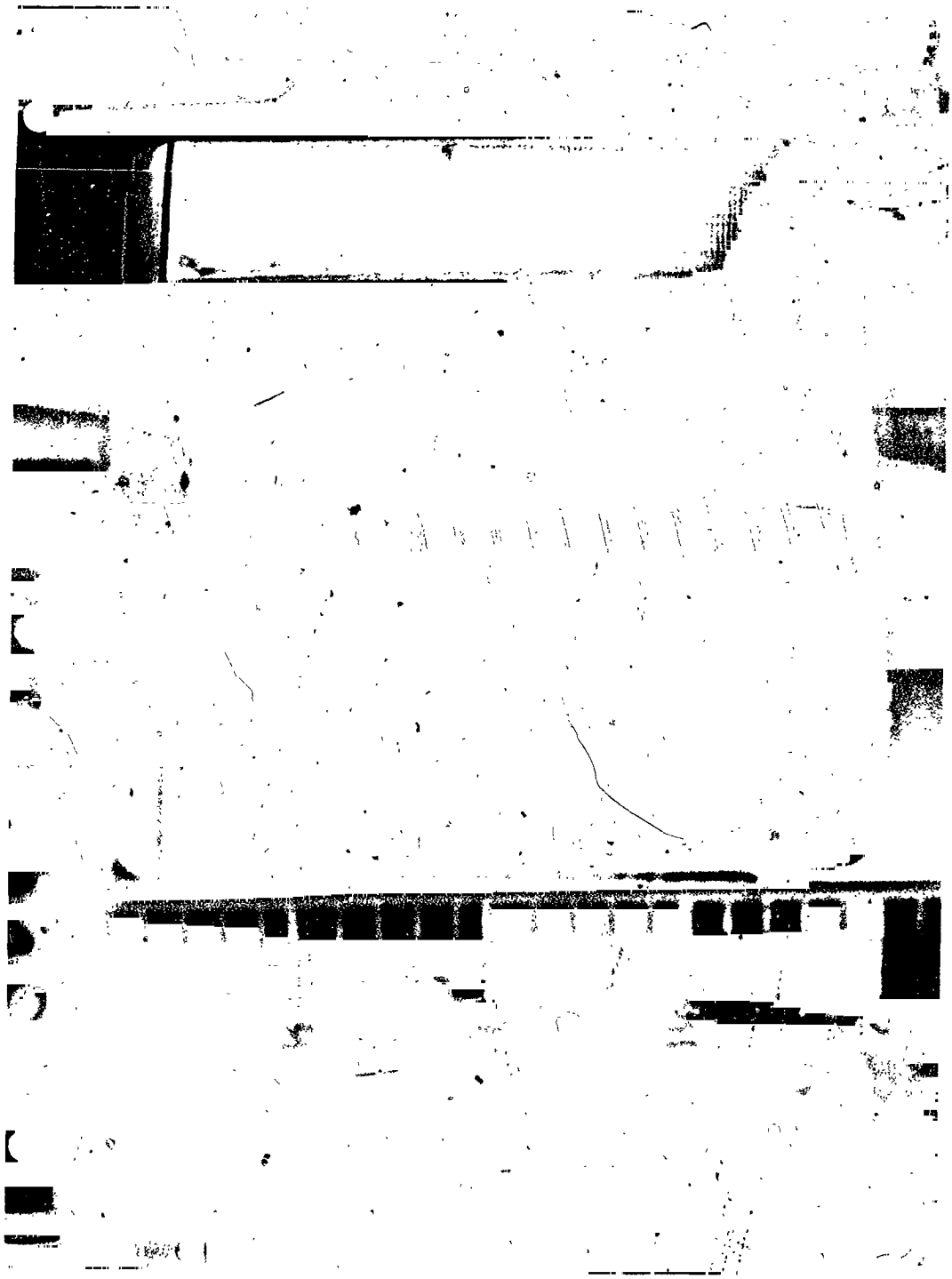

ET-378 Oil Interface - Configuration 5
(Housing Grooves, 0.003 in. Radial Clearance;
N = 12,500 rpm; T = 225°F; ΔP = 61.5 psi)

Figure 37

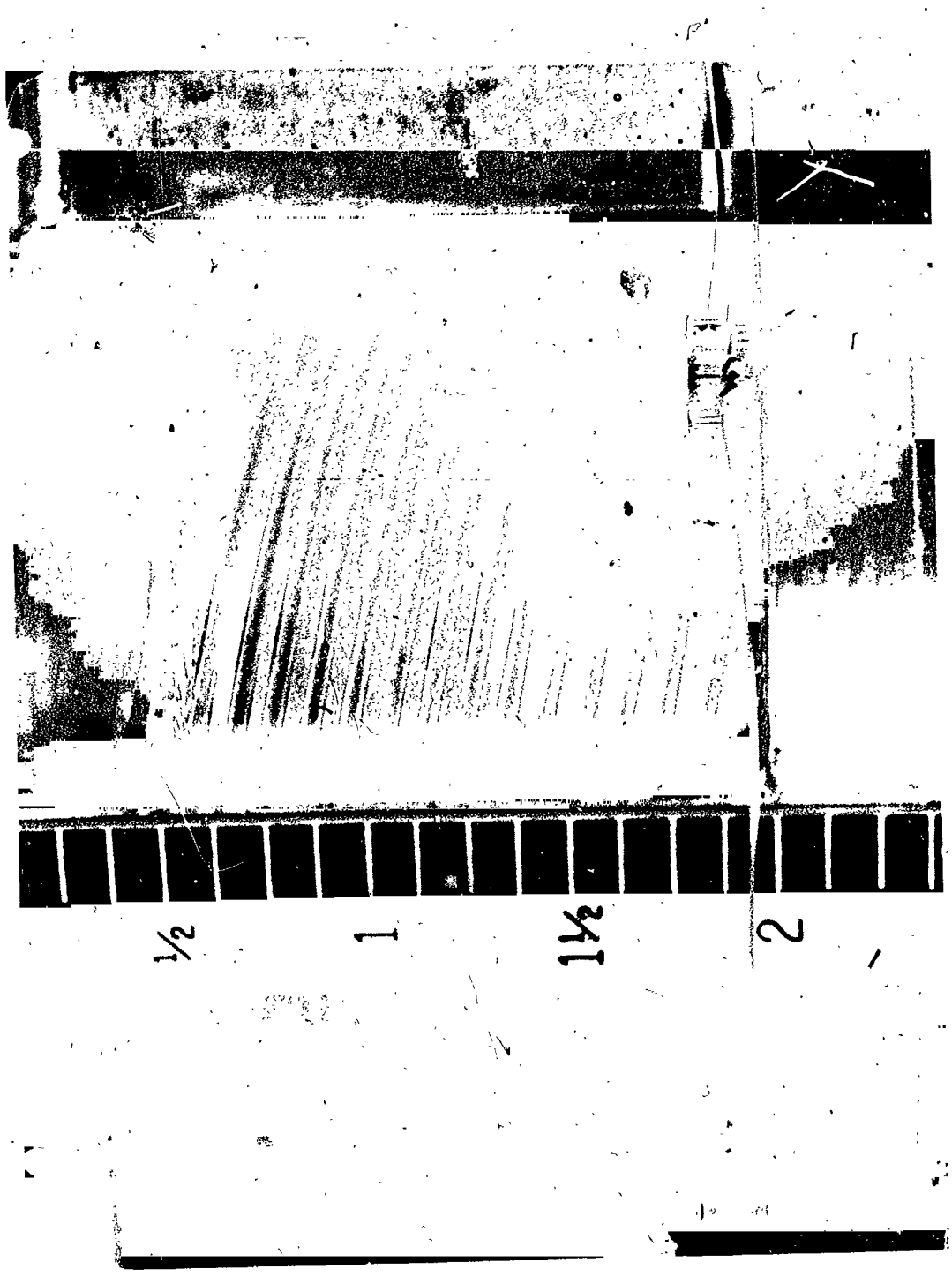

Mercury Interface - Configuration 6
(Shaft Grooves, 0.003 in. Radial Clearance;
N = 12,000 rpm; T = 287°F; ΔP = 110 psi)

Figure 38

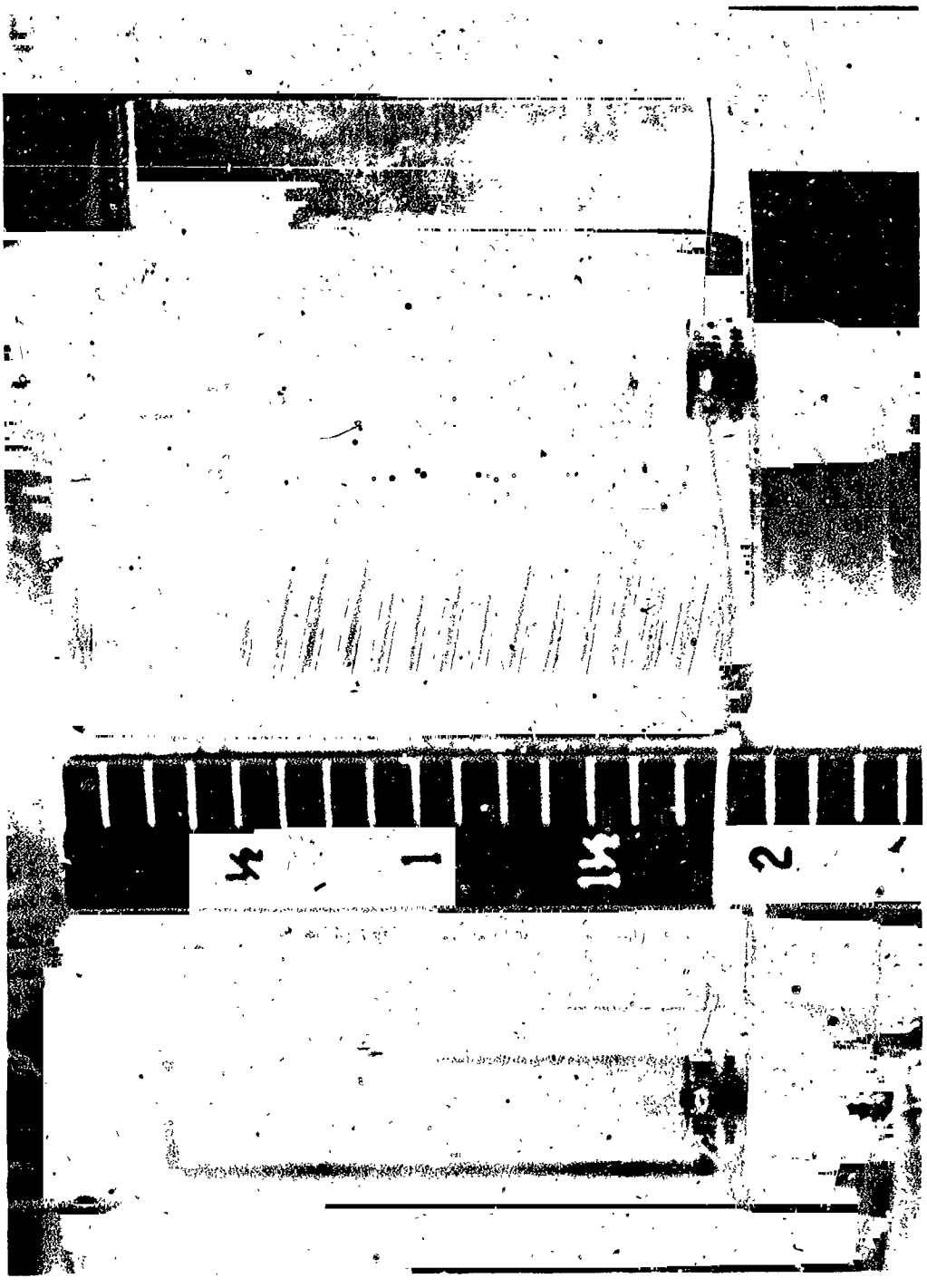

Mercury Interface - Configuration 8
(Shaft Grooves, 0.0048 in. Radial Clearance;
N = 12,000 rpm; T = 250°F; ΔP = 40 psi)

Figure 39

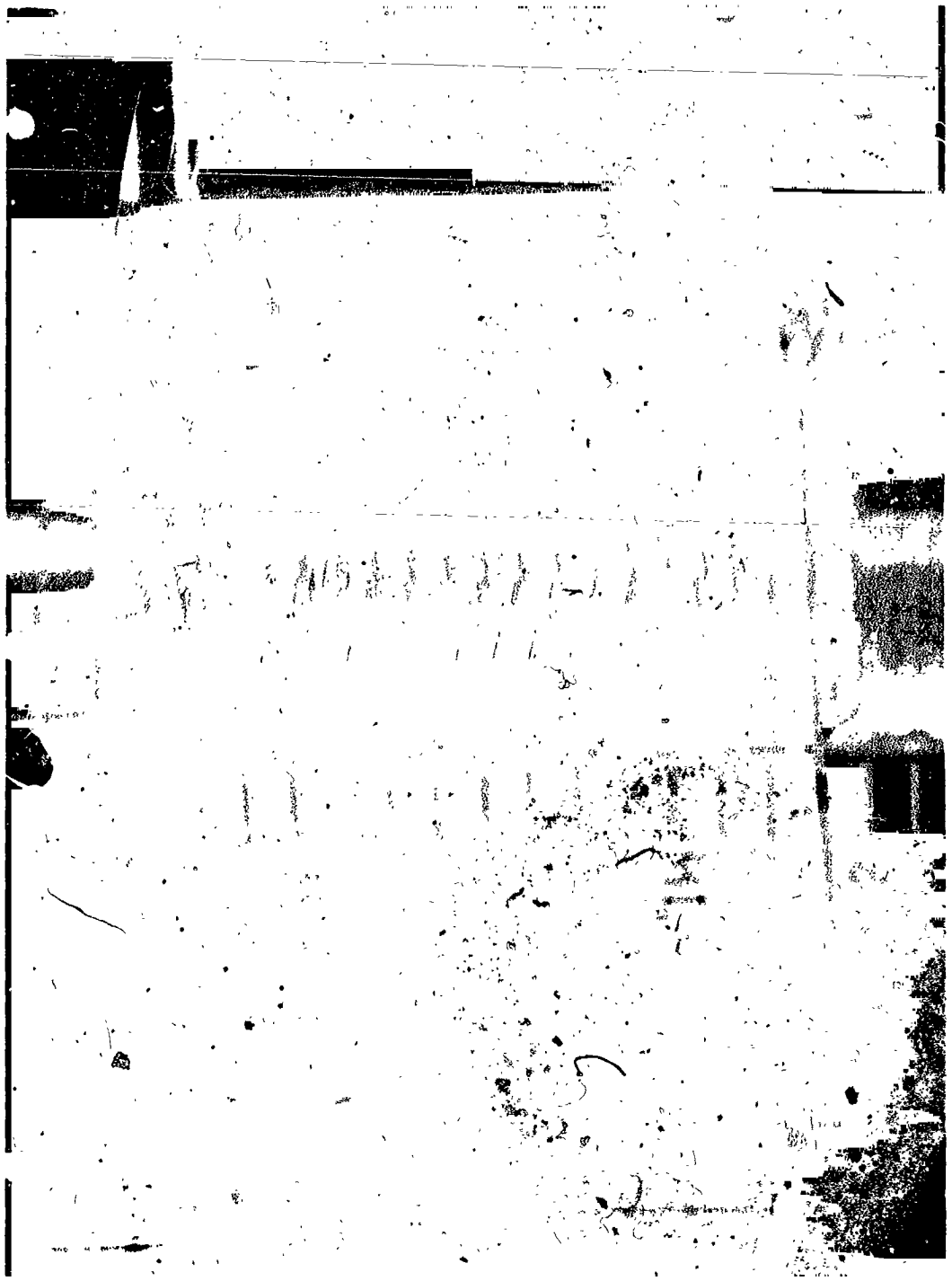

Mercury Interface - Configuration 9
(Housing and Shaft Grooves, 0.0048 in. Radial Clearance;
N = 12,000 rpm; T = 295°F; ΔP = 80 psi)

Figure 40

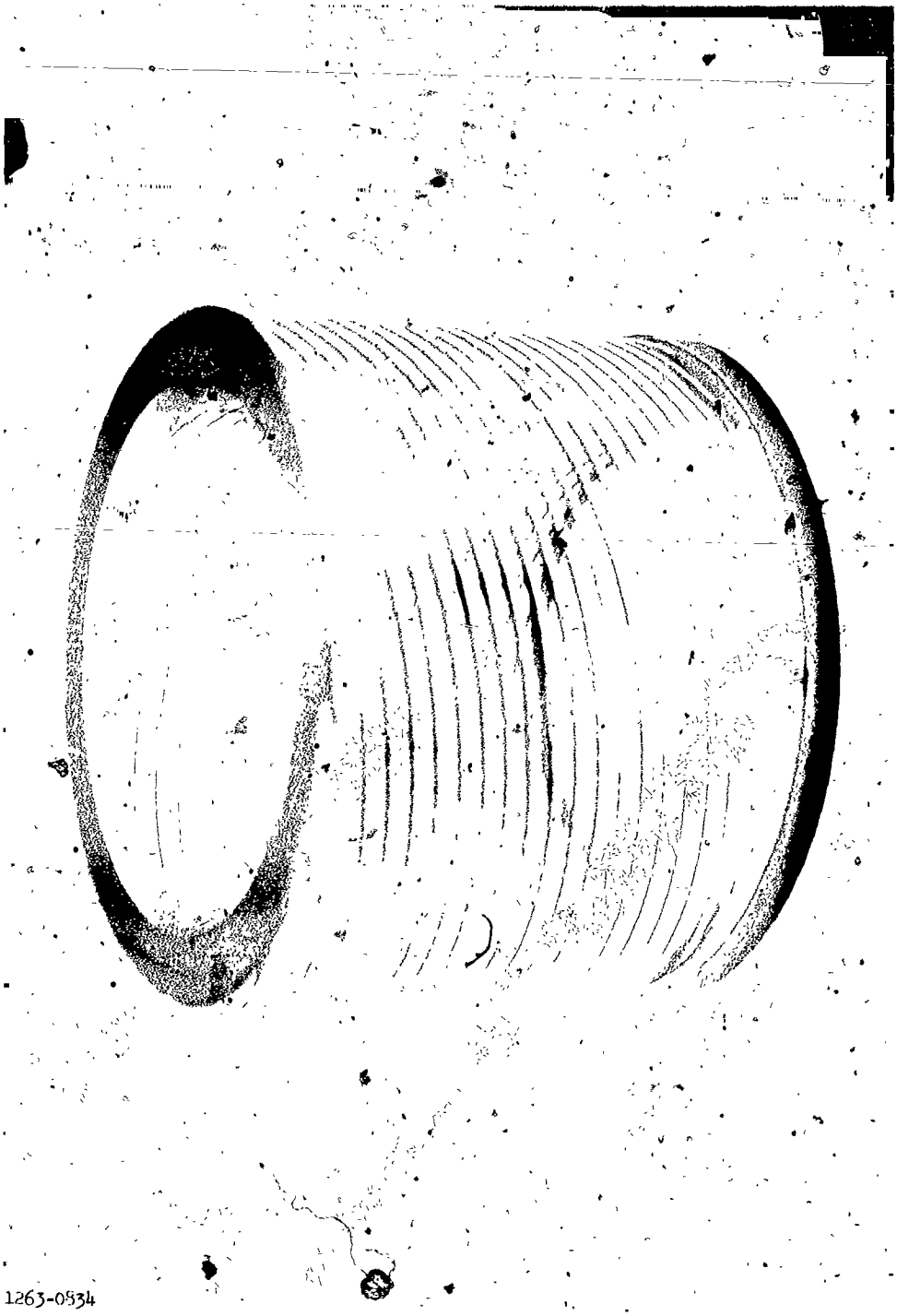

Erosion Damage to Quartz Test Section

Figure 41

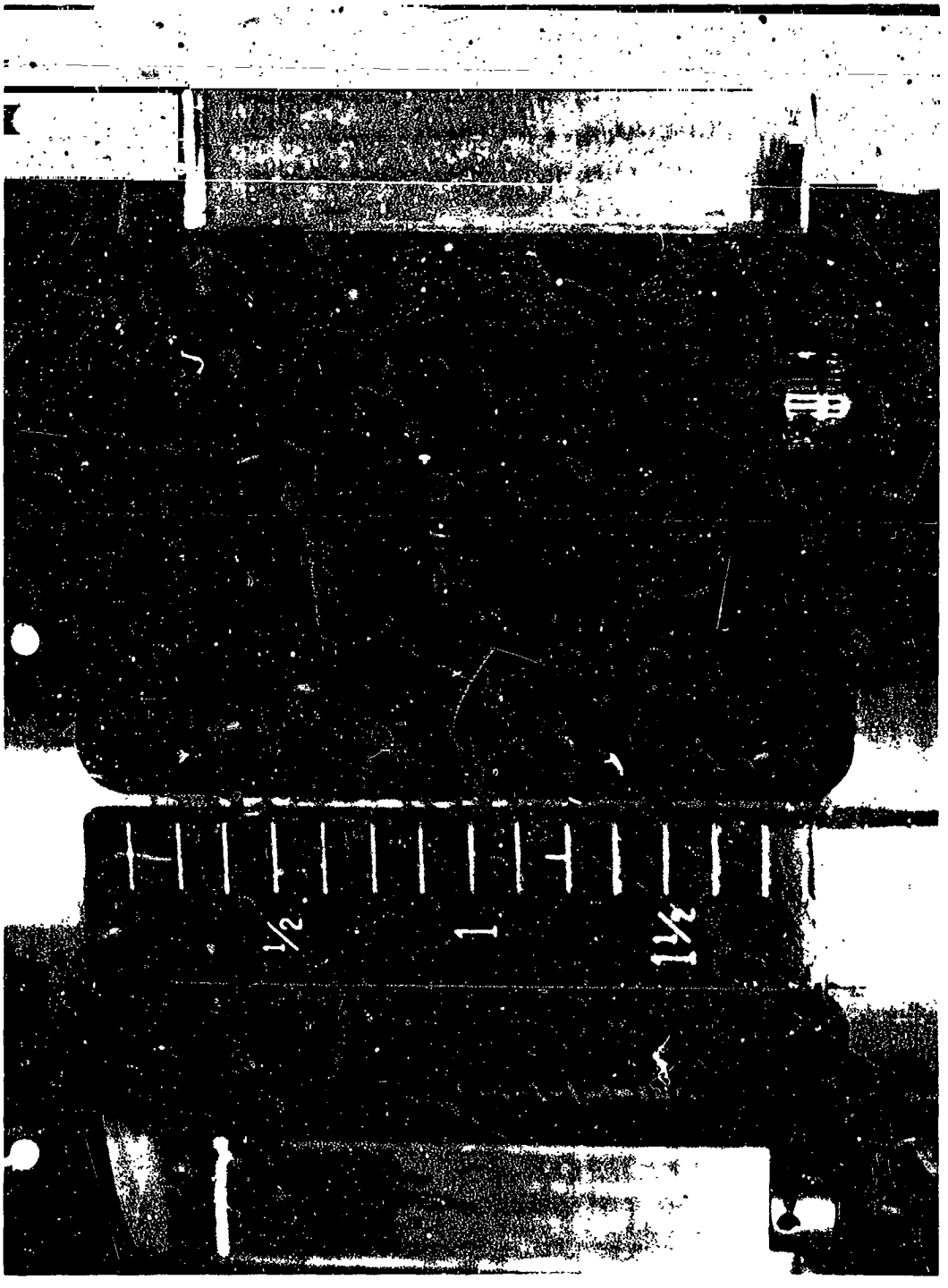

Mercury Interface - Configuration 10
(Housing Grooves, 0.0051 in. Radial Clearance;
N = 12,000 rpm; T = 305°F; ΔP = 110 psi)

Figure 42

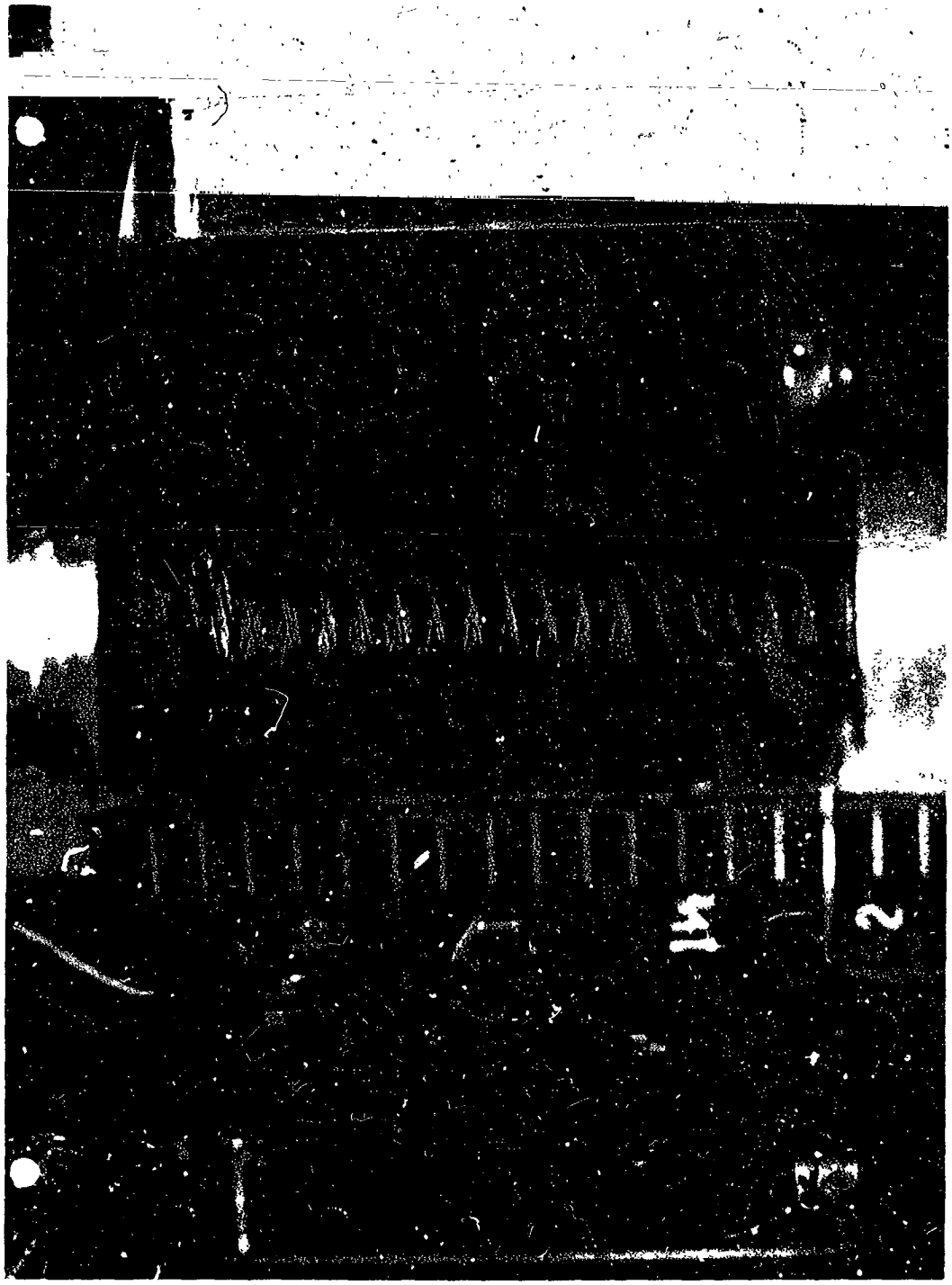

Mercury Interface - Configuration 11
(Housing and Shaft Grooves, 0.0067-in.-Wide Radial Clearance;
N = 12,000 rpm; T = 310°F; ΔP = 120 psi)

Figure 43

Mercury Interface - Configuration 12
(Shaft Grooves, 0.0067 in. Radial Clearance;
N = 12,000 rpm; T = 300°F; ΔP = 82.5 psi)
Upper Contact Seal Broke Down, Leaving Carbon Deposit on Quartz Housing

Figure 44

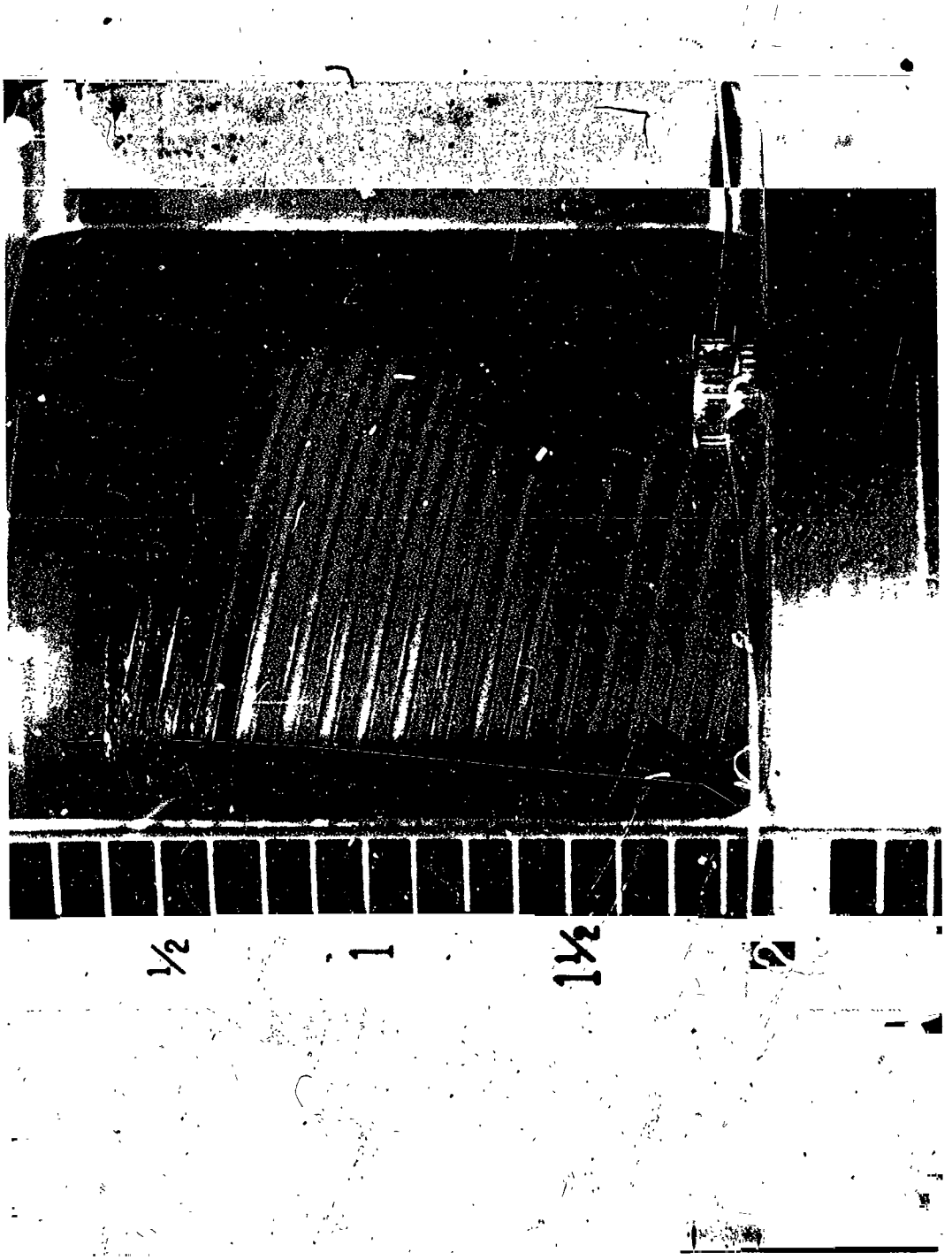

Mercury Interface - Configuration 6
(Shaft Grooves, 0.003 in. Radial Clearance;
N = 6220 rpm; T = 126°F; ΔP = 38 psi)

Figure 45

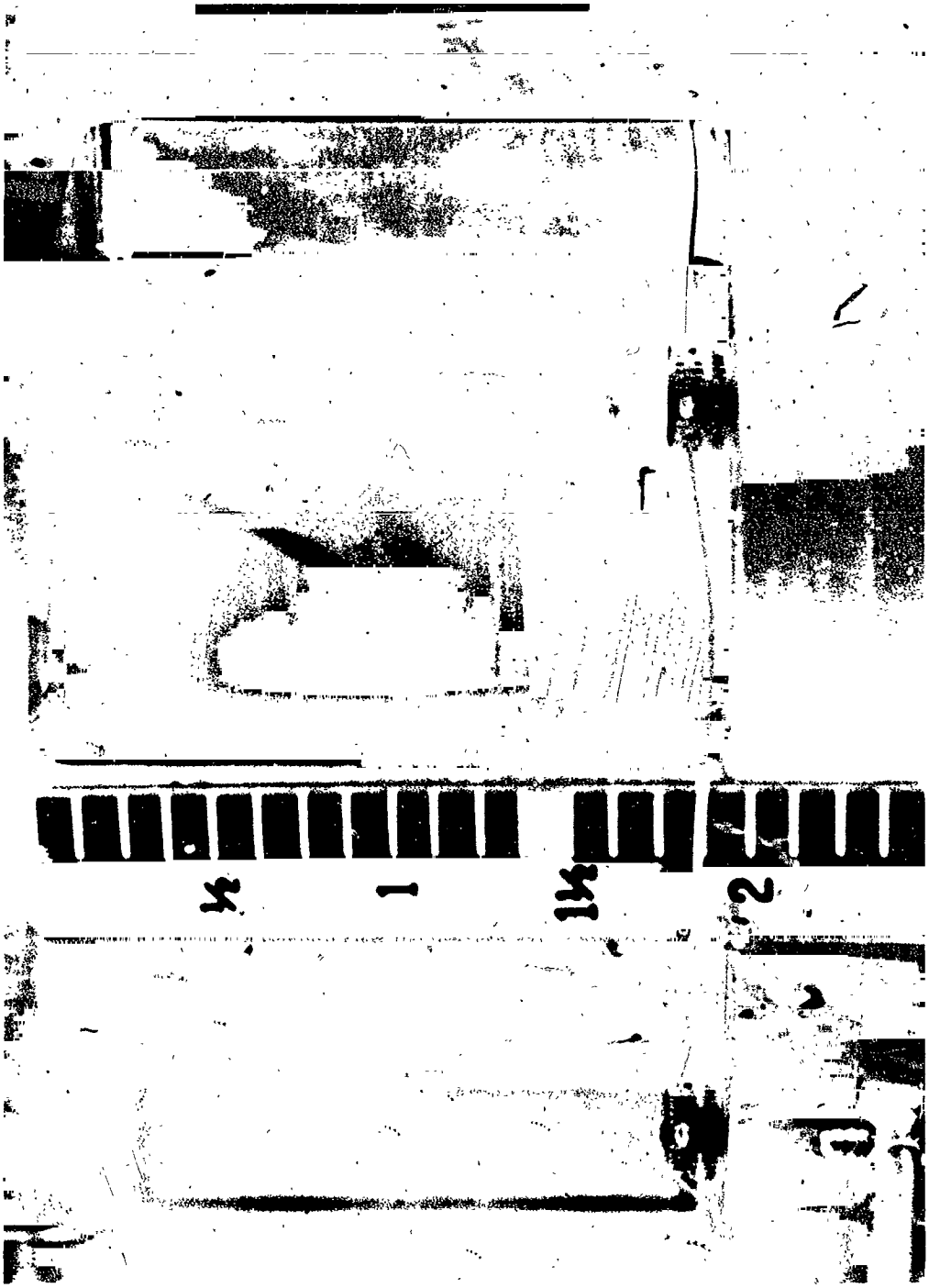

Mercury Interface - Configuration 8
(Shaft Grooves, 0.0048 in. Radial Clearance;
N = 5980 rpm; T = 145°F; ΔP = 70 psi)

Figure 46

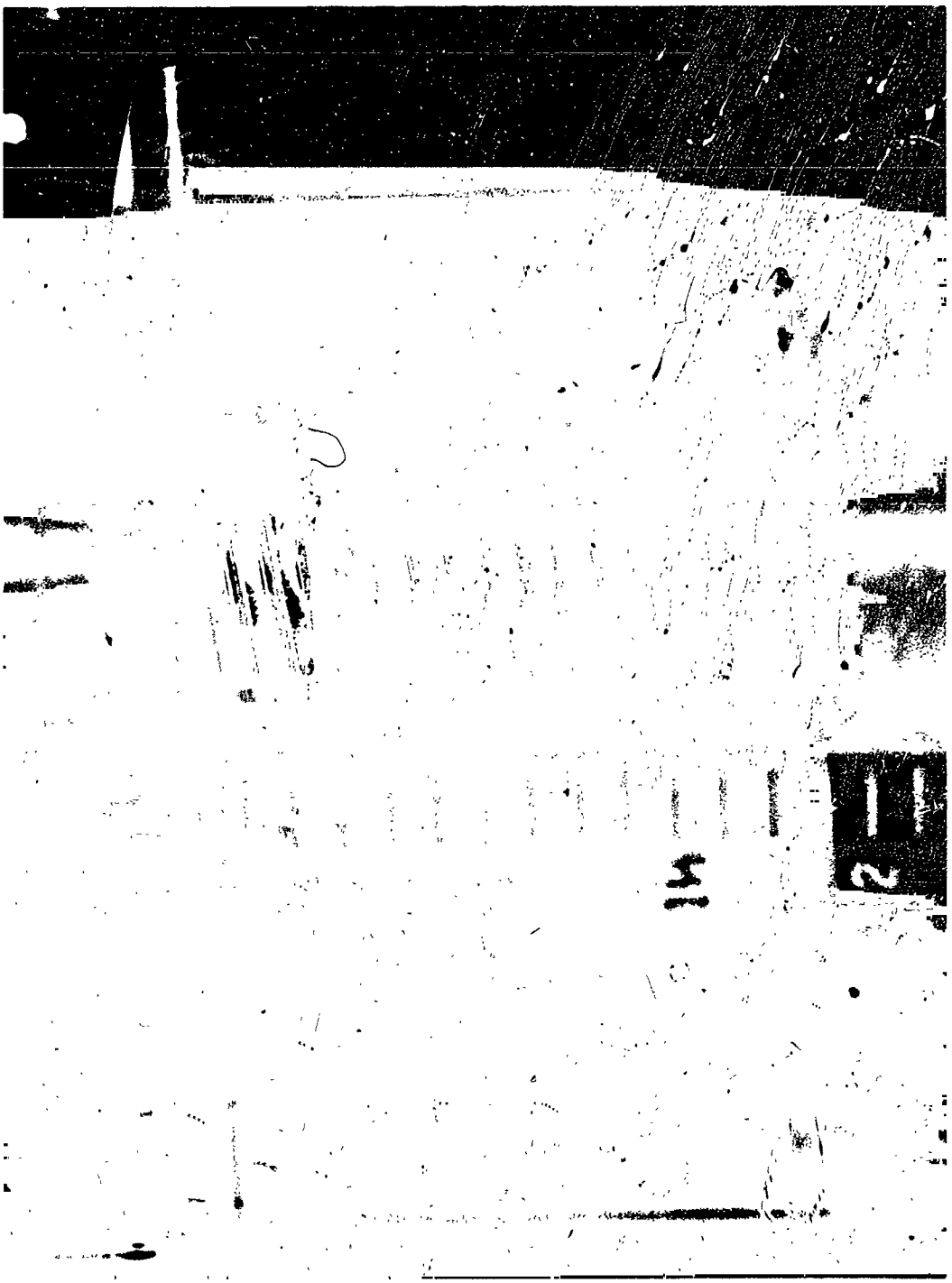

Mercury Interface - Configuration 9
(Housing and Shaft Grooves, 0.0048 in. Radial Clearance;
N = 6000 rpm; T = 135°F; ΔP = 80 psi)

Figure 47

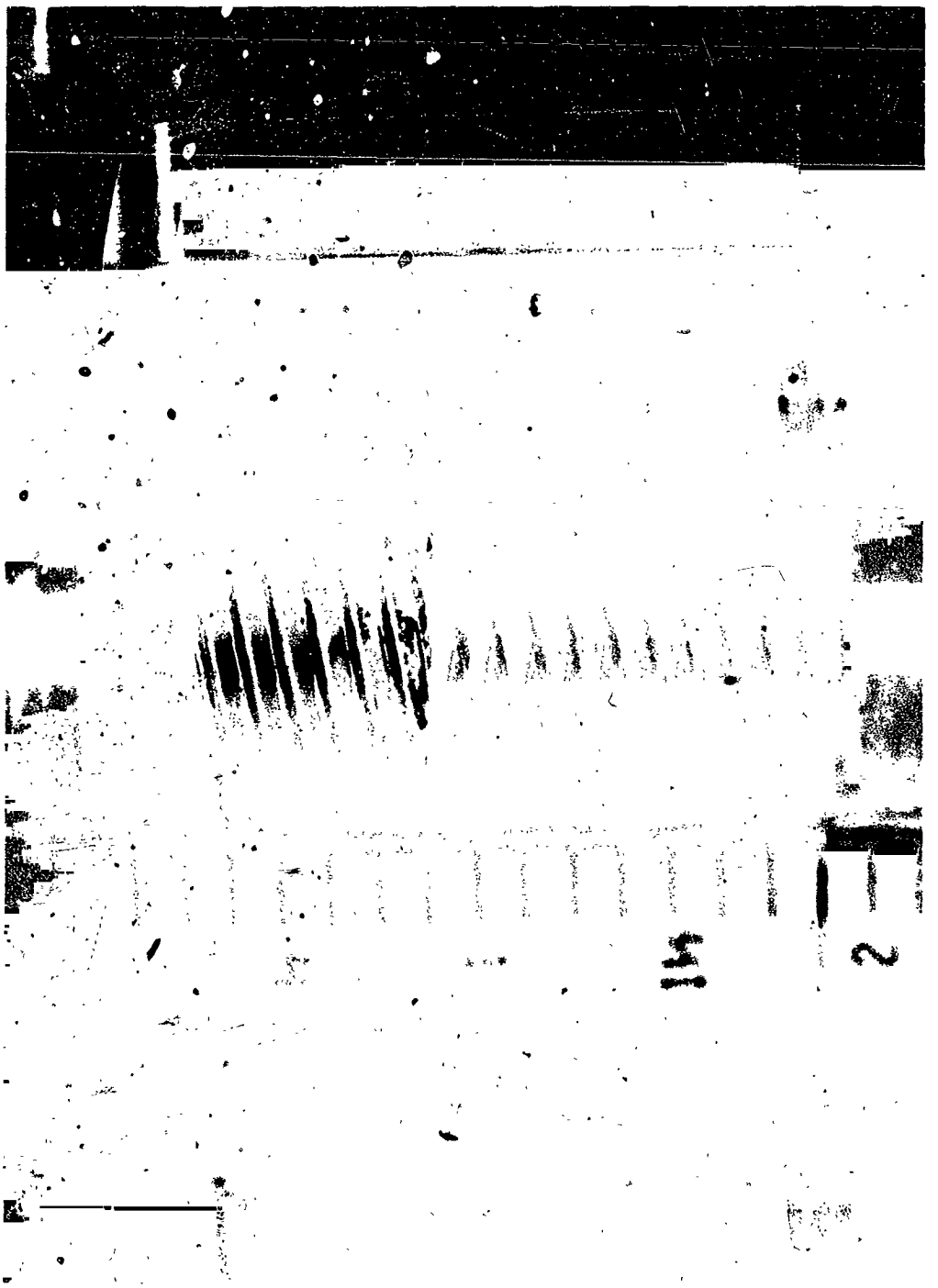

Mercury Interface - Configuration 11
(Housing and Shaft Grooves, 0.0067 in. Radial Clearance;
N = 6000 rpm; T = 125°F; ΔP = 70 psi)

Figure 48

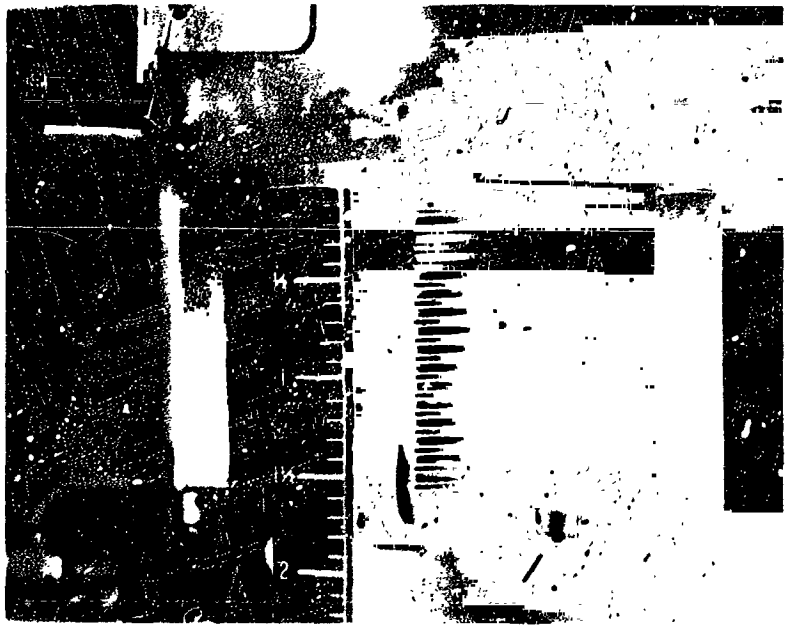

A - N = 12,000 rpm; ΔP = 37 psi

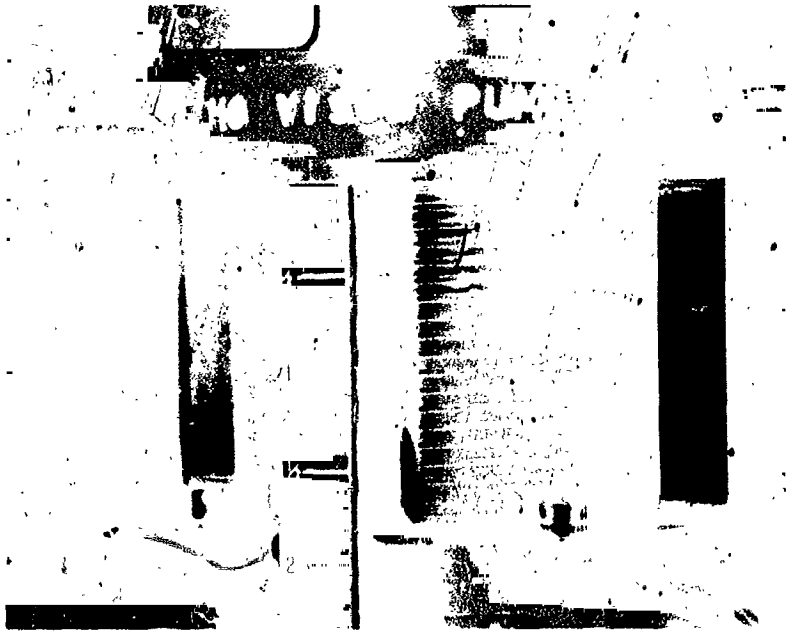

B - N = 12,150 rpm; ΔP = 4.6 psi

Incipient Breakdown - Configuration 4

Figure 49

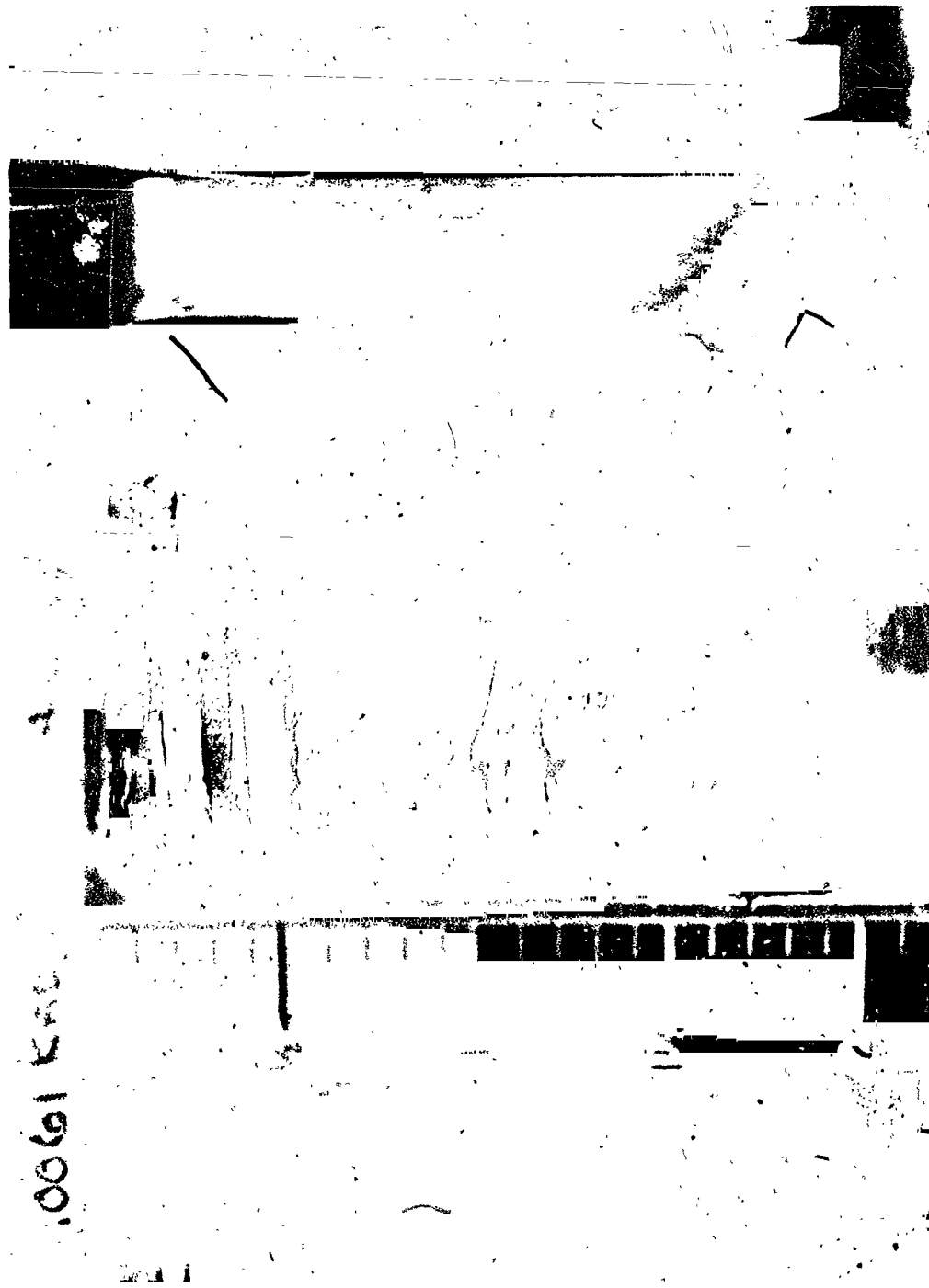

Complete Breakdown - Configuration 1
(Housing Grooves, 0.006 in. Radial Clearance;
0.004 in. Groove Depth; N = 12,000 rpm)

Figure 50

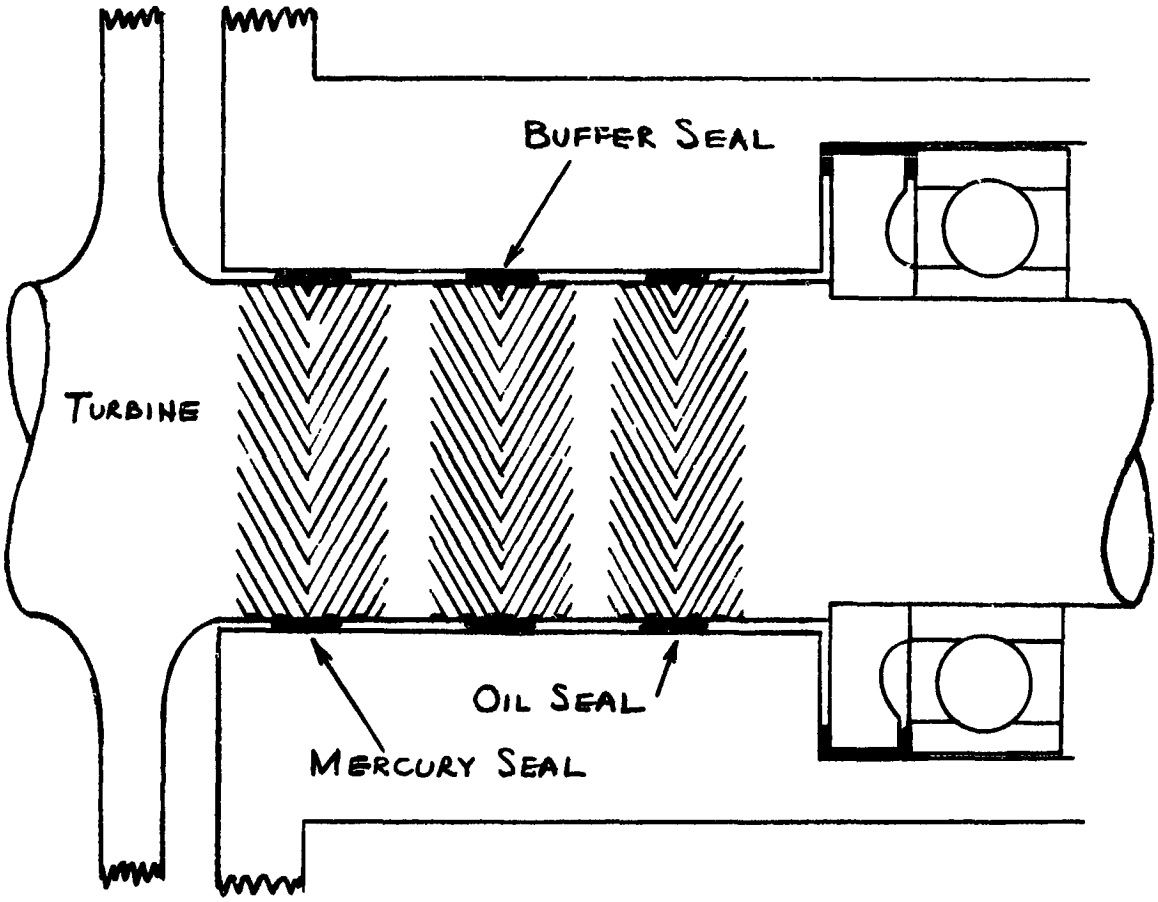

Zero Leakage Seal

Figure 51

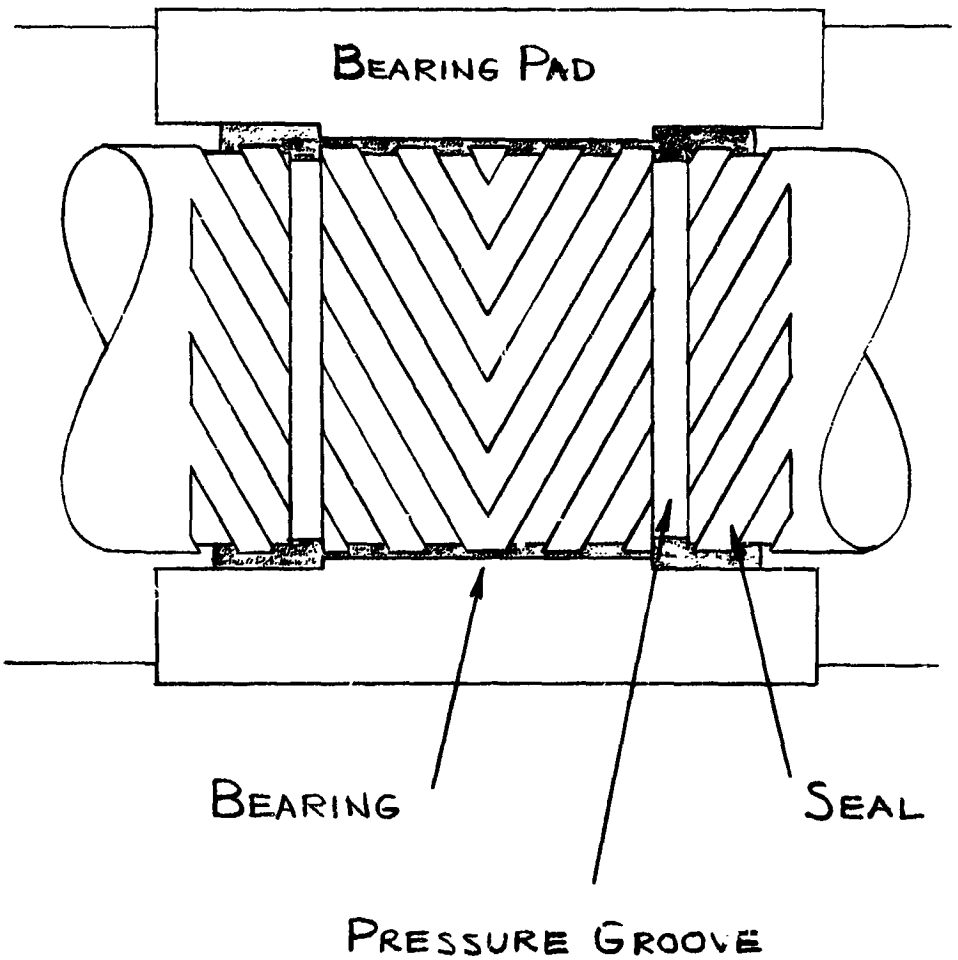

Herringbone Visco Bearing

Figure 52

APPENDIX

THEORY OF VISCO-PUMP OPERATION*

*From An Experimental Evaluation of Three Types of Visco Seals, by J. M. McGrew, General Electric Report No. 63GL173, Jan. 28, 1964.

I. SUMMARY

The performance of the visco pump is derived analytically for both laminar and turbulent flow.

The laminar analysis shows that the pumping coefficient

$$\psi_\ell = \frac{\Delta p\, \delta^2}{L\, \mu\, V}$$

is a constant and that the value of the constant depends on the configuration of the helical channels.

The turbulent analysis shows that the pumping coefficient is a function of Reynolds Number of the following form:

$$\psi_t = K_1 + K_2\, Re^n$$

Specific coefficients derived analytically vary considerably depending on the assumptions made and in general tend to give values higher than those found experimentally. The best experimental data gives

$$\psi_t = 0.313 + 4.3 \times 10^{-4}\, Re_\delta^{1.044}$$

for the optimum configuration of Zotov* where

$$Re_\delta = \frac{r\, \omega\, \delta}{\nu}$$

An optimum channel geometry based on a simplified laminar model is derived. The results are as follows:

Helix angle = 21.6°

Radial clearance/groove depth = 0.36

Groove width = land width

*V. A. Zotov, "Research on Helical Groove Seals," Machine Design and Calculation (Russia), Issue No. 10.

The results of a more complex laminar analysis by Zotov* are discussed and judged to be the most reliable definition of optimum channel configuration currently available.

The Zotov criteria are as follows

Helix angle = 14.5°

Radial clearance/groove depth = 0.32

Groove width/groove width + land width = 0.63

Groove depth/groove width = 0.08

This differs from the criteria of the simplified analysis in that the helix angle is smaller and the number of thread flights is indirectly specified.

II. THEORY OF SCREW SEAL OPERATION

In this section the equations describing screw seal operation in the laminar region are developed, including the effect of internal leakage across the thread lands. Following the laminar-flow treatment, an analysis is presented predicting the effect of turbulence with no land leakage.

A. LAMINAR FLOW SEALING CAPABILITY

The screw seal is essentially a pump operating at a zero internal flow. Therefore, the screw pump operation will be discussed, with the screw seal as a special case. The screw pump usually consists of a threaded shaft rotating in a fixed sleeve. It is far more convenient, however, to visualize the threaded shaft as the stationary member. The sleeve then appears to rotate opposite in direction to the actual shaft motion.

Figure A-1 shows a portion of a screw pump in which the rotational speed of the sleeve relative to the shaft is U. The component V tends to drag the fluid in the direction of the channel. The T component induces a transverse flow which is neglected in the analysis. Figure A-2a illustrates an element of the helical channel with only the relative velocity component V existing on the sleeve. Figure A-2b pictures the velocity distribution at a cross-section of the channel with no pressure gradient.

As shown in Reference 1, the laminar flow equation for this simplified model is

$$\frac{dp}{d\xi} = \mu \frac{d^2u}{dy^2} \qquad (1)$$

*Ibid.

where

p = pressure

ξ = coordinate along groove

μ = absolute viscosity

u = velocity along groove

y = coordinate in radial direction

Introducing the boundary conditions

$$y = o; \quad u = o$$
$$y = h; \quad u = \frac{V}{1 + \beta}$$

where

h = groove depth

$\beta = \delta/h$

δ = radial clearance

The solution for Equation 1 is given by

$$\frac{Q}{Vwh} = \frac{1}{2(1 + \beta)} - \frac{1}{12}\left[\frac{h^2}{\mu V}\frac{dp}{d\xi}\right] \tag{2}$$

where

w = groove width

$$Q = w\int_o^h udy = \text{volume flow} \tag{3}$$

The first righthand term of Equation 2 is the drag flow. The second term represents the backward flow along the channel due to the negative pressure gradient. The total flow can be viewed as a drag flow minus a pressure flow minus a leakage flow over the lands, or

$$Q = Q_d - Q_p - Q_\ell \tag{4}$$

The flow components are put in terms of the visco pump geometry by reference to Figure A-1 where

$$V = U \cos \phi = \pi DN \cos \phi \tag{5}$$

$$d\xi = dx/\sin \phi \tag{6}$$

$$t = nt^* = \pi D \tan \phi \tag{7}$$

$$w = (t^* - e) \cos \phi \tag{8}$$

where

ϕ = helix angle

D = diameter

N = speed

x = coordinate along shaft axis

t = pitch

n = number of thread flights

t^* = t/n

e = land width along axis

The axial leakage over the lands is given in Reference 2 as

$$Q_\ell = \frac{E\pi Dt\delta^3\Delta p}{12\,\mu neL}$$

where

E = eccentricity correction factor

L = wetted length of seal

Substitution of the above into Equations 2 and 4 gives

$$Q = \frac{nhU(t^*-e)\cos^2\phi}{2\,(1+\beta)} - \frac{nh^3(t^*-e)\sin\phi\cos\phi\Delta p}{12\,\mu\,L} - \frac{E\pi Dt\delta^3\Delta p}{12\,\mu neL} \tag{9}$$

For operation as a seal it is desired that Q = 0. Setting Q = 0 in Equation 9 and rearranging to form dimensionless quantities,

$$\psi = \frac{\delta^2\Delta p}{\mu\,UL} = \frac{6\beta^2\,(1+\beta)^{-1}}{\tan\phi + \dfrac{\tan\phi\,E\beta^3}{\gamma\,(1-\gamma)\sin^2\phi}} \tag{10}$$

where

$\gamma = \frac{w}{w+w'}$

w = groove width

w' = land width

The dimensionless coefficient $\frac{\Delta p\delta^2}{\mu\,UL}$ is designated the laminar sealing coefficient ψ_ℓ. It is seen in Equation 10 to be a function of geometry alone. Figure A-3 shows the sealing coefficient plotted vs helix angle for the optimum values of β and γ.

With no leakage flow ($Q_\ell = 0$), Equation 10 becomes

$$\gamma_\ell = \frac{6\varepsilon^2 (1+\beta)^{-1}}{\tan \phi} \tag{11}$$

B. EFFECT OF ECCENTRICITY ON SEALING CAPABILITY

Equation 10 reveals that the leakage flow over the screw lands is strongly influenced by the position of the shaft in the sleeve. The sealing coefficient, γ, is a function of eccentricity due to the factor E which varies from a value of 1.0 to 2.5 as the eccentricity varies.

Assuming the two extreme values for the eccentricity factor E, we can calculate the sealing coefficient variation corresponding to minimum and maximum eccentricity, respectively. This is shown in Figure A-4 for a selected geometry. The cross-hatched area between the extreme values of the sealing coefficient defines the range of laminar sealing coefficients.

C. LAMINAR FLOW POWER LOSS

The simplest method for estimating the power loss in a screw seal is to treat the loss as frictional dissipation by viscous shear in an annulus which has a clearance, δ, over part of its area and a clearance, h, for the remaining part. The force exerted on the shaft is simply

$$F = \frac{\mu U}{\delta} A_\ell + \frac{\mu U}{(\delta+h)} A_g \tag{12}$$

where

A_ℓ = area of lands

A_g = area of grooves

and the power is

$$P = F U$$

By observing that

$$\gamma = \frac{A_g}{A_\ell + A_g}$$

and

$$\beta = \frac{\delta}{h}$$

$$A = A_\ell + A_g$$

the expression for power becomes

$$\frac{P \delta}{\mu U^2 A} = \left[\frac{\gamma \beta}{\beta + 1} + (1 - \gamma) \right] \tag{13}$$

or

$$\frac{P}{\pi U \Delta p} = \frac{\delta D}{\gamma_\ell}\left[\frac{\gamma \beta}{\beta + 1} + (1 - \gamma)\right] \tag{14}$$

It can be seen that the right-hand side is a function of geometry alone. Hence, in laminar flow for a given speed and required sealing pressure, power is independent of fluid viscosity.

The power loss data may also be presented in terms of a friction factor f, defined as

$$f = \frac{F/A}{\frac{\rho U^2}{2g}} \tag{15}$$

where

ρ = density

F is given by Equation 12. Equation 15 can be rewritten as

$$f = \frac{2}{Re}\left[\frac{\gamma \beta}{\beta + 1} + (1 - \gamma)\right] \tag{16}$$

where

Re = Reynolds No.

The drag can be specified in terms of a drag coefficient based on the following drag relationship:

$$\lambda = \frac{T}{\frac{\rho \omega^2}{2g} r^4_L} \tag{17}$$

where

T = torque

ω = angular velocity

r = radius

It also is noted that

$$\lambda = \frac{Fr}{\frac{\rho U^2}{2g} r^2_L} = 2\pi \frac{F/A}{\frac{\rho U^2}{2g}} = 2\pi f \tag{18}$$

which gives for laminar flow

$$\lambda = \frac{4\pi}{Re_\delta}\left[\frac{\gamma \beta}{\beta + 1} + (1 - \gamma)\right] \tag{19}$$

In Reference 3 the frictional characteristics of an unloaded journal bearing are given in terms of the friction factor, f. In laminar flow the friction factor is given by Equation 16. In the turbulent flow regime, the friction was shown to be given by

$$f = \frac{0.078}{Re_\delta^{0.43}} \tag{20}$$

or in terms of the moment coefficient for an unloaded journal of clearance, δ, over part of its area and h over the remaining area

$$\lambda = \frac{0.156\pi}{Re^{0.43}}\left[\frac{\gamma\,\beta}{\beta + 1} + (1 - \gamma)\right] \tag{21}$$

The previous analysis of loss has included only couette or drag flow. In addition there is a Poisseuille or pressure flow within the groove which also contributes to the power loss. Boon and Tal (Reference 4) performed an analysis in which this additional factor was considered. Their analysis shows the loss attributable to the Poisseuille portion of the flow is very small in comparison to the viscous losses. We have therefore chosen to neglect it.

D. OPTIMIZATION FOR MAXIMUM SEALING CAPABILITY

Optimization of Simplified Sealing Equation

The sealing coefficient, ψ_ℓ, can be maximized by taking the partial derivatives of ψ_ℓ with respect to β, γ, and ϕ and setting these partial derivatives equal to zero. A system of 3 equations results, the solution of which yield values of β, γ, and ϕ for which ψ_ℓ is a maximum.

$$\frac{\partial \psi_\ell}{\partial \phi} = 0 = K - \sin^2\phi\,(1 + 2K) \tag{22a}$$

$$\frac{\partial \psi_\ell}{\partial \gamma} = 0 = 2\gamma - 1 \tag{22b}$$

$$\frac{\partial \psi_\ell}{\partial \beta} = 0 = \frac{E}{\gamma\,(1-\gamma)\,\sin^2\varphi}\,(2\beta^4 + \beta^3) - \beta - 2 \tag{22c}$$

The simultaneous solution of the above equations gives

$$\phi = 21.6^\circ$$
$$\beta = 0.36$$
$$\gamma = 0.5$$

The value of ψ for these conditions is

$$\psi_\ell = 0.61$$

Optimization of the sealing coefficient based on the clearance gives the added information that there is an optimum groove depth for a given clearance, δ. For tight clearances, however, the optimum ratio of clearance to groove depth leads to very shallow grooves. For a 0.5 mil clearance, the optimum groove depth is only 1.5 mils. Such a groove is very difficult to machine. In order to estimate the sealing coefficient at other than optimum conditions, the following method can be used.

From Equation 22b the condition $\gamma = 0.5$ is an optimum condition independent of the value of ϕ and β. Substituting for γ and letting $K_o = 4E\beta^3$ for $\gamma = 0.5$, we obtain

$$\phi_o = \sin^{-1}\left[\frac{K_o}{2K_o + 1}\right]^{1/2} \tag{23}$$

Then

$$\psi_o = \frac{3\,(1+\beta)^{-1}\,\beta^2}{2\left[E\beta^3\,(1+4E\beta^3)\right]^{1/2}} \tag{24}$$

This is plotted in Figure A-5 for the two extreme values of the eccentricity factor E.

For any value of β with $\gamma = 0.5$, an optimum value of ψ_ℓ can be read from Figure A-5. The helix angle required to attain this value of ψ_ℓ is calculated from Equation 23 or read from Figure A-6.

In Figure A-5 it is seen that eccentricity markedly reduces the sealing coefficient but hardly changes the value of β where the sealing curve reaches a maximum. In Table A-1, the values of β required for maximum sealing coefficient as reported in several different references range from 0.2 to 0.38. Figure A-5 indicates that in this range of β, the sealing coefficient changes little and that any of these "optima" would give good sealing capability.

For values of β below 0.2, however, the curve drops off sharply; for a given clearance, a considerable penalty in reduced sealing capability is paid by using small values of β.

Figure A-6 provides the value of helix angle required to attain the sealing coefficients given in Figure A-5 as a function of β. The effect of eccentricity is to increase the helix angle required to obtain maximum sealing for any given β.

The previous analysis was based on a simplified model of the screw seal in that the edge effects of the channel were neglected. The analysis is therefore limited to channels which are much wider than they are deep, or h/w (the aspect ratio) is small. Other investigators have included aspect ratio and other effects in determining optimum conditions.

Table A-1 summarizes the various screw seal optimizations for laminar operation.

TABLE A-1

SUMMARY OF OPTIMUM GEOMETRY FOR
LAMINAR SCREW SEAL OPERATION

	ψ_ℓ theor	ψ_ℓ meas	ϕ	δ/h	$\gamma = \frac{w}{w' + w}$	h/w	Test Regimes
1. Zotov - Reference 5	0.69	0.37-0.69	14.5°	0.32	0.63	0.08	Lam & Turb $Re_{h_{cr}} = 1300$
2. Asanuma - Reference 6	0.45	0.33-0.36	10°~11°	0.2	0.5	0.05~0.2	Lam
3. Boon and Tal - Reference 4	0.55	--	15.8°	0.38	0.5	--	Lam
4. Frossel - Reference 7	--	0.122*	12°	0.007*	--	--	Lam
	--	0.18*	15°~20°	0.16*	--	--	Lam
5. Whipple et al. - References 8 and 9	0.55	--	13.8°	0.38	0.5	--	Lam
6. Hughes - Reference 10	0.55	0.47	13.8°	0.38	0.5	0.055	Lam
7. McGrew and McHugh - Reference 11	0.61	0.313	21.6°	0.36	0.5	--	Lam & Turb
8. Present study	0.61	0.45-0.49	21.6°	0.36	0.5	--	Lam & Turb

*Not optimum value.

It will be seen that the analysis based on a simplified model gives results which are close to those given by the more complicated analyses. The largest discrepancy between the simplified analysis and the other optimizations in Table A-1 is in the helix angle required for maximum sealing. The simplified approach gives angles from 7 to 10° larger than the other methods.

E. TURBULENT FLOW SEALING CAPABILITY

The general two-dimensional turbulent flow equations for the fluid in the screw channel are taken from Reference 1. These equations are reproduced below.

$$\frac{\partial p}{\partial \xi} = \mu \frac{\partial^2 \bar{u}}{\partial y^2} + \frac{\partial \overline{(-\rho u'v')}}{\partial y} \tag{25}$$

and

$$\frac{\partial u}{\partial \xi} + \frac{\partial \bar{v}}{\partial y} = 0 \tag{26}$$

In Reference 12, a study is made of the turbulent hydrodynamic motion in a lubricant layer, and a solution is obtained for Equation 25 by introducing Prandtl's mixing length, ℓ, where

$$\overline{-\rho u'v'} = \rho \ell^2 \frac{\partial \bar{u}}{\partial y} \left| \frac{\partial \bar{u}}{\partial y} \right| \tag{27}$$

The mixing length, ℓ, is defined as

$$\ell = ky \qquad 0 \leq y \leq \frac{h}{2}$$

$$\ell = k(h-y) \quad \frac{h}{2} \leq y \leq h \tag{28}$$

where k is an empirical factor that must be determined by experiment. This has been done by measuring the fully developed turbulent velocity profile in a pipe. Measurements of this type yield values of k = 0.4.

After substituting Equation 27, Equation 25 is integrated in Reference 12 to obtain velocity profile as a function of pressure coefficient and Reynolds number. The Reynolds number has substantial influence upon the velocity profile; when Re $\rightarrow$ 0 the velocity profile tends towards the laminar one, and when Re $\rightarrow \infty$ the velocity distribution tends to become constant with respect to y. The resulting mean velocity is

$$u_m = \frac{1}{h} \int_0^h u dy$$

This mean velocity in the screw channel can be thought of as consisting of two parts:

$$u_m = u_{m_c} + u_{m_p}$$

where

u_{m_c} = mean couette velocity

u_{m_p} = mean pressure velocity (29)

Since it can be shown that the mean couette velocity, u_{m_c}, is independent of Reynolds number, the mean velocity is then given by

$$u_m = \frac{V}{2} + u_{m_p} \tag{30}$$

For laminar flow, neglecting internal seal leakage, this becomes

$$\frac{u_m}{V} = \frac{1}{2} + \frac{B}{12} \tag{31}$$

where

B = dimensionless pressure, $\frac{h^2 \Delta p}{\mu V d s}$

From Reference 12, the pressure coefficient can be expressed analytically as

$$B = k' \left(\frac{u_{m_p}}{V} \right)^n \tag{32}$$

where

$k' = 12$ for $Re = 0$

$k' = \infty$ for $Re \longrightarrow \infty$

This variation in k' can be expressed as

$$k' = K_1' + K_2' \, Re^n$$
$$= 12 + 0.14 \, Re^{0.725} \tag{33}$$

Substituting for u_{m_p} in Equation 30 we obtain

$$\frac{Q}{Vwh} = \frac{u_m}{V} = \frac{1}{2} + \frac{B}{\left[K_1' + K_2' \, Re^{0.725} \right]} \tag{34}$$

$$\frac{Q}{Vwh} = \frac{u_m}{V} = \frac{1}{2} + \frac{B}{\left[12 + 0.14\ Re^{0.725}\right]} \tag{35}$$

For Reynolds number = 0, this reduces to the laminar case with no leakage as shown in Equation 11. The dimensionless pressure coefficient vs the dimensionless flow coefficient is plotted in Figure A-7, which shows the dependence of screw pump performance on Reynolds number.

When the screw pump is adapted for use as a seal, the important point on the characteristic is the shutoff pressure (i.e., the value of pressure coefficient at zero flow).

From Equation 35, the shutoff value is given by

$$\frac{dp}{d\xi}\frac{h^2}{uV} = \frac{1}{2}\left[12 + 0.14\ Re^{0.725}\right] \tag{36}$$

A more recent study in turbulent lubrication theory in Reference 13 differs with the results obtained by Constantinescu. The new study using Reichardt's formula to evaluate the effective fluid viscosity in turbulent flow results in different values of K_2' and n. The study further predicts that the values of K_2' and n change depending upon the Reynolds number ranges. Values for K_2' and n are listed below in Table A-2 for comparison.

TABLE A-2

Method	K_2'	n	Range of Application
Constantinescu (Reference 12)	0.140	0.725	$0 \leq Re \leq \infty$
Ng (Reference 13)	0.00725	1.003	$500 \leq Re \leq 5000$
	0.0395	0.803	$5000 \leq Re \leq 50{,}000$

The constants in Equation 31 and Table A-2 are based on values of k (Equation 28) measured in pipe flow experiments. The values of the pressure coefficient measured in screw seal experiments are much lower than those predicted by Equation 36. This discrepancy is in part due to the fact that Equation 31 neglects leakage flow over the land. However, even in the laminar flow analysis where land leakage is included, measured values of sealing coefficient are considerably lower than the theoretical values.

Since Equation 36 ultimately rests on an experimentally determined constant, the approach here has been to demonstrate the form of the turbulent sealing equation and then to evaluate the constants K_1, K_2, and n experimentally. Thus we would expect the expression for the turbulent sealing equation to be of the form

$$\gamma_t = K_1 + K_2\ Re_h^n \tag{37}$$

where the constants are a function of geometry alone.

In Reference 11, these constants were evaluated experimentally for the Zotov geometry, the first entry in Table A-1. The values found were

$$\psi_t = 0.313 + 1.31 \times 10^{-4} \, Re_h^{1.044} \tag{38}$$

In terms of the Reynolds number based on clearance this equation becomes

$$\psi_t = 0.313 + 4.3 \times 10^{-4} \, Re_\delta^{1.044} \tag{39}$$

F. SIMILARITY RELATIONS FOR THE VISCO SEAL

In order to derive the similarity laws for any device, an accurate knowledge of the physical process involved is required. The laws which govern screw seal operation are a special case of the Navier-Stokes equations. The Navier-Stokes equations are well known, but there are no general methods for their solution. The Navier-Stokes equation for laminar incompressible flow is given by

$$\frac{\partial \vec{V}}{\partial t} + (\vec{V} \text{ grad}) \vec{V} = \vec{g} - \frac{1}{\rho} \text{ grad } \vec{p} + \frac{\mu}{\rho} \nabla^2 \vec{V} \tag{40}$$

The above equation contains forces due to pressure, viscosity, inertia, and gravity. Now from similarity theory it is known that full-scale processes and model processes are similar if:

1. The two systems are geometrically similar
2. The two systems are dynamically similar
3. The two systems have equal dimensionless boundary and initial conditions.

The two systems can be made geometrically similar by scaling their dimensions. For a screw seal this means that the dimensions should be scaled directly (i.e., δ/R, $w/(w + w')$, ϕ, δ/h, L/D, and w/h must be maintained for both the full-scale seal and the model seal).

The dimensionless criteria for dynamic similarity are found by transforming the Navier-Stokes equations into dimensionless form, that is

$$\frac{\ell_o}{U t_o} \frac{\partial \vec{V}}{\partial T} + (\vec{V} \text{ grad}) \vec{V} = \frac{g \vec{\ell_o}}{U^2} - \frac{p_o}{\rho U^2} \nabla \vec{p} + \frac{\mu}{\rho U \ell_o} \nabla^2 \vec{V} \tag{41}$$

where ℓ_o, t_o, U, and p_o are reference quantities.

The fluid motions in the two seals, full-scale and model, are similar only if the solutions for the above equation in both systems are identical. This requires that the coefficients in the above equation must be equal for full-scale and model seals. For the steady-state case, this means

$$\left[\frac{U^2}{g\ell_o}\right]_1 = \left[\frac{U^2}{g\ell_o}\right]_2 \qquad \text{Froude No.}$$

$$\left[\frac{\rho U\ell_o}{\mu}\right]_1 = \left[\frac{\rho U\ell_o}{\mu}\right]_2 \qquad \text{Reynolds No.}$$

$$\left[\frac{p_o}{\rho U^2}\right]_1 = \left[\frac{p_o}{\rho U^2}\right]_2 \qquad \text{Pressure Coefficient}$$

where the subscripts 1 and 2 refer to the full-scale and model seal respectively. It is interesting to note that the sealing coefficient is given by

$$\frac{\Delta p \delta^2}{\mu UL} = \left(\frac{\rho U \delta}{\mu}\right)\left(\frac{\Delta p}{\rho U^2}\right)\left(\frac{\delta}{L}\right) \tag{42}$$

which is the product of the Reynolds number, pressure coefficient, and a geometrical ratio.

The remaining condition which must be satisfied to ensure similarity between the model and full-scale seal is that the dimensionless boundary and initial conditions are equal. Since we are concerned with the steady state, the initial conditions are unimportant. The boundary conditions which require that the fluid be at rest with respect to the boundary are satisfied in both full-scale and model. The boundary condition at the fluid-air interface must satisfy the surface tension equation; that is

$$p_\ell = p_g + \sigma\left(\frac{1}{R_1} + \frac{1}{R_2}\right) \tag{43}$$

where p_ℓ is the liquid pressure, p_g the gas pressure, σ = fluid surface tension, and R_1 and R_2 are the principal radii of curvature of gas-liquid interface. For the screw seal $R_1 \approx \delta/2$ and $R_2 = \infty$. Therefore

$$p_\ell = p_g + \frac{2\sigma}{\delta} \tag{44}$$

Writing this in dimensionless terms

$$\underline{p}_\ell = \underline{p}_g + \frac{2\sigma}{p_o \ell_o \Delta} \tag{45}$$

where

$$\underline{p} = p/p_o$$
$$\Delta = \delta/\ell_o$$

This dimensionless equation must also be satisfied to ensure similarity. Now if the quantity $\sigma/(p_o \ell_o)$ is multiplied by $p_o/(\rho U^2)$, the inverse of the familiar Weber number is obtained. The additional requirement for similarity can then be expressed as

$$\left[\frac{U^2 \ell_o \rho_o}{\sigma}\right]_1 = \left[\frac{U^2 \ell_o \rho_o}{\sigma}\right]_2 \qquad \text{Weber No.}$$

It should also be noted that the surface tension is a function of both the liquid and the gas. However, in most gas-liquid systems a change in the nature of the gas produces no appreciable change in σ. Hence the interfacial tension of a liquid-gas system is usually treated as a property of the liquid alone.

Where the interface between two fluids meets a solid, the angle of contact depends upon the nature of the solid surface. Thus, strictly speaking, the liquid-gas-solid wetting characteristics must also be the same for both full-scale and model seal.

The Navier-Stokes equation (Equation 40) assumes that the fluid is a continuum. If cavitation occurs this requirement is not met. The cavitation number is the parameter which describes the pressure conditions for similarity in the liquid-gas system existing in a cavitating flow. This imposes an additional requirement for similarity in a screw seal.

$$\left[\frac{p_o - p_v}{\rho U^2}\right]_1 = \left[\frac{p_o - p_v}{\rho U^2}\right]_2 \qquad (46)$$

where p_v is the vapor pressure.

Since the cavitation number is independent of the size of the physical system, it provides a means for predicting cavitation behavior of full-scale screw seal and model screw seal in order to ensure similarity. Similarity relations are summarized below.

Geometric Similarity

δ/h, δ/R, w/h, $w/(w + w')$, ϕ, L/D

Dynamic Similarity

$U^2/g\ell_o$	Froude No.
$\frac{\rho U \ell_o}{\mu}$	Reynolds No.
$p_o/\rho U^2$	Pressure coefficient
$\frac{p_o - p_v}{\rho U^2}$	Cavitation No.

Similarity of Boundary Condition

$$\frac{U^2 \ell_o \rho}{\sigma}$$ Weber No.

REFERENCES

1. H. Schlichting, Boundary Layer Theory, Pergamon Press, New York, 1955.

2. J. F. Carley and R. A. Strub, Industrial and Engineering Chemistry, 45, No. 5, May 1953.

3. M. I. Smith and D. D. Fuller, "Journal Bearing Operation at Super Laminar Speeds," Trans. of ASME, 78 (1956).

4. E. F. Boon and S. E. Tal, "Hydrodynamische Dichtung fur rotierende Wellen," (Hydrodynamic Seal for Rotating Shafts), Chemie-dug-Technik, 31, No. 3, January 31, 1959, pp. 202-12.

5. V. A. Zotov, "Research on Helical Groove Seals," Machine Design and Calculation (Russia), Issue No. 10.

6. T. Asanuma, "Studies on the Sealing Action of Viscous Fluids," International Conference on Fluid Sealing, Paper A3, April 17-19, 1961, BHRA, Harlow Essex, England.

7. W. Frössel, "Hydrodynamisch Wirkende Wellendichtung," Konstrucktion, 8, No. 11, November 1956.

8. R. T. P. Whipple, "Herring-Bone Pattern Thrust Bearing," UKHEA, Atomic Energy Research Establishment, TIM-29, August 24, 1949.

9. R. T. P. Whipple, "Theory of the Spiral Grooved Thrust Bearing with Liquid or Gas Lubricant," UKHEA, Atomic Energy Research Establishment, T/R 622, March 6, 1951.

10. D. P. Hughes, "Shaft Seal for High Gas Pressures," Paper C1, April 17-19, 1961, International Conference on Fluid Sealing, BHRA, Harlow, Essex, England.

11. J. M. McGrew and J. D. McHugh, "Analysis and Test of the Screw Seal in Laminar and Turbulent Operation," ASME Paper 64-LubS-7, presented at April 28-30 ASME Spring Lubrication Symposium, Cleveland, Ohio.

12. V. N. Constantinescu, "On Turbulent Lubrication," Proc. Instn. Mech. Engrs., 173, No. 38, 1959.

13. Chung-Wah Ng, "Fluid Dynamic Foundation of Turbulent Lubrication Theory," ASLE, Preprint for 1964 Spring Meeting.

BIBLIOGRAPHY

Daily, J. W., and Nece, R. E., "Chamber Dimension Effects on Induced Flow and Frictional Resistance of Enclosed Rotating Disks," ASME paper 59-Hyd-9, 1959.

Frössel, W., "Hochtourige Schmierölpumpe," Konstrucktion, 12, No. 5, 1960, pp. 195-203.

Snell, L. N., "Theory of Viscosity Plate Thrust Bearing Based on Circular Geometry," UKHEA, Ministry of Supply, Division of Atomic Energy (Production) 5181, October 13, 1952.

Stair, W. K., "The Visco Seal - A Survey," University of Tennessee Engineering Experiment Report No. ME-5-62-2, March 1962.

Wigg, R. E., and Battle, N., "Improvements in or Relating to Sealing Means," Great Britain Patent 834,923, May 11, 1960.

Woodrow, J., "Viscosity-Plates Flow and Loading," UKHEA, Atomic Energy Research Establishment, E/M 31, December 22, 1949.

Wordsworth, D. V., "The Viscosity Plate Thrust Bearing," UKHEA, Atomic Energy Research Establishment, E/R 2217, October 1952.

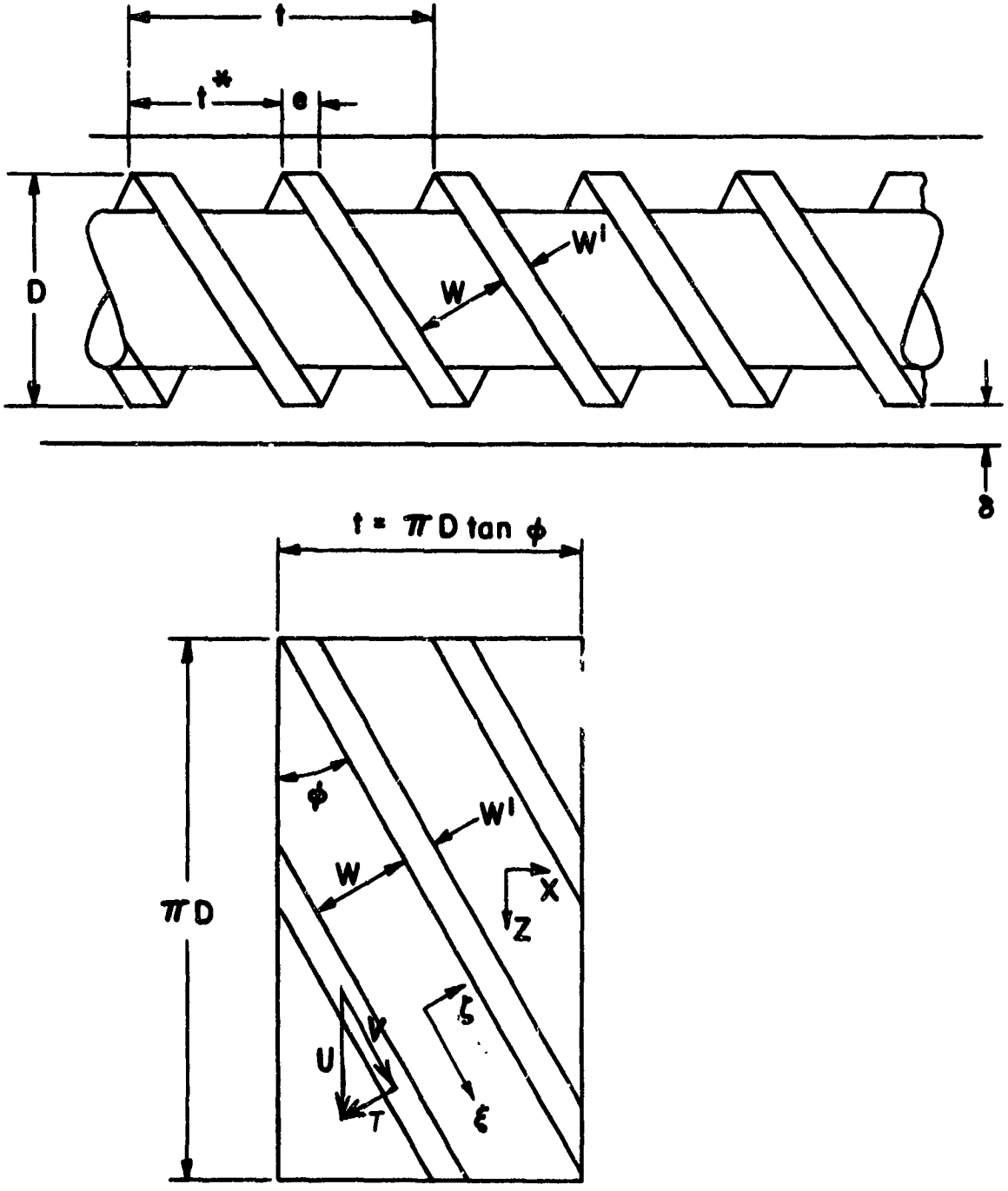

Screw Geometry

Figure A-1

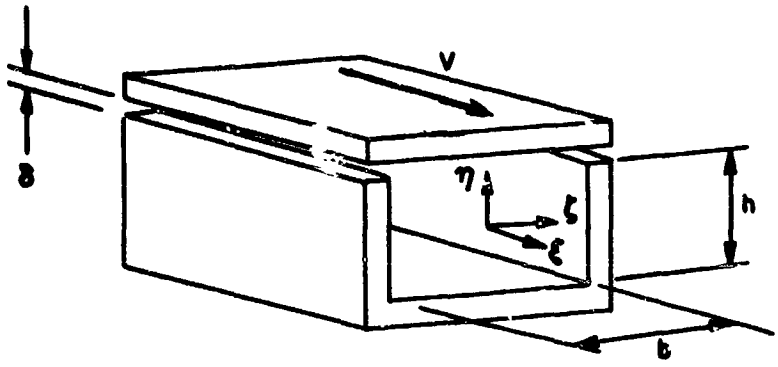

A

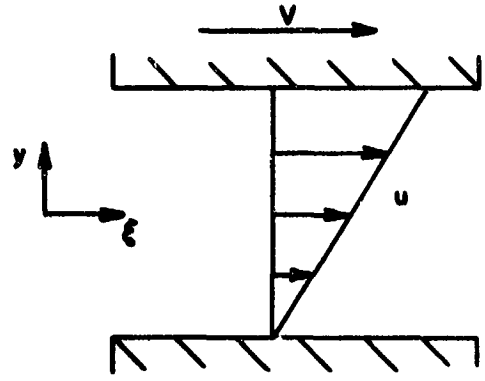

B

Couette Flow Approximation to Flow in Screw Channel

Figure A-2

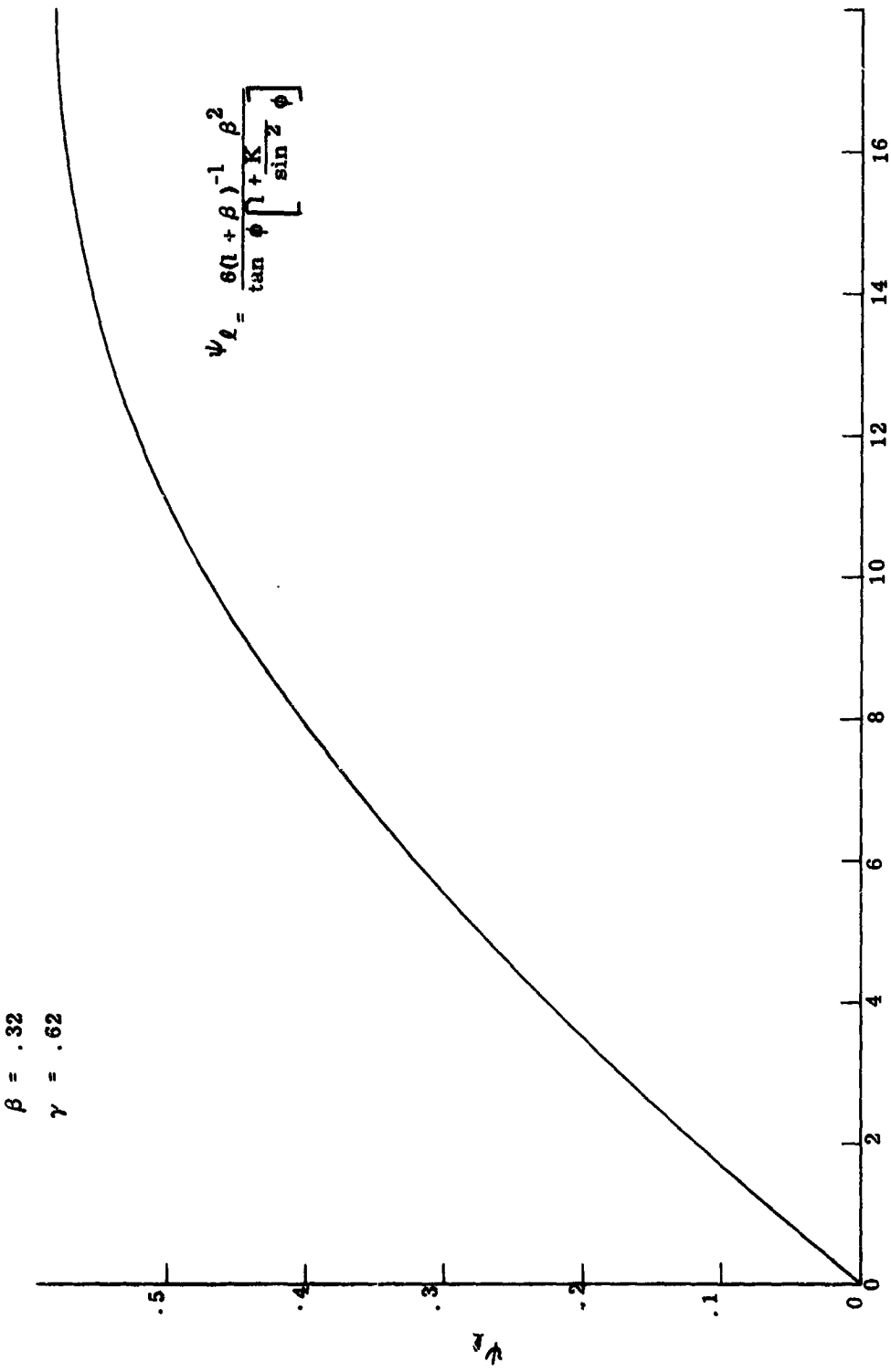

Variation of Sealing Coefficient With Helix Angle, Laminar Flow

Figure A-3

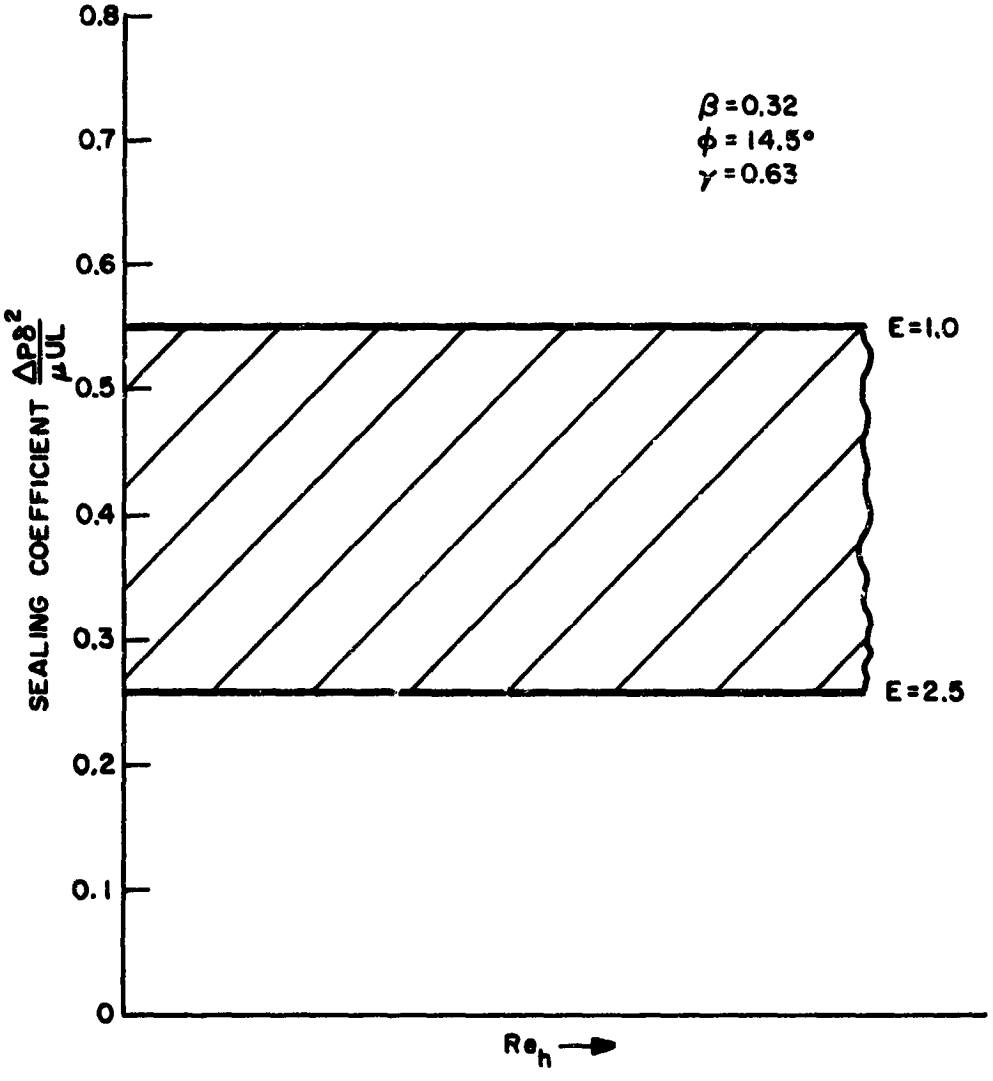

Variation of Sealing Coefficient With Eccentricity

Figure A-4

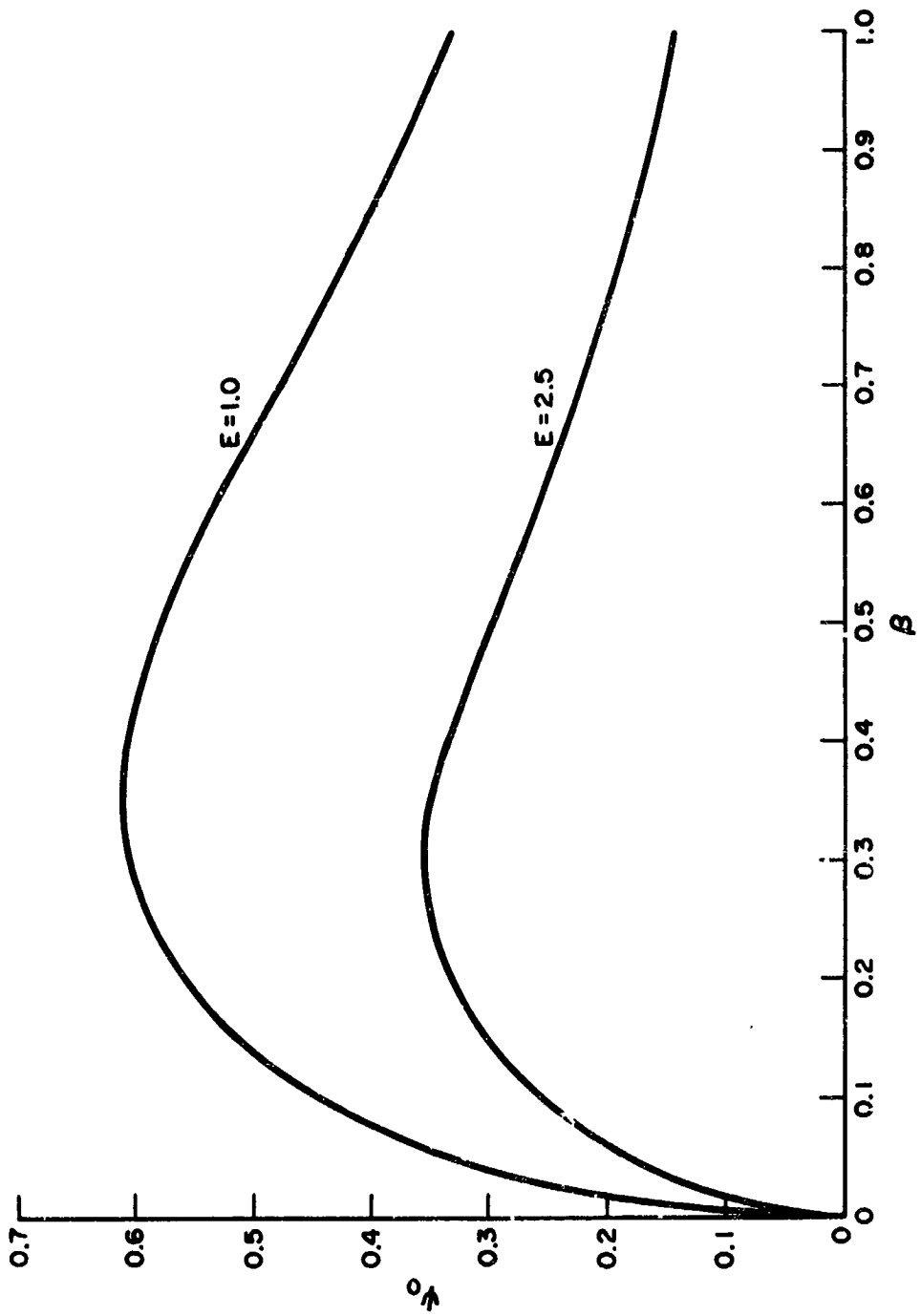

Maximum Sealing Coefficient at Any Given β

Figure A-5

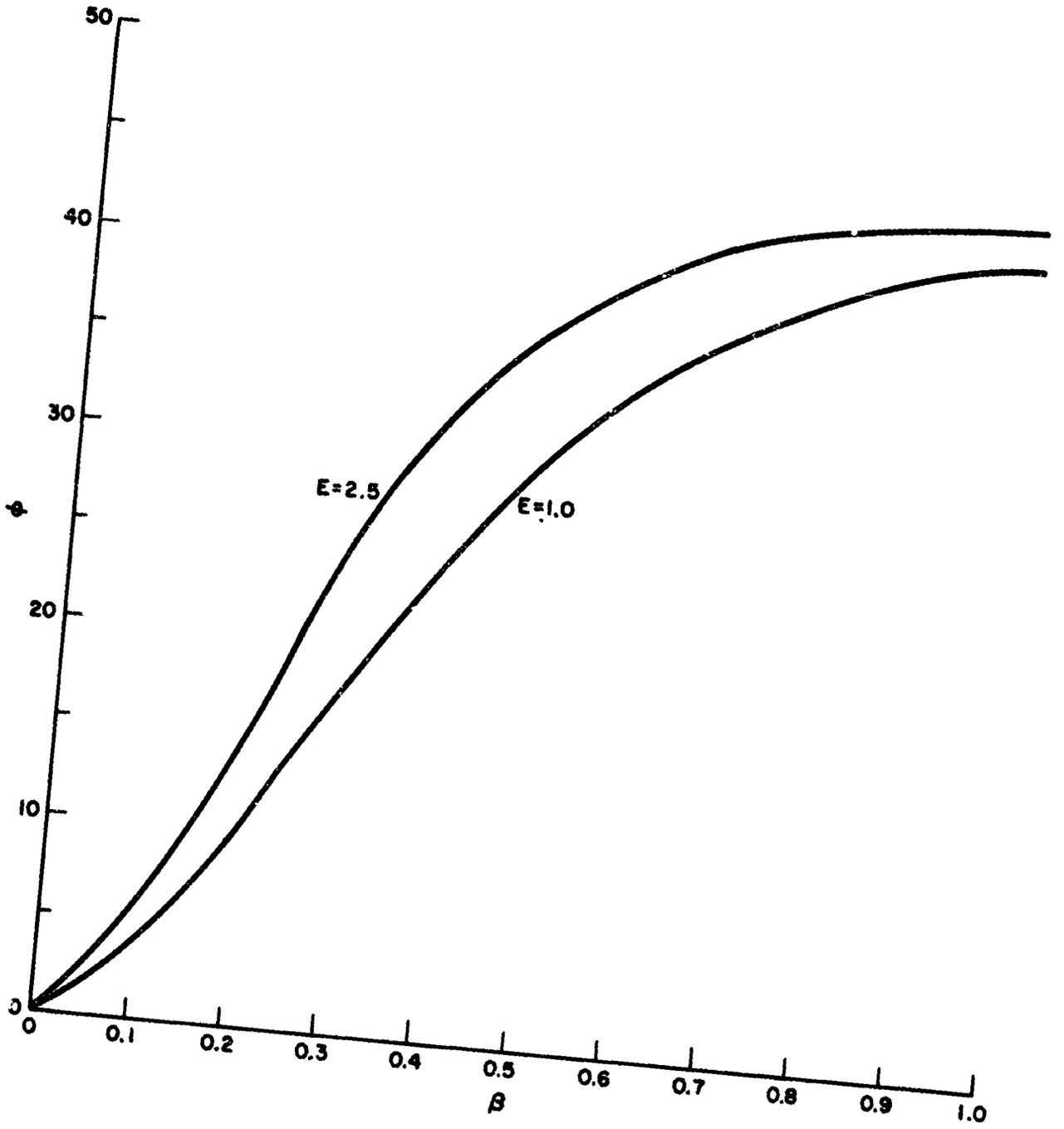

Helix Angle Required to Attain Maximum Sealing Coefficient

Figure A-6

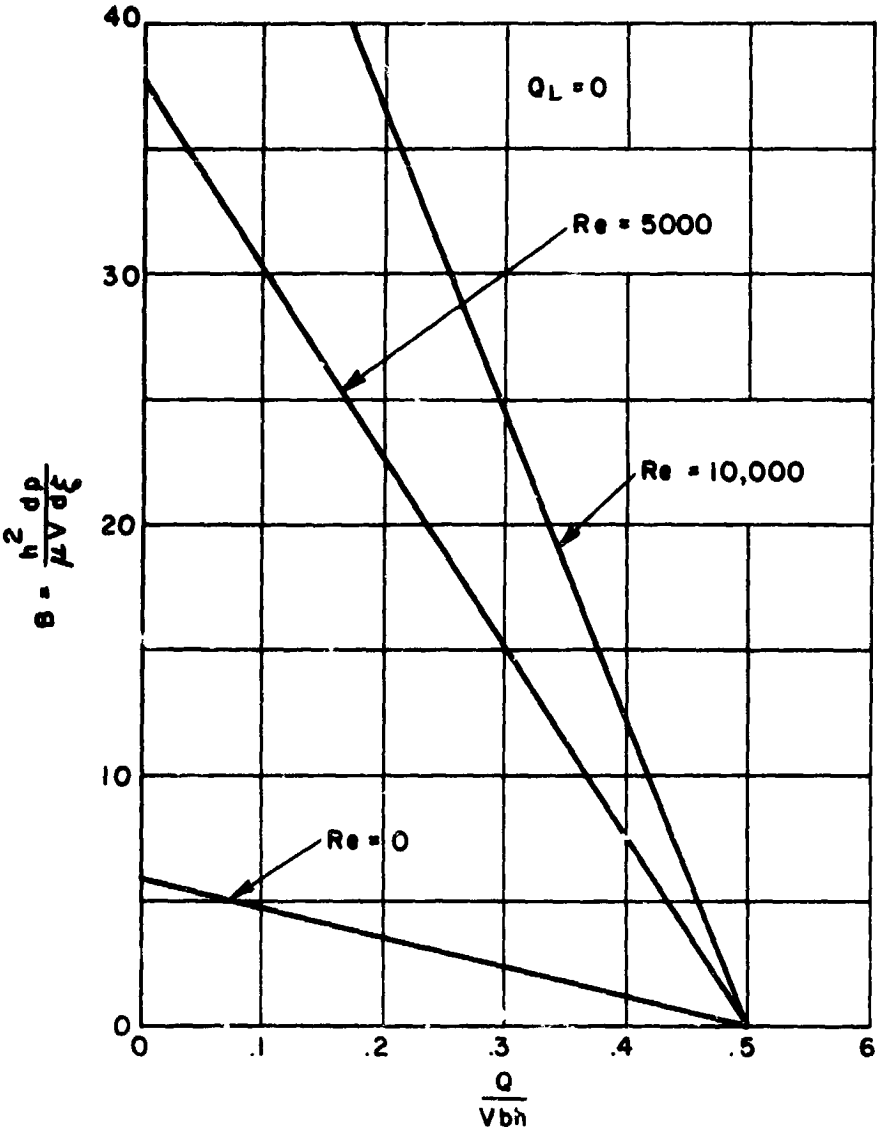

Theoretical Screw Pump Characteristic

Figure A-7

Report No. 2808, Vol. I

SNAP-8 SEALS-TO-SPACE DEVELOPMENT TEST PROGRAM

Aerojet-General Corporation

ABSTRACT

The role of the visco pump in a seal-to-space concept is discussed. Specific tests were required to demonstrate the proper functioning of the visco pump for operating conditions of the SNAP-8 power conversion system rotating assemblies. Results revealed the visco pump to be a reliable seal for SNAP-8 conditions. Basic data regarding interface stability, seal "breakdown," and pumping and drag coefficients were obtained.